Ph.D. Thesis

Université de Limoges


## University of Limoges

## ED 610 - Sciences et Ingénierie des Systèmes, Mathématiques, Informatique (SISMI)

**Faculté de science et Technique - XLIM équipe BioEM**


Thesis for the requirements of the degree of

Doctor of Philosophy

Sciences et ingénierie pour l'information : Electronique des Hautes Fréquences, Photonique et systèmes

Presented and defensed by


**Amani NEFZI**


On 02/02/2021

# Analysis and dosimetry of the coupling of electromagnetic waves with biological tissues: application to applicator design for biomedical and study of health effects

Thesis supervised by Delia ARNAUD-CORMOS and Philippe LEVEQUE

JURY :

Reporters

| | |
|---|---|
| **Mme. Elodie RICHALOT** | Professeur ESYCOM - Université Gustave Eiffel |
| **M. Jean-Lou DUBARD** | Professeur LEAT - Université Côte d'Azur |

Examiners

| | |
|---|---|
| **Mme. Valérie MADRANGEAS** | Professeur XLIM - Université de Limoges |
| **Mme. Noëlle LEWIS** | Professeur IMS - Université de Bordeaux |
| **Mme. Delia ARNAUD-CORMOS** | Maître de Conférences, IUF, XLIM - Université de Limoges |
| **M. Philippe LEVEQUE** | Directeur de recherche CNRS, XLIM - Université de Limoges |

*“He who has led you so far will guide you further.”*

**Rumi**

# Acknowledgements

Le travail de cette thèse a été effectué au sein de l'équipe BioEM à l'institut de recherche xlim. Je voudrais remercier toutes les personnes qui m'ont aidé et soutenu durant la thèse. Tout d'abord j'adresse mes sincères remerciements à mes directeurs de thèse Délia ARNAUD-CORMOS et Philippe LEVEQUE pour leur encouragement et leurs judicieux conseils durant la thèse. Je suis également reconnaissante pour leur aimable humeur et leur gentillesse. Les réunions et les longues discussions avec eux ont été très enrichissantes et accompagnées de moments de rigolade. Cette énergie et cette ambiance m'ont boosté pour avancer et bien réussir ma thèse. J'ai vraiment pris un grand plaisir à travailler avec eux.

Je tiens aussi à remercier Elodie RICHALOT professeur à l'université Gustave Eiffel et Jean-Lou DUBARD professeur à l'université de Côte d'Azur pour avoir accepté d'être rapporteurs de cette thèse. Je remercie également Valérie MADRANGEAS professeur à l'université de Limoges et Noëlle LEWIS professeur à l'université de Bordeaux d'avoir accepté d'examiner ce mémoire.

J'adresse de chaleureux remerciements à tous mes collègues de l'équipe BioEM notamment Martinus Dobbelaar et Lynn CARR pour leur agréable compagnie et leur aide. Un grand merci à Rosa ORLACCHIO pour son assistance et sa patience pendant les longues et complexes expérimentations qu'on a effectuées ensemble. J'associe à ces remerciements Nour TABCHEH pour sa convivialité et sa bienveillance.

Je désire en outre remercier tous mes amis et spécialement Inés, Mariem, Dali et Sirine avec qui j'ai pris mes pauses au labo, j'ai voyagé et j'ai partagé d'agréables moments d'amitié, de joies et de complicité. Je vous remercie pour tous les souvenirs qu'on a construits ensemble et j'espère que nous atteindrons tous nos objectifs et trouverons ou créons un emploi satisfaisant.

Enfin, j'exprime ma profonde et sincère gratitude à ma famille pour leur amour, leur aide et leur soutien continus. Je suis reconnaissant à mes frères d'avoir toujours été là pour moi en tant qu'amis. Un ENORME MERCI à mes parents pour leur encouragement, leur attention et leur confiance tout au long de mes années d'études. Je leur suis redevable de m'avoir offert les opportunités et les expériences qui ont fait de moi ce que je suis. Ce parcours n'aurait pas été possible sans eux et je leur dédie cette étape importante.

# Contents

# List of Figures

**List of Tables**

# General introduction

Wireless communication technology evolved rapidly in the past decades with the advent of digital standards. Therefore, numerous wireless communication systems, services and applications were developed. Due to the scientific and technological constant progress, the use of these devices is in continuous growth and the demand is increasing constantly. Human daily tasks whether personal or professional are essentially dependent on the wireless technology that permeated most of the fields with smartphones, computers, monitoring systems, broadcasting systems, therapeutic and diagnostic tools. Consequently, exposure to Radiofrequency (RF) electromagnetic fields (EMFs) increased because of the intensive use of these wireless devices and concerns raised regarding their potential health risks.

The RF band extends from 30 kHz to 300 GHz and is used for various applications such as maritime communications, broadcasting, terrestrial transmission and mobile communications which is the most used nowadays. Mobile communication technology underwent huge enhancement in the last two decades. Digital Mobile communication started with the Global System for Mobile Communications (GSM) standard set in 900 MHz and the 1800 MHz bands. Numerous studies called bioelectromagnetic then proceeded with the investigation about the health effects associated with RF exposures. They were mostly interested in investigating the effects induced by the GSM-900 and GSM-1800 mobile signals. Nowadays, the mobile communication bands expanded and includes other frequencies for the newer generations 3G-5G. Mobile phones are used mostly in the proximity of the head which may lead the brain to higher exposure levels compared to the body. Thus, it is essential to study the impact of mobile signals on the central nervous system, particularly the brain and its neuronal network.

Within this context, four types of studies are typically carried out which are epidemiological (on populations), clinical (on humans), *in vivo* (on animals) and *in vitro* (on cells). More particularly, *in vivo* and *in vitro* studies represent laboratory experimental assessments. *In vivo* experiments are conducted on or in living entities such as animals. *In vitro* refer to the experiments conducted on tissues or cells outside their natural environment within a culture holder or a tube.

To perform laboratory biological *in vitro* experiments, an experimental setup with equipment allowing the exposure of tissues, the observation and the recording of the biological changes are required. The exposure devices allowing the application of the EMFs to the samples and the recording devices used to detect the biological changes need to be characterized before conducting any biological experiment. The studies performed during this thesis are associated with the *in vitro* study type. However, no cells or tissues were used because this work aims to characterize at the microscopic scale a recording microsystem at 1.8 GHz. One type of system evaluated is an electrophysiological device designed to record the spontaneous electrical activity of neuronal networks during exposure to mobile phone signals. This system is developed by a team from IMS laboratory in Bordeaux with whom we collaborate.

The manuscript is divided into 4 chapters. The first chapter presents the general context of this study and is divided in two sections. The first section details the progress of wireless mobile communication and the services provided over the years. The interactions between the biological human organs and the mobile EMFs are overviewed. The occurrence of health risks due to the high exposures was prevented by defining norms. The basic restrictions set by the health organizations ensuring safe exposures are detailed. The health effects observed in previous studies are reported. The second section describes the bioelectromagnetic studies and the experimental setup required for *in vitro* experiments including the exposure systems and the detection methods and techniques. Examples of exposure devices suitable for laboratory experiments are described and categorized according to their field type and application.

The second chapter presents the materials and methods available to carry out dosimetry at different scales. It details, in particular, the different assessments conducted to characterize the selected microscopy technique suitable for our applications and objectives of microscale dosimetry. This chapter is divided in two sections. The first one describes the numerical software used to design and simulate the systems for their characterization. It also illustrates the numerical and experimental values of the energy absorbed by the biological target defined by the Specific Absorption Rate (SAR). Different types of SARs can be distinguished depending on the computing method. The second section overviews the features and the limitations of the methods that can be used for the macroscopic scale temperature measurements but not suitable for microscale recordings due to size limitations. Therefore, a few of the microscopy techniques based on temperature-dependent dyes that allow the detection of the biological changes such as temperature variation at the microscopic scale are presented and compared. One of these microscopic techniques based on a fluorescent dye named Rhodamine

B (Rhod-B) was selected due to its features to attain the objective of our study. A thorough characterization of the Rhod-B technique was conducted disclosing its sensitivity toward certain exposure parameters. The outcomes helped to optimize the technique for proper application on the microsystems under test. A theoretical approach is validated allowing the conversions and the exploitation of the fluorescence results to determine the rates of energy absorbed by the biological medium. An open transverse electromagnetic (TEM) cell is selected as the exposure device assigned for the evaluation of the microscopy technique and it was studied to determine its efficiency in terms of energy transfer and electric field (E-field) homogeneity.

The third chapter is divided in two sections and is assigned to the characterization of two electrophysiological recording devices at the macroscopic scale. They are based on microelectrode arrays (MEA). In the first section, both devices are described by showing their particularities regarding their structures and components. For the experimental dosimetry, the recording devices are combined with the open TEM cell exposure device for EMFs application. Real-time assessments consisted of temperature recording with a standard temperature probe. This study revealed MEAs sensitivity toward the proximity environment. The second section discusses the numerical macroscale investigations that consisted of reproducing the exposure and recording devices in the different conditions tested experimentally. The outcomes revealed the steadier version of MEA and the most adequate for biological experiments.

The fourth chapter combines the findings exhibited in the two previous chapters as it presents the characterization of the MEA recording devices at the microscopic scale based on the Rhod-B microscopy technique. This technique was applied to characterize another microsystem (i.e. microfluidic exposure system) as well which is designed for EMFs application to biological samples in fluidic conditions. Three sections constitute this chapter and the first one is dedicated to the evaluation of the MEA recording microsystems. It focuses particularly on the homogeneity of the energy absorbed by the biological sample during the exposure and the impact of the microelectrodes of these devices on the exposure uniformity and the energy absorption at the cellular layer. Experimentally, the MEAs are simultaneously investigated with the macroscopic method and the microscopic technique. Microscopic numerical simulations are performed only with the newer custom-designed MEA version. The E-field uniformity was investigated and different approaches were tested to solve the encountered simulation spatial resolution issues. The second section details the tests conducted to study the efficiency of the Rhod-B technique with a small amount of medium before the

characterization of the exposure microfluidic system. The third section discusses the results of the experimental assessments of the microchannel exposure device carried out in static conditions and they revealed the importance of the setup parameters for the success of the microscopic dosimetry of this device including the selection of the adequate values related to the exposure and the microscopy parameters. Numerical simulations illustrated the level of E-field homogeneity within the microfluidic device essential for biological experiments with cells.

This manuscript is completed by the conclusion and perspective section that synthesizes the main outcomes obtained and presents the envisaged perspectives followed by the list of the scientific publications and communications published during this thesis.

The work of this thesis stands within the framework of two projects supported by ANSES and by the Nouvelle Aquitaine region.

# Introduction générale

La technologie de communication sans fil a évolué rapidement au cours des dernières décennies avec l'avènement de la technologie de communication numériques. Par conséquent, de nombreux systèmes, services et applications de communication sans fil ont été développés. Due aux progrès scientifiques et technologiques constants, l'utilisation de ces appareils est en croissance continue et la demande augmente constamment. Les tâches humaines quotidiennes, qu'elles soient personnelles ou professionnelles, sont essentiellement basées sur la technologie sans fil qui imprègne la plupart des domaines avec les smartphones, les ordinateurs, les systèmes de surveillance, les systèmes de diffusion, les outils thérapeutiques et diagnostiques. Par conséquent, l'exposition aux champs électromagnétiques (CEM) radiofréquences (RF) a augmenté suite à l'utilisation intensive à ces appareils sans fil et des préoccupations existent concernant leurs risques potentiels pour la santé.

La bande des radiofréquences (RF) s'étend de 30 kHz à 300 GHz et elle est utilisée pour diverses applications telles que les communications maritimes, la radiodiffusion, la transmission terrestre et les communications mobiles qui sont les plus utilisées de nos jours. La technologie des communications mobiles a fait l'objet d'améliorations considérables au cours des deux dernières décennies. La communication mobile numérique a commencé avec la norme Global System for Mobile Communications (GSM) définie dans les bandes 900 MHz et 1800 MHz. De nombreuses études bioélectromagnétiques ont ensuite consisté à étudier les effets sur la santé liés à l'exposition aux RF. Initialement, ces études étaient surtout concentrées sur des effets induits par les signaux mobiles GSM-900 et GSM-1800. De nos jours, les bandes de communication mobile se sont diversifiées incluant d'autres fréquences pour les nouvelles générations 3G, 4G et 5G. Les téléphones portables sont principalement utilisés à proximité de la tête, le cerveau devenant alors une cible privilégiée par rapport au reste du corps. Ainsi, il est essentiel d'étudier l'impact des signaux mobiles sur le système nerveux, en particulier le cerveau et son réseau neuronal.

Dans ce contexte, quatre types d'études sont typiquement menés, à savoir les études épidémiologiques (sur les populations), cliniques (sur l'homme), *in vivo* (sur les animaux) et *in vitro* (sur les cellules). Plus particulièrement, les études *in vivo* et *in vitro* représentent des évaluations expérimentales en laboratoire. Des expériences *in vivo* sont menées avec des entités

vivantes telles que les animaux. *In vitro* fait référence aux expériences menées sur des tissus ou des cultures de cellules en dehors de leur environnement naturel.

Pour réaliser des expériences biologiques *in vitro* en laboratoire, un montage expérimental avec un équipement permettant l'exposition des tissus, l'observation et l'enregistrement des changements biologiques est nécessaire. Les dispositifs d'exposition qui appliquent les champs électromagnétiques aux échantillons et les dispositifs d'enregistrement qui détectent les changements biologiques doivent être caractérisés avant de mener toute expérience biologique. Bien que les travaux réalisés se placent dans un contexte d'étude *in vitro*, il n'a pas été utilisé de cellules ou des tissus. L'objectif est alors de caractériser, à l'échelle microscopique, un microsystème lors d'une exposition à 1,8 GHz. Le système évalué est un dispositif électrophysiologique conçu pour enregistrer l'activité électrique spontanée du réseau neuronal lors d'une exposition à des signaux de téléphonie mobile. Ce système est développé par une équipe de l'IMS à Bordeaux avec qui nous collaborons.

Le manuscrit est divisé en 4 chapitres. Le premier chapitre présente le contexte général de l'étude et est divisé en deux sections. La première détaille l'évolution des communications mobiles sans fil et les services fournis au cours des dernières décennies. Les interactions entre les organes biologiques humains et les CEM mobiles sont présentées. Les risques sanitaires liés aux expositions sont contrôlés et s'appuient sur la définition de normes. Les restrictions de base fixées par les organismes de santé garantissant des expositions sûres sont détaillées, ainsi que les effets sanitaires observés décrits dans la bibliographie. La deuxième section s'intéresse aux études bioélectromagnétiques et aux systèmes expérimentaux nécessaires aux expérimentations *in vitro*, comprenant les dispositifs d'exposition et les méthodes et techniques de mesure. Des exemples d'appareils d'exposition adaptés aux expériences en laboratoire sont décrits et classés en fonction de leurs types et de leurs applications.

Le deuxième chapitre présente les outils et méthodes disponibles pour réaliser la dosimétrie à différentes échelles. Il détaille, en particulier, les travaux et les évaluations menés pour caractériser une technique de microscopie retenue et adaptée à nos applications et objectifs de dosimétrie microscopique. Ce chapitre est divisé en deux sections. Le premier décrit le logiciel numérique utilisé pour concevoir, développer et caractériser les systèmes d'exposition. Il illustre également les différentes grandeurs numériques et expérimentales de l'énergie absorbée par la cible biologique définie par le débit d'absorption spécifique (DAS). Différents types de SAR peuvent être distingués selon l'approche retenue. La deuxième section présente

les caractéristiques et les limites des méthodes qui peuvent être utilisées pour les mesures de température à l'échelle macroscopique, mais qui ne conviennent pas aux enregistrements à l'échelle microscopique en raison des limitations de taille. Par conséquent, des techniques de microscopie basées sur des marqueurs biologiques dépendants de la température qui permettent la détection des changements physiques tels que la variation de température à l'échelle microscopique sont présentées et comparées. L'une de ces techniques microscopiques basées sur un marqueur fluorescent nommé Rhodamine B (Rhod-B) a répondu à nos attentes et objectifs. Une caractérisation approfondie de la technique Rhod-B a été réalisée, révélant sa sensibilité à certains paramètres d'exposition. Les résultats ont aidé à optimiser la méthode pour une application appropriée sur les microsystèmes testés. Une approche théorique a permis de valider le facteur de conversion et l'exploitation des résultats de fluorescence pour déterminer les taux d'énergie absorbés par le milieu biologique. Une cellule électromagnétique transversale ouverte (TEM) est sélectionnée comme dispositif d'exposition pour l'évaluation de la technique de microscopie et elle a été étudiée pour déterminer son efficacité en termes de transfert d'énergie et d'homogénéité du champ électrique (champ E).

Le troisième chapitre est divisé en deux sections et il est consacré à la caractérisation de deux appareils d'enregistrement électrophysiologique (MEA) à l'échelle macroscopique. Ils sont basés sur des réseaux de microélectrodes. Dans la première section, les deux dispositifs sont décrits en montrant leurs particularités associées à la structure et aux composants. Pour la dosimétrie expérimentale, les dispositifs d'enregistrement sont combinés avec le dispositif d'exposition pour l'application des CEM. Les évaluations en temps réel consistaient à mesurer la température avec une sonde classique non sensible aux CEM. Cette étude a révélé la sensibilité des microsystèmes à l'environnement de proximité. La deuxième section aborde les investigations numériques à l’échelle macroscopique qui consistaient à reproduire les appareils d'exposition et d'enregistrement dans les différentes conditions testées expérimentalement. Les résultats ont déterminé la version la plus stable et la plus adéquate pour les expériences biologiques.

Le quatrième chapitre exploite les résultats présentés dans les deux chapitres précédents. Il présente la caractérisation des appareils d'enregistrement MEA à l'échelle microscopique basée sur la technique de microscopie Rhod-B. Cette technique a également été appliquée pour caractériser un système d'exposition microfluidique développé pour exposer des échantillons biologiques aux signaux RF. Trois sections constituent ce chapitre et la première est consacrée à l'évaluation des microsystèmes d'enregistrement MEA. Elle s'intéresse particulièrement à

l'homogénéité de l'énergie absorbée par l'échantillon biologique lors de l'exposition et à l'impact des microélectrodes de ces dispositifs sur l'uniformité de l'absorption d'énergie au niveau des cellules exposées. Expérimentalement, les MEA sont étudiés aux échelles macroscopique et microscopique. Les simulations numériques à l'échelle microscopique sont effectuées uniquement avec la nouvelle version de MEA. L'uniformité du champ électrique a été étudiée et différentes approches ont été testées pour résoudre les problèmes de résolution spatiale rencontrés au cours des simulations. La deuxième section détaille les tests menés sur l'efficacité de la technique Rhod-B pour de petite quantité de milieu, permettant de caractériser un système microfluidique. La troisième section s'intéresse aux résultats des évaluations expérimentales du dispositif d'exposition à microcanaux réalisées dans des conditions statiques. Ils ont révélé l'importance des paramètres de configuration sur la réussite de la dosimétrie microscopique, en particulier le choix des valeurs adéquates pour l'exposition et pour les paramètres du microscope. Des simulations numériques ont illustré le niveau d'homogénéité du champ E dans le dispositif microfluidique essentiel pour les expériences biologiques avec des cellules.

Ce manuscrit est complété par une conclusion qui synthétise les principaux résultats obtenus et présente les perspectives envisagées, suivie par la liste des publications et communications scientifiques réalisés au cours de cette thèse.

Le travail de cette thèse s'inscrit dans le cadre de deux projets soutenus par ANSES et par la région Nouvelle Aquitaine.

# Chapter I.

## Context and state of art

# Introduction

Wireless communication technology rapid progress in the last few decades led to intense use of communication devices followed by an increase of the transmission and relaying equipment to respond to the growing demands. As electromagnetic fields (EMF) communication devices were more and more ubiquitous in our environment, it became essential to investigate their potential health effects. Experimental studies were massively conducted to detect through community health statistics, biological and medical experiments the health effects induced. Biological studies performed in laboratories consist in exposing a biological sample to short or long-term RF-EMFs and detecting the changes induced on the sample. These investigations are based on an experimental setup that includes multiple devices, tools and methods crucial for exposure assessment.

The first chapter of this thesis starts by presenting the background of the study by detailing the mobile communication technology and the associated health risks. Enhancements and changes conducted to provide new and rapid communication services are achieved by modifying the mobile phone signal characteristics (e.g. power intensity, frequency). Depending on these characteristics, the interaction between the human body and mobile communication EMFs can be different. Therefore, international organizations defined a set of norms based on the studies conducted to guarantee the general public safety. The effects observed from exposures respecting the norms are presented as well as those from exposures exceeding the safe limits. The biological effects observed depend on the type of EMF applied.

The second part of the chapter discusses typical bioelectromagnetic experimental setup implemented for laboratory studies. Numerous exposure devices were developed for biological studies. They are used to apply the RF-EMF to the biological sample under test. Selecting the suitable apparatus depends on several experimental parameters such as the biological application, the type of experiment and the size of the target. Hence, several exposure devices are described and their main features are evidenced.

# I.1. Mobile communications and potential health effects

## I.1.1. Evolution of mobile communications

Mobile telephony provides communication services allowing the transmission of sound, data, and images with other services. This sector has witnessed in the last century and up until now a huge evolution as it progressed through a sequence of generation bands [1], [2]. Mobile telephony communications (Figure 1) started around 1980 with the **first generation** (1G) which was an analog technology within 800 MHz to 900 MHz frequency band transmitting only voice signals. 1G was updated starting with around 1990 to a digital technology with the **second generation** (2G) [3]. Besides voice transmission, 2G provided data services like short message service (SMS) and Multimedia service (MMS). With 2G, the Global System for Mobile Communications (GSM) was introduced [3]. The 2G frequency bands were 900 MHz, 1800 MHz and 1900 MHz and the data transfer rate was around 10 kbit/s. New techniques were also implemented within 2G such as compression and encryption of data.

The **third generation** (3G) arrived in 2000 with improved features compared to the precedent generation [4] such as higher transmission data rate ranging from 144 kbit/s to 2 Mbit/s with cell phones offering advanced multimedia applications such as video conferencing and Internet browsing services. Frequencies used were between 1900 MHz and 2170 MHz. 3G technology corresponds to the start of smartphones era based on the universal Mobile Telecommunications system (UMTS) technology using terrestrial or satellite based waves propagation.

The **fourth generation** (4G) was developed with the aim to offer services with higher performances (speed, quality, capacity, etc.) [5]. With less power, the LTE (Long Term Evolution) standard that is considered part of the 4G, offers better connection quality compared to other technologies (e.g. GSM, UMTS) with a download speed of 100 Mbit/s and an upload speed of 50 Mbit/s. This technology offered greater frequency range depending on the user location. In cities, the band ranged from 2500 MHz to 2690 MHz and in rural areas from 790 MHz to 862 MHz. In 2015 and during the reorganization of the Digital terrestrial television in France, frequencies within the 700 MHz band were released for the 4G [6]. Thus, the 4G operates as well on the 703 – 733 MHz and 758 – 788 MHz. With LTE-Advanced technology

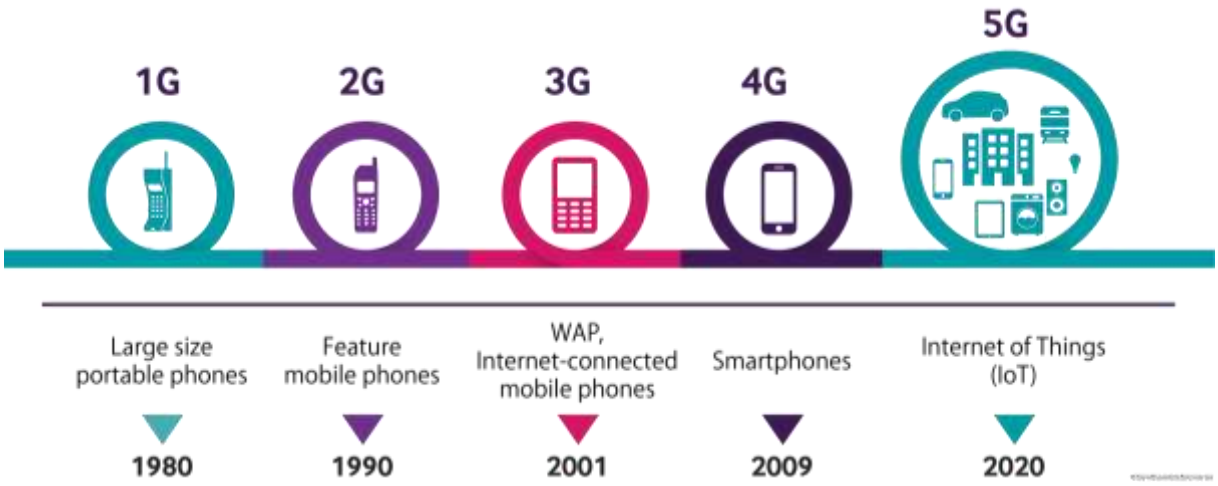


Figure 1 : Mobile communications evolution, from 1G to 5G [8].

known as 4G+, data rate improved to attain theoretically 1 Gbit/s for download and 500 Mbit/s for upload.

The **fifth generation** (5G) was launched in 2019 and it is today (end of 2020) available in many countries around the world [7]. Improvements were conducted with the 5G performances to fulfill the requirements of the massive Internet of Things (IoT). With a data rate up to 10 Gbit/s, a 1 ms latency, a large bandwidth, a 100 % coverage and virtually 100 % availability, the 5G can ensure the massive IoT. It allows the connection per unit area of up to 100 times more connected devices compared to the 4G and its bandwidth per unit area is 1000 times larger than that of the 4G. The 3.5 GHz frequency band was selected as the first band for 5G deployment. This band that ranges from 3.4 to 3.8 GHz provides good capacity, coverage and availability.

### I.1.2. Interaction of Radiofrequency fields with living material

Electromagnetic (EM) waves can penetrate the human body and their penetration depth is defined as the depth that the wave can travel inside the tissue until its intensity reaches a value of 1/e (0.36) of its initial value at the surface. The intensity of the EM wave inside a material diminishes exponentially from the surface as defined by equation ( 1 ). Moreover, the

penetration depth of an object depends on its electric and dielectric properties and on the EM wave frequency [9].

$$I(z) = I_0 e^{-\alpha z} \quad (1)$$

Where $I$ : the EM wave intensity in V/m as a function of the depth z

$I_0$ : the initial intensity at the surface in V/m

$\alpha$ : the attenuation coefficient in Np/m

The penetration depth of EMF into the tissues is high at low frequencies. It decreases when the frequency increases because above the body resonance frequency, tissues adopt a more predominant dielectric behavior. In addition, even if the body is exposed to the same level of E-field, EM waves will not be absorbed homogenously as the absorption depends on the composition of organs.

EM waves interact more with organs having higher water and salt contents because the ions contained in those organs contribute to the conductivity and by extension to the penetration depth. Figure 2 shows the penetration depth variation of some organs as a function of the frequency. Fat tissues and bones have the least water percentage compared to the rest of the body parts resulting in a low conductivity thus high skin depth. The bones conductivity is low and it was estimated from bovine bones in [10] to be about 0.3 S/m at 1.8 GHz. At this frequency, the bones penetration depth is about 8 cm (Figure 2) and it drops by more than 72 % to 2.2 cm at 3.5 GHz. Brain and lean tissues have lower penetration depth with 1.7 cm at 1.8 GHz and 0.85 cm at 3.5 GHz. The frequency increase caused a reduction of the penetration depth into the brain by ratio of 2. Muscles have the lowest skin depth values due to their great absorption to EMFs and they efficiently dissipate the energy into heat. These values show that the EM waves of the 5G mobile communication band (3.5 GHz) induce lower penetration compared to the 2G and 3G bands.

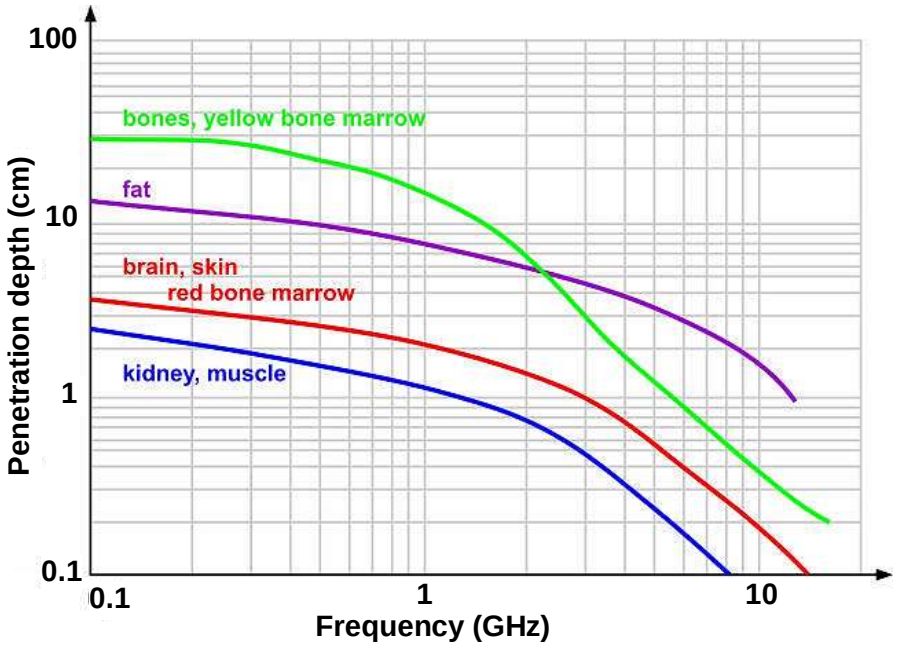


Figure 2 : Variation of the penetration depth of few organs as a function of frequency [11].

## I.1.3. Specific Absorption Rate (SAR)

To evaluate the rate of energy absorbed by the human body under the EMF exposure, a dosimetric quantity known as the specific absorption rate (SAR) expressed in units of watts per kilogram (W/kg) is generally used. SAR can be retrieved from the power loss density (PLD) which represents the energy dissipated in a volume and it is expressed in units of watts per cubic meter (W/m$^3$). Equation ( 2 ) describes the SAR as the time derivative of the energy dissipated $dW$ in a unit of mass $dm$ corresponding to a unit of volume $dV$ of a given density $\rho$.

$$SAR = \frac{d}{dt}\left(\frac{dW}{dm}\right) = \frac{d}{dt}\left(\frac{dW}{\rho \cdot dV}\right) \quad (2)$$

$$PLD = \frac{d}{dt}\left(\frac{dW}{dV}\right)$$

SAR can be quantified as the energy absorbed by E-field coupling defined by equation ( 3 ).

$$SAR = \frac{\sigma |E|^2}{\rho} \quad (3)$$

Where $\sigma$ the electric conductivity of the medium in S/m

$|E|$ the magnitude of the E-field in V/m

$\rho$ the volume density of the sample in kg/m$^3$

SAR can also be expressed as a function of the heat induced within the biological sample temperature and it can be computed from the initial increase in temperature as defined by equation ( 4 ).

$$SAR = C \left. \frac{\partial T}{\partial t} \right|_{t = t_0} \quad (4)$$

Where $\partial T / \partial t$ the initial slope of the temperature rise versus time curve

$t_0$ the start of the heat increase

$C$ the specific heat capacity of the medium (i.e. the amount of heat needed to increase the temperature of a substance by 1 °C) expressed in (J/(kg·K)).

$C_{water} = 4186$ J/(kg·K)

Different types of SAR can be computed numerically. Typical SAR include the whole body SAR where values are averaged over the whole body and the localized SAR obtained by averaging the values over a small volume, such as 1 g or 10 g. SAR 1 g (Figure 3) is obtained by averaging the maximum SAR of the points within the 1 g volume and this calculation is performed until it covers the whole sample volume. The same principle is applied for computing the SAR 10 g over 10 g volume covering the whole volume. For the point SAR no averaging is conducted and it represents the local value of SAR at every point within the sample providing higher special resolution than the two previous types.

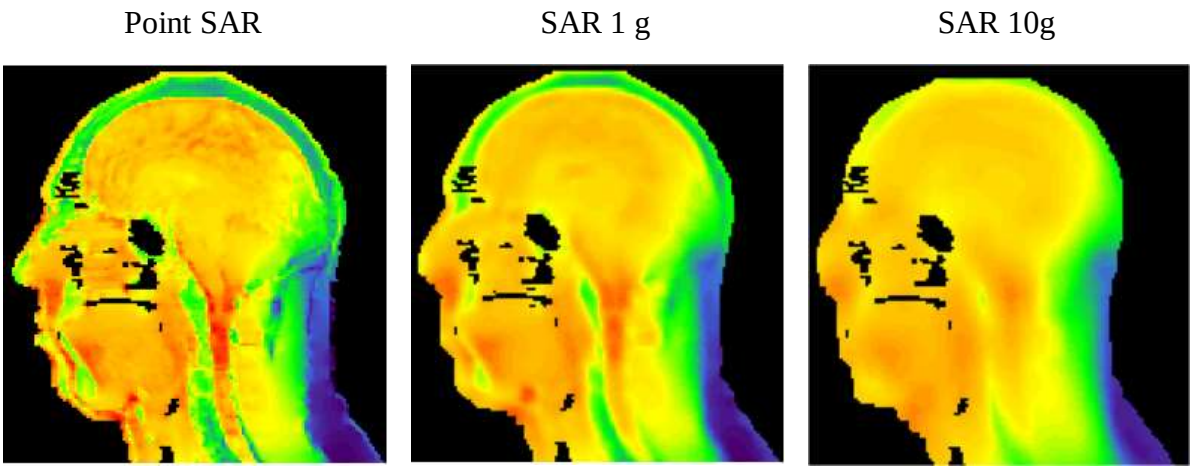


Figure 3 : SAR spatial distribution of human head, a) point SAR, b) SAR averaged over 1 g, c) SAR averaged over 10 g [12].

### I.1.4. Norms of mobile communication

With this huge evolution of mobile communication technologies, RF signal relaying equipment (i.e. base stations, antennas, etc.) were installed to cover the massive demand and usage of wireless modern devices. In addition to mobile phones, modern connected smart devices are ubiquitous in homes and offices increasing worries about health risks toward the exposure to RF EMFs.

However, mobile phones are not in continuous communication with the base station antennas. They transmit the signal only when they need to send data (i.e. calls, text messages, etc.) or to connect to a new base station when the user moving, gets out of the base station coverage area known as a cell [13]. When the device is in standby mode which means no calls or data are sent or received, it still receives RF signals continuously from the base for control purposes. Thus, the phone sends back low level signals to report its position and confirm its presence inside the cell of the serving base station every few minutes. The base station on the other hand, is communicating continuously with the devices and equipment in its cell which makes it a continuous whole-body exposure source. SAR values (i.e. whole-body and local SAR) depend strongly on the distance separating the RF source from the body exposed.

National and international organizations set the limits of EMF exposure to protect the population health using recommendations of the World Health Organization (WHO). The most

known international organizations that developed a large part of the norms currently applied are:

- The International Commission on Non-Ionizing Radiation Protection (ICNIRP)
- Institute of electrical and electronic engineers / International committee on electromagnetic safety (IEEE / ICES)
- International electrotechnical commission (IEC)
- European Committee for Electrotechnical Standardization (CENELEC)

Safety guidelines differ from one country to the other following the national recommendations. The safety limits are fixed by identifying the minimum exposure level needed to produce harm according to the scientific data. Also, reduction factors were applied that are larger for the general public than for workers. The basic restrictions consisting of SAR values are then determined with a large margin of safety. Hence, based on the basic restrictions reported by ICNIRP in the 2020 guideline [14], the safety distance limits from emitting antennas were defined to be 75 cm in [15] and 1 m in [16] for the general public.

Experimental studies showed that an EMF exposure to an average whole-body SAR of 6 W/kg at the frequency range 100 kHz – 6 GHz during 1 hour induces 1°C elevation of temperature. Therefore, ICNIRP considered, in the 2020 guideline [14], that the minimum exposure level that could induce a temperature rise of 1 °C is a whole-body SAR of 4 W/kg applied for 30 minutes at the frequency range mentioned. And as presented in Table 1, ICNIRP fixed the basic restrictions by reducing even further the value by 10 and 50 respectively for a controlled environment for workers and an uncontrolled one for the general public. With a large safety margin, limits were set respectively at 0.4 W/kg and 0.08 W/kg for the whole-body exposure.

Safety limits were also set for the head, torso and limbs within 100 kHz – 6 GHz frequency range. A localized SAR 10g of 20 W/kg is considered to cause 2°C of heat in the head and torso, and 40 W/kg heats the limbs and raises its temperature by 5°C after 6 minutes of exposure. For safety measures, ICNIRP reduced these values by 2 and 10 factors respectively for the occupational and the general public.

For frequencies above 6 GHz, EMFs absorption is more superficial resulting in a temperature rise within the skin which makes the dissipation process easier. Nevertheless, the basic restriction was determined to be 20 W/m$^2$ for the general public within 4 cm$^2$ surface area after a reduction by 10. This corresponds to the safety threshold set for both head, torso and limbs.

| **Whole body** ⬇ | | **Head and torso** ⬇ | | **Limbs** ⬇ | | **Head and torso, Limbs** ⬇ | | | |
|---|---|---|---|---|---|---|---|---|---|
| **Frequency range** 100 kHz – 300 GHz | | **Frequency range** 100 kHz – 6 GHz | | | | **Frequency range** 6 – 300 GHz | | | |
| **ΔT after 30 min** | | **ΔT after 6 min** | | | | **ΔT after 6 min** | | | |
| 1 °C | | 2°C | | 5°C | | 5°C | | | |
| **whole body SAR** averaged over 30 min | | **SAR 10g** Averaged over 6 min | | | | **SAR 4cm²** Averaged over 6 min | | **SAR 1cm²** | |
| 4 W/kg | | 20 W/kg | | 40 W/kg | | 200 W/m² | | 400 W/m² | |
| ↘ ↙ | | ↘ ↙ | | ↘ ↙ | | ↘ ↙ | | ↘ ↙ | |
| workers | General public | workers | General public | workers | General public | workers | General public | workers | General public |
| **Safety reduction factors** | | | | | | | | | |
| 10 | 50 | 2 | 10 | 2 | 10 | 2 | 10 | 2 | 10 |
| **Threshold whole body SAR** averaged over 30 min | | **Threshold SAR 10g** averaged over 6 min | | | | **Threshold SAR 10g** averaged over 6 min | | | |
| 0.4 W/kg | 0.08 W/kg | 10 W/kg | 2 W/kg | 20 W/kg | 4 W/kg | 100 W/m² | 20 W/m² | 200 W/m² | 40 W/m² |

Table 1 : Basic restrictions set by the ICNIRP for the whole body, head, torso and limbs for RF-EMF induced health effects.

## I.1.5. Effects of EMFs

The basic restrictions are set with additional safety measures for daily exposures and it was shown that high SAR values induce body temperature increase. Studies focused initially on the impact of these thermal effects on the biological cells. To ensure the general public safety, research investigations were focused on potential health risks occurring with exposures under levels respecting the limits. Thus, RF-EMFs effects were divided into two categories: the thermal effects due to temperature rise and the non-thermal effects consisting of potential health induced from low-level exposures.

### I.1.5.1. Thermal effects

Thermal effects could cause harm to the human body if the exposure exceeded the safe threshold, hence, several groups investigated the whole body temperature variations induces by RF exposure and the associated potential health impairment. An increase in body temperature by more than 1°C can cause various health effects, although, usually the heat is dissipated by thermoregulation to maintain the normal functions of cells. Furthermore, serious health accidents can occur in the case of hyperthermia when the temperature exceeds 40°C. Ramsey et al. reported in [17] through 14 month period experiments, during which workers' behavior was observed, that hyperthermia affects significantly the workers' healthy behavior. Various adverse health effects were detected due to hyperthermia [18]; most importantly it causes thermoregulation physiology impairment that leads to irreversible cell damage and heat strokes.

*In vitro* studies showed that the exposure to high energy EMF induces temperature rise of biological samples as well which may lead to numerous biological changes. Takashima et al. performed high SAR exposure on two cell lines and reported that applying continuous or intermittent RF signal at 2.45 GHz with a SAR of 50 W/kg causes a temperature rise > 2°C within 30 minutes [19]. Experiments with both cell lines to continuous or discontinuous RF signals with SAR up to 100 W/kg showed no significant biological changes compared to the sham-exposed cells. However, a SAR of 200 W/kg induced a decrease in cell survival and inhibited cell growth. Therefore, continuous and pulsed RF fields induce similar biology effects on cells when they are applied with the same energy levels. These experiments were based on SAR levels that exceed the ICNIRP basic restrictions of 2 W/kg causing considerable

temperature elevation. Furthermore, above a certain exposure level, temperature high increase caused serious adverse changes on cells.

#### I.1.5.2. Non-thermal EMF effects

Low-level exposure to mobile EMFs with levels below the basic restrictions fixed by the ICNIRP does not normally induce thermal risks because the body can regulate its temperature under these low exposure levels. Nevertheless, this topic is under constant focus and numerous studies investigate till this day potential non-thermal effects that can occur due to the long term exposure. Mobile phones are intensively used nowadays and they are mostly in the proximity of the head especially during calls. Thus, due to the very small distance, the human head is exposed to higher E-field levels than the rest of the body possibly influencing in turn the brain physiology [20], [21]. Hence, the focus was set on studying the impact of mobile signals on the central nervous system, especially the brain and its neuronal network. Electrically, neurons are excitable cells which makes them more susceptible to be affected by the RF fields. They are responsible for carrying information inside the brain and throughout the whole body using electrical and chemical signals.

This topic was studied extensively for the last few decades and several brain functions were evaluated under the influence of mobile (GSM) signals. The investigations are based on epidemiological, clinic and laboratory experimental studies. The epidemiological analysis consists of detecting and observing health effects related to a change of the brain electrical activity in a distinct group of people exposed to RF signals. Clinical studies are based on the electrophysiological assessments by measuring brain activity through the electroencephalogram (EEG) that is a non-invasive method allowing the measurement of the electric voltage changes (Figure 4). Regarding the laboratory experimental research, they are based on animal *in vivo* and cells *in vitro* studies.

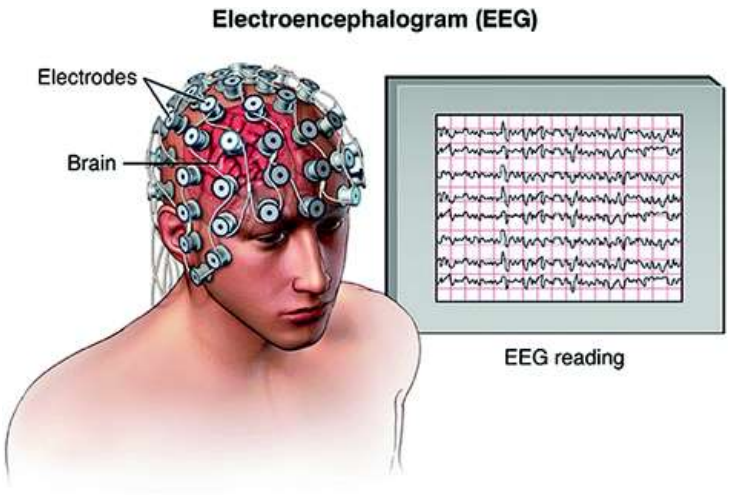


Figure 4 : Electroencephalogram (EEG) brain activity recording [22].

In France, French Agency for Food, Environmental and Occupational Health and Safety (ANSES) analyzes research related to the RF fields impact on health. The main conclusions of the ANSES, RF-EMF and health assessments of 2009 and 2013 reports [23], [24] are synthetized in the following paragraphs.

The majority of tests conducted on animals to evaluate their cognitive, memory and behavior functions under RF exposure show major methodological limitations. Reliable publications reported that RF signals did not induce any degenerative effects on mice [25], [26]. Some even concluded that the exposure seems able to improve cognitive and memory performances of mice in certain tests [27]–[30].

Amid the clinical research publications on humans, few studies recorded insignificant negative effects on the response time [31]–[33] and reported that these effects observed from the EEG of cognitive functions depend on the person's age, the exposure duration and side against the head. Numerous studies inferred the absence of mobile signals (GSM, UMTS, WCDMA) exposure effects on cognitive functions (reaction time and answers accuracy) [34]–[37]. Cursio et al. have noticed a shortening of the reaction time under GSM exposure [38].

One *in vivo* experimental study on animals assessed the sleep quality of rats under RF exposure [39]. An increase was noticed in the repetition rate of one of the sleep stages (i.e. paradoxal sleep). ANSES stated in the report of 2013 [24] that further investigations are needed to obtain an accurate opinion on this topic.

Seven articles investigated the effects of mobile signals exposure on sleep quality of humans. Four epidemiological studies concluded the absence of any effect disturbing the sleep quality for short or medium-term (i.e. 1 year) exposures [40]–[43]. Also, the three polysomnographic studies performed in laboratory agreed that for young men, acute exposure to a mobile signal (GSM-900) probably does not affect the electrical macrostructure of sleep [44]–[46]. Schmid et al. [45] and Loughran et al. [46] reported as well an increase in the EEG power within the sleep spindle (i.e. bursts of neural oscillatory activity) frequency range (i.e. 12 – 14 Hz). Danker-Hopfe et al. [44] detected a change in the duration of sleep stages, thus, RF exposure may alter the brain physiology without perturbing the sleep quality or the cognitive tasks associated. However, these studies lack data for other ages (i.e. children and elderly), gender (i.e. female) as well as other types of RF signals.

The association between mobile phone use and tumor growth in the brain and central nervous system has been the subject of numerous studies yet this remains arguable. Research focused on assessing the risk levels associated with RF exposure for carcinogenic effects. The animal *in vivo* studies identified by ANSES in [24] did not evidence that exposure to non-thermal exposure levels causes the initiation or the promotion of cancer [47], [48].

For humans, publications studied tumoral effects in brain related to RF exposures and focused on both benign and malignant tumors. Little et al. selected data between 1992 and 1996 of people diagnosed with glioma (most common malignant brain tumor) at age 18 and older [49]. Based on the mobile phone subscriptions data from 1982 onward, they estimated the risks of glioma development from 1997 till 2008 with the consideration of latency periods, phone use hours, age, etc. The projected rates obtained were compared with incident cases reported in the Interphone study of 2010 [50] and the Swedish study of Hardell et al. 2011 [51] and Little et al. concluded that for observation periods of 10 years, the rates were substantially higher than that found in the two epidemiological studies. Thus, the ANSES synthesis regarding these studies led to conclude that the possibility of an association between mobile phone signals and the development of glioma was reduced. No compelling data have evidenced the risk increase of developing any type of cancer (glioma, meningioma, acoustic neuroma, leukemia, etc.) related to the regular mobile use [52]–[56].

Within the National Toxicology Program (NTP) supported by US government agencies within the department of health and human services, *in vivo* carcinogenesis and genetic toxicology studies were conducted on rats [57]. A group of male and female rats received

whole-body exposure to RF modulated mobile signals (i.e. GSM or CDMA) at 900 MHz for 28 days or 2 years inside reverberation chambers. A reverberation chamber or room is a closed large metallic cavity that includes reflective surfaces causing the reflection and the stirring of the EM waves generated inside the chamber by antennas. The reverberation effect creates an homogenous and isotropic i.e. same physical properties at all EMF directions. The rat groups of the 28 days study were exposed to 0 (sham control), 3, 6 or 9 W/kg for 5 to 7 days per week. Those of the 2 years study were exposed to 0 (sham control), 1.5, 3, or 6 W/kg for 7 days per week. Exposures lasted 18 hours and 20 minutes per day. The genetic toxicology investigation results showed no significant increase in micronucleated red blood cells in peripheral blood for either male and female rats and for both RF signals. No significant increase of DNA damage was reported in males and females rats for frontal cortex, hippocampus, cerebellum, liver, and leukocytes after RF GSM signal. However, DNA damage tests following the CDMA signal exposure did not provide consistent outcomes between male and female rats neither for the different types of the biological cells. For the carcinogenesis study, it was reported that no clear evidence found proving carcinogenic activity for female rats with both RF signals. As for male rats, it was reported that exposure to GSM or CDMA modulated signals resulted in an equivocal proof of carcinogenic activity.

Depending on the power level of EMFs applied different effects were observed and reported from the *in vivo* and the *in vitro* studies conducted. Exposure to continuous EMFs induces either an increase of the local or the whole body temperature when applying high power values. Low-level exposure was shown to not affect human health but in some cases, it induces biological changes without impairment of the biological target physiology and it was reported that it can improve certain brain functions.

Equivalently, numerous studies focused on the biological effects of discontinuous EMFs known as the pulsed E-fields and revealing their impact on the biological cells that are strongly dependent on the pulses duration and intensity as illustrated in the next section.

### I.1.6. Pulsed electric field (PEF) effects

The application of a short intense Pulsed E-Field (PEF) with low repetition rate and without high frequency carrier was reported to increase the cell permeability known as electroporation [58]. During the exposure positive and negative charges start to accumulate on

both internal and external sides of the membrane increasing, in turn, the transmembrane voltage to a level where membrane conductivity rises leading to the creation of pores. Two types of electroporation can be observed depending on the pulses duration regarding the cell membrane charging time.

Charging time of the cell plasma membrane, typically higher than 50 ns, depends on the physical and biological properties of the cell such as the dielectric properties of the membrane, the cell suspension, the cytoplasm, the organelle as well as the size of the cell itself [59].

#### I.1.6.1. Conventional electroporation

Conventional Electroporation is a method to access the cell cytoplasm and its microorganisms and is generally induced by cells exposure to large and intense E-field pulses with durations higher than the plasma membrane charging time. Pulses lasting from few microseconds (µsPEF) to hundreds of milliseconds (msPEF) with intensity up to 10 kV/cm were reported to cause electroporation of the plasma membrane of cells [60]–[62]. Pulses parameters (i.e. shape, intensity, duration and number of pulses) settings are selected according to application needs [63], [64] and whether planning on applying the conventional electroporation with reversible or irreversible effects.

#### I.1.6.2. Nanoporation

Super short pulses with nanosecond (nsPEF) and sub-nanosecond durations and higher intensities ( > 10 kV/cm) were shown to induce smaller size and higher number of pores within the plasma membrane of the cell. nsPEF is shown to penetrate the cell and cause the electroporation of the intracellular components as well without permanent damage to the plasma membrane [65]–[67].

Reversible electroporation is a transient effect meaning that after the permeabilization the membrane heals returning to its initial form. Reversible electroporation either achieved with nsPEF or msPEF can be exploited for numerous therapeutic applications. Due to the increase of membrane permeability, an exchange of material generally occurs through the membranes providing a pathway for molecule transport. This alteration is beneficial for drug delivery such as anticancer drugs to treat tumors [68], [69] known as electrochemotherapy. Useful as well for gene therapy (DNA transfer) [70]–[73], introduction of protein into the cytoplasm [74],

cryopreservation of biological tissues [75] and applications in other fields such as the treatment of waste water [76] and stimulation of plants metabolism [77], [78].

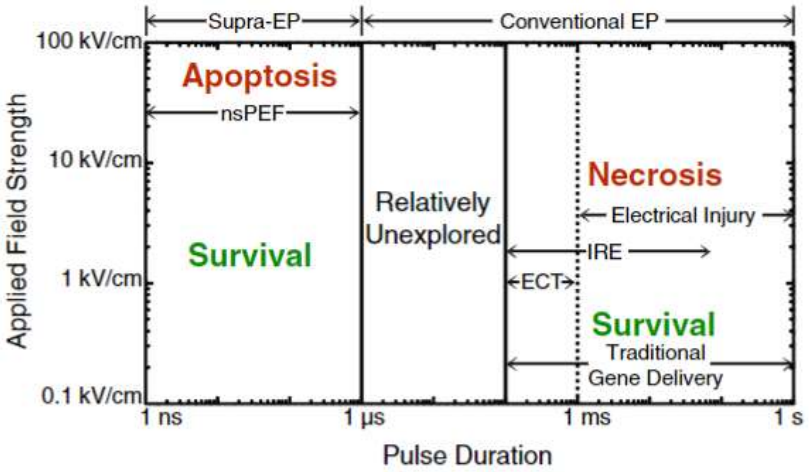


Figure 5 : PEF intensities and durations values inducing nanoelectroporation (supra-electroporation) or conventional electroporation with ranges causing cells death (irreversible electroporation) [79].

Pulses with higher energy, obtained either by increasing the intensity and the pulse duration simultaneously (Figure 5) or the repetition rate, can induce irreversible electroporation. It causes permanent damage to the cell membrane causing their death (i.e. necrosis /apoptosis) or allow inhibition of microorganisms activity (i.e. growth, division, etc.) useful for tumor growth cessation [80] or cancer cells ablation [81]. Irreversible electroporation is used in food processing and biorefinery [82] due to its advantages regarding other methods in preserving food quality and nutrients. It was used to dehydrate tissue, inactivate microbes to sterilize, pasteurize and preserve certain food products.

Pulsed E-fields effects are classified as non-thermal because samples are exposed to low energy doses although, increasing the repetition rate of pulses may result in the appearance of electric and thermal effects [83] as discussed previously. All the investigations and the studies on the biological entities interactions with the EMF and the potential effects are associated with the field of bioelectromagnetism.

## I.2. Bioelectromagnetic studies

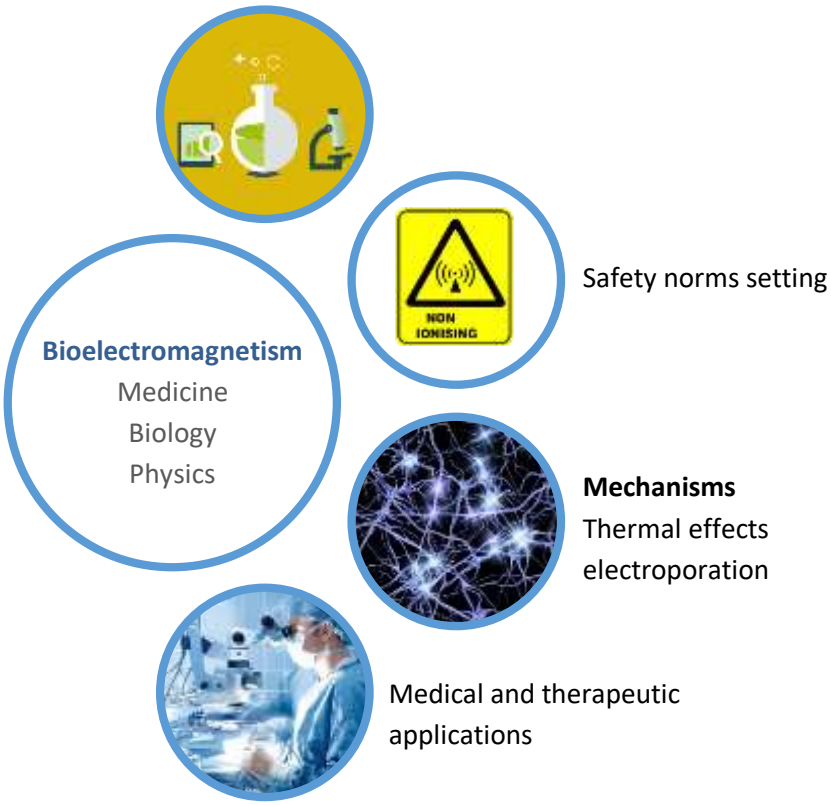


Figure 6 : Bioelectromagnetism studies assembles different fields and research topics.

Bioelectromagnetism is a multidisciplinary field that brings together researchers from different fields; medicine, biology, and physics to investigate E-field health effects, determine the mechanisms of interaction and develop based on electronic technology methods to improve the therapeutic and medical treatments (Figure 6). This thesis mainly focuses on physics setups and methods for *in vitro* experiments. The experimental setups (Figure 7) can generate RF signals, expose the biological samples, observe in real-time the biological changes, and achieve the dosimetry to quantify the energy doses absorbed.

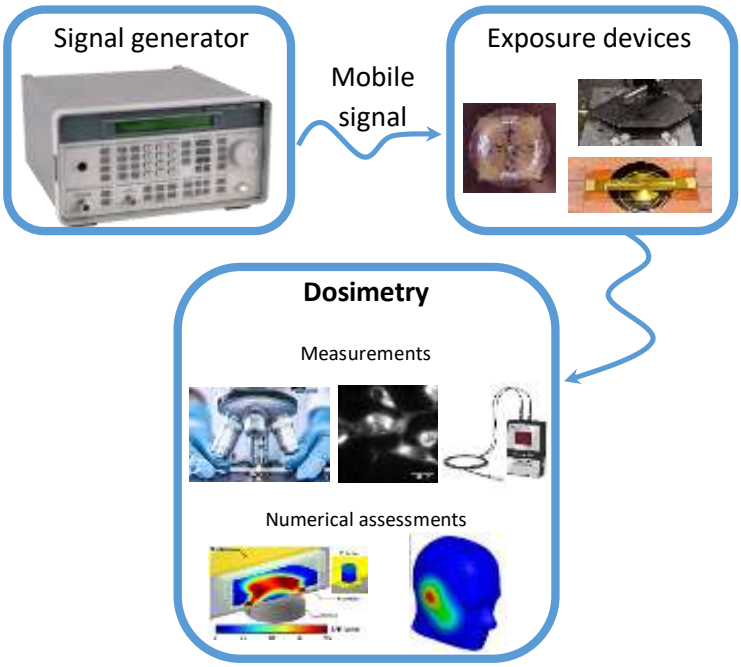


Figure 7 : *In vitro* exposure and dosimetry setup.

## I.2.1. Radiofrequency EMF exposure devices

Exposure devices used for the application of RF-EMF to the biological samples aiming to investigate the biological effects are countless. *In vitro* studies require the use of devices that meet certain biological and EM criteria and demands such as the biocompatibility, the operational frequency, the application of homogenous and uniform EF. Systems can be classified depending on the experiments type, *in vitro* or *in vivo*, or on the protocol that can be offline or real-time. Paffi et al. reviewed RF exposure devices developed from 1999 for bioelectromagnetic investigations and arranged them into three categories; propagating, resonant and radiating exposure devices [84], [85]. From each category, a few devices will be briefly described hereafter.

### I.2.1.1. Propagating exposure devices

Waveguides

Waveguides are suitable for bioelectromagnetic experiments and they have been used by several research groups for the exposure of biological samples to E-field [84]. E-field can

be uniform in the biological target if it has been placed at the proper position within the waveguide. Waveguides were developed in different shapes (rectangular, circular, radial, etc.) and they were integrated within experimental setups dedicated to *in vitro* and *in vivo* studies. In the case of close waveguide structures, the E-field propagating is confined inside the device and the energy applied to the biological target can be determined by monitoring the power transmitted at the input and that received at the output of the waveguide [86]. Numerous bioelectromagnetic studies were based on these close waveguides even though they are not suitable for real-time observation. For example, rectangular waveguides were used to investigate the effects of GSM signals on the permeability of cells [87] and other biological effects [88]. Besides, the temperature within a close waveguide cannot be controlled and the structure does not allow air flow. Thus, these waveguides should be placed within an incubator if their size allows it.

Close structures do not allow real-time measurements and biological evaluation is usually performed after the end of the experiment. Modifications can be applied to these structures for real-time biological effects detection. For example, waveguides can be perforated and coupled with a detection device [89] or probes can be inserted for temperature or E-field recording [90].

Coplanar waveguides are open structures. They were first introduced by Cheng P. Wen in 1969 [91]. Biological exposure within the waveguide channels can be performed in static or also in fluidic conditions when exposing cells in their culture medium. Cells inserted land on the bottom of the device without displacement in static condition whereas, in the fluidic ones, they circulate along the channels through perfusion tubes. This structure allows real-time detection and observation. Liberti et al. and Paffi et al. proposed a coplanar waveguide suitable for the EM and biological requests [92], [93]. Optimizations were achieved on the electrophysiological exposure device to minimize the radiation losses, avoid higher modes losses, and ensure the impedance matching (50 Ω) with the rest of the equipment. E-field was evaluated to be quite homogenous in the observation window between the electrodes.

Another propagating exposure device known for its numerous advantages is the Transverse Electromagnetic cell.

Transverse Electromagnetic (TEM) cell

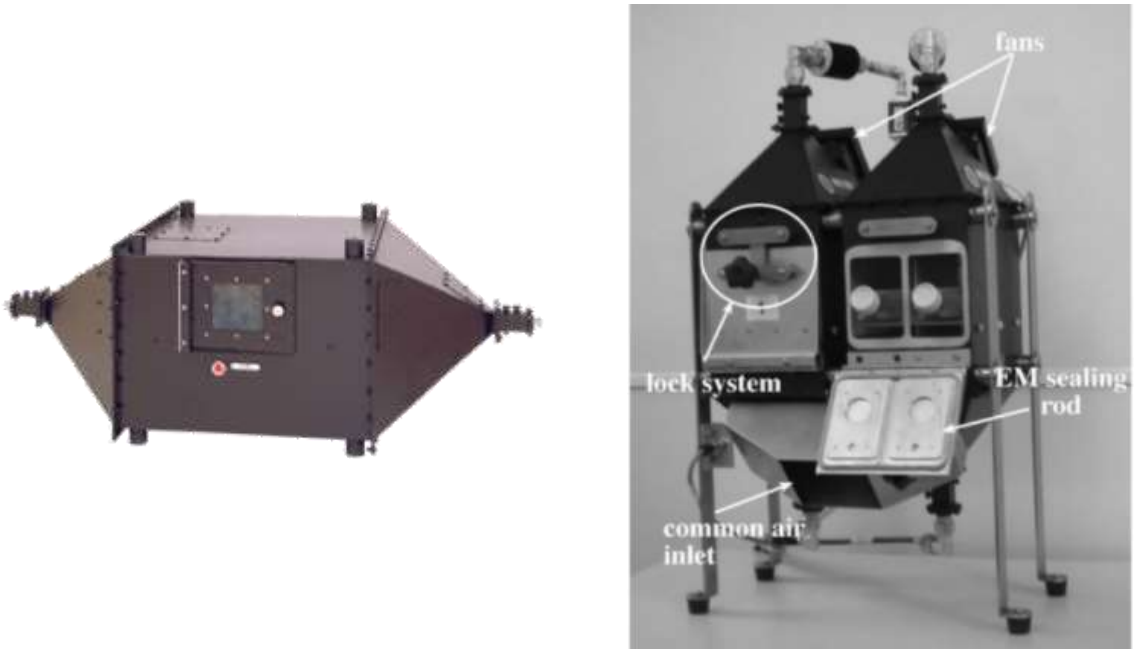


Figure 8 : Closed TEM cell with sealing for sample access [94], [95].

The TEM cell is well known for bioelectromagnetic studies and it was introduced by Myron L. Crawford in 1974. A TEM is defined as a section of coaxial transmission line with rectangular shape [96]. It was designed and developed as a close structure with a side door to permit the access to the samples (Figure 8). To respond to the EM requirements, the design of the TEM cell was optimized to maximize the operating frequency band, enlarge the exposing area, reduce the impedance mismatch, lower the voltage standing wave and improve the uniformity of the propagating wave [96]. An example of a closed TEM cell is shown in Figure 8. The TEM cell is composed of four outer walls with a central transmission line called septum. This section is tapered at the extremities with pyramidal ends which make the transition to standard 50 Ω coaxial connectors and allows the coupling with the appropriate output load typically 50 Ω. TEM mode propagates within the apparatus for a wide frequency range which prevents the losses from higher modes. The E-field within this exposure device is homogenous and uniform at the center of the TEM cell. Near the walls the E-field pattern can distort and decrease rapidly [97]. The E-field is also confined and shielded within the apparatus, therefore limiting the interferences.

TEM cells have been exploited as a test device to evaluate the electromagnetic compatibility (EMC) of RF devices due to their ability to generate plane waves in the field of

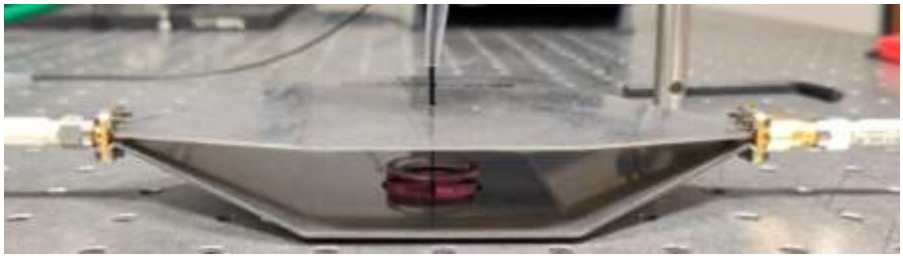

Figure 9 : Open TEM cell used for *in vitro* Bioelectromagnetic studies.

interest [98]. The operating frequency band of the TEM mode goes from 0 Hz (DC) to a few MHz and the maximum value can be increased to the GHz by diminishing the TEM cell size. In this case, the small size of the TEM cell can be limiting in terms of the number of exposed containers. The device is known for its large capacity to expose simultaneously multiple cell containers of different types such as flasks, petri dishes, tubes and cuvettes and multiwells.

Closed TEM cells are non-invasive exposure systems suitable for bioelectromagnetic studies. They have been used intensively for *in vivo* [99], [100] and *in vitro* [94], [101], [102] experiments to investigate the biological effects of RF EMFs.

Open TEM cell structures were also designed as well as illustrated in Figure 9. It consists of a triplate transmission line with the outer plates connected to the ground and the septum in between. They offer easier access to the samples, are mostly used for *in vitro* experiments [103]–[105] and can be placed within an incubator for better temperature control. The open structure was even suitable for the application of pulsed E-field [106]. For both close and open structures, modifications are needed to perform real-time measurements, for example, creating holes for probes insertion and for microscopic observation.

The second category of exposure apparatus assigned for bioelectromagnetic research is the resonant devices category.

#### I.2.1.2. Resonant exposure devices

They are called resonant devices because they operate around a precise frequency band called resonant frequency band determined by the device dimensions and characteristics. Among the most known resonant exposure devices for biological studies are the short-circuited waveguide (Figure 10) and the wire patch cell (Figure 11). Short-circuiting one of the waveguide ends by a metal plate enhances its efficiency. To increase the EM coupling with the

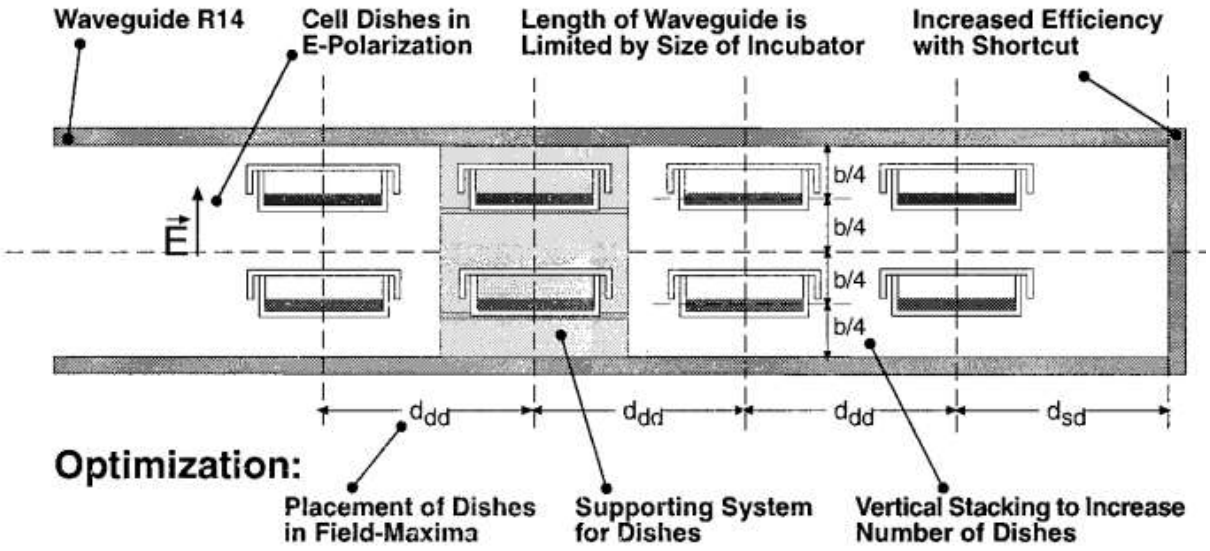


Figure 10 : Short circuited rectangular waveguide, optimization of the system [107].

biological target, the dish containing the sample should be placed at the maxima of the standing wave field and exposed in E-polarization [107]. This exposure device, illustrated in Figure 10, is suitable for multiple samples simultaneous exposure at mobile signal frequencies [108]. Also, biological dishes can be stacked above each other within the waveguide to increase the number of exposure samples in a way that does not perturb the E-field and cause additional losses. The EM field within this type of waveguides can be generated from one or both sides of the device using excitation probes [109].

The wire patch cell was introduced by Laval et al. as two rectangular plates shorted together to the ground by metallic pins or wires [110] as depicted in Figure 11. The feeding source consists of a coaxial cable inserted at the center of the cell from the top plate. The external conductor of the coaxial cable is connected to the upper plate and the central conductor is coupled with the bottom plate of the device. This device was designed based on the wire patch antenna developed by Delaveaud et al. which has the structure of a classic microstrip patch antenna [111]. The numerical and experimental evaluation of the exposure device showed good uniformity of E-field around the feeding cable that lowers at the edge of the device. Since it is an open structure the field can radiate outside, hence, absorbing materials might be needed during *in vitro* experiments. The wire patch cell offers a large test area that can fit multiple dishes. At 1800 MHz, it showed good efficiency and E-field homogeneity with four petri dishes [112]. At 900 MHz, due to the dimensions optimization, it allowed the insertion of eight 35 mm

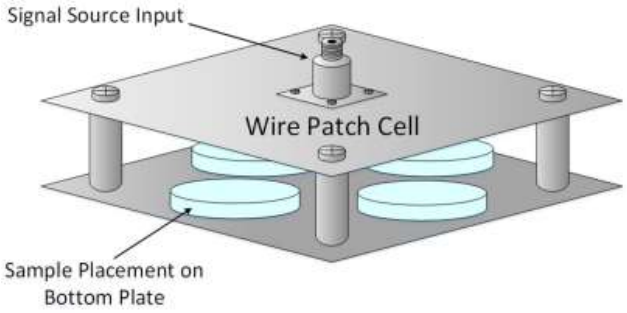


Figure 11 : Wire patch cell exposure device for *in vitro* experiments according to [86].

petri dishes. To optimize the absorption homogeneity each of these dishes was placed inside a 50 mm petri dish [110].

Another category of exposure devices used for bioelectromagnetic studies is radiating devices briefly introduced hereafter.

#### I.2.1.3. Radiating exposure devices

Radiating systems emit EMFs in a large open area and the exposure of the biological target is performed in the far field of the system. Horn antennas and microstrip antennas are among the most used radiating exposure devices for bioelectromagnetic research. Horn antennas are large thus being limited for use within an incubator. Therefore, these antennas are often used within an anechoic chamber [86]. This latter is a room with absorbents set on its walls to absorb the reflected EM waves. By eliminating the reflected energy, the absorbents protect the experimental equipment from EM interferences and guarantee the accuracy of the experiments. E-field emitted from a horn antenna (Figure 12) is quite homogenous but has low efficiency. Thus, Iyama et al. optimized the exposure setup by inserting a dielectric lens between the antenna and the culture medium to focus the energy in the direction of the sample and enhance the efficiency of the E-field [113]. This type of antenna can expose multiple samples simultaneously in far field conditions. For example, *in vivo* studies were conducted on eight rats at 900 MHz [114] and *in vitro* experiments were performed as well on several containers with biological cells [115], [116] such as multi-well culture plates, petri dishes, flasks, etc.

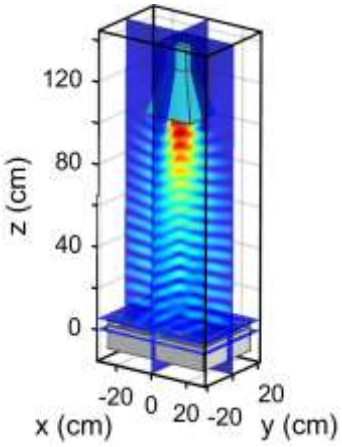


Figure 12 : E-field radiation from a horn antenna.

Microstrip antennas (Figure 13) have smaller dimensions, lower fabrication costs and are easy to manufacture. They are printed on a Printed circuit board (PCB) and due to their low volume, they can operate at the ultra-high frequency (UHF) range. Araneo et al. characterized a set of six microstrip antennas placed on the faces of a cubic box and reported their suitability for long-term biological experiments [117]. A microstrip patch antenna was used as well to measure the power received by unrestrained mice during their exposure to 2.45 GHz signals [118].

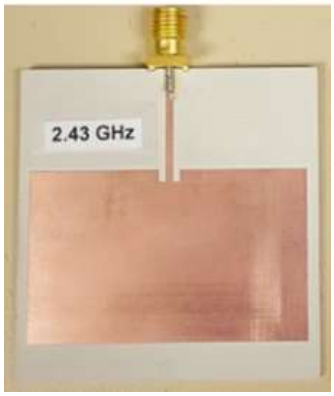


Figure 13 : A microstrip patch antenna operating at 2.43 GHz [86].

The exposure devices aforementioned are generally used to apply continuous EMF and study the induced heat and its biological effects on cells. Few devices were utilized as well for *in vivo* experiments due to their large size.

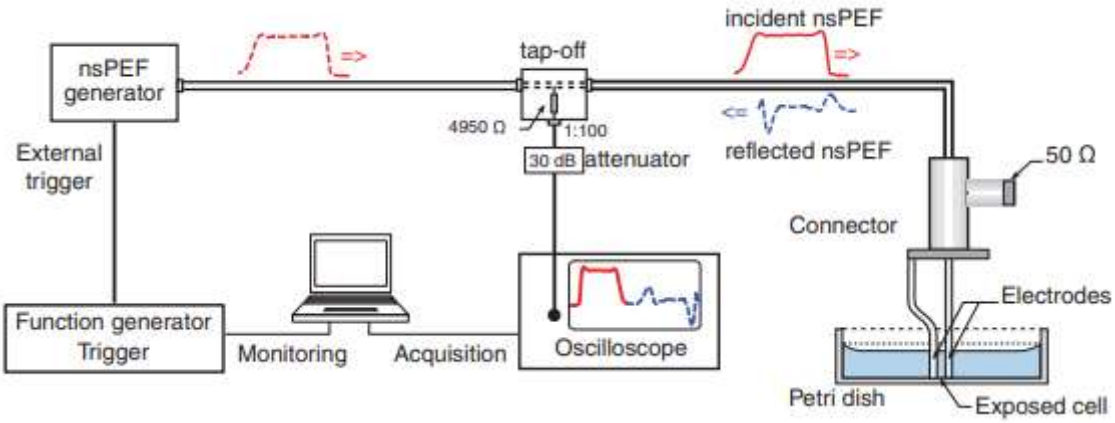


Figure 14 : Exposure setup for nsPEF application through the wire electrode apparatus.

Another set of exposure devices were developed for the application of pulsed E-field specifically nsPEFs to investigate the nanoporation and study other biological effects evoked by the PEFs.

### I.2.1.4. Pulsed electric fields exposure devices

Contact exposure devices are the systems that need to be in contact with the biological medium for exposure. At low frequency range, the PEF exposure devices may have an impedance that reaches 50 Ω when they are filled or submerged in the medium. They also can present a low impedance or a high impedance that can be matched by connecting a 50 Ω in parallel. Contact exposure devices are based on electrodes and are generally developed to apply PEF. The E-field application is achieved by creating a potential difference between the electrodes of the device. Thus, one is connected to the feed line and the other to the reference (ground). The PEF exposure setup is different from the one used for continuous EMF and it contains specific high-frequency, high-voltage components. Figure 14 illustrates the nsPEF exposure setup that consists of the nsPEF generator followed by a tap-off to monitor the incident and reflected pulses through an oscilloscope. The tap-off is also connected to the delivery device in this schematics which is the wire electrodes submerged in the biological medium. Since the delivery device has a high impedance, it is coupled in parallel with a 50 Ω resistor. The volume of the exposed area depends on the shape and the structure of the electrodes (e.g. wires, planar, etc). In the PEF exposure devices category, there are wire electrodes [119]–[122], electroporation cuvettes [123]–[125], microchambers [126], microfluidic channels [127]–

[129], etc. The contact PEF exposure devices that will be presented afterward are designed to apply PEFs created by electric pulses with durations higher than a few ns up to about 100 ns.

Wire Electrodes based systems

Wire electrodes based exposure devices can only expose a small number of cells due to the reduced electrodes size and a small exposed area. These devices are generally attached to a micromanipulator and set on a microscope stage allowing a precise positioning of the electrodes around cells. They are designed to apply ultra-short duration PEF with high intensities with MV/m (tens of kV/cm) magnitude.

A microsystem with tungsten electrodes depicted in Figure 15 was developed by Pakhomov et al. to study the *in situ* response of a single cell to nsPEF [130]. Pulses of 60 ns duration were applied to the cell placed within the 0.31 mm gap between the tungsten electrodes. E-field level that can be generated between the electrodes tips was determined by numerical simulations to be in the 20 – 24 kV/cm range per 1 kV applied voltage. As the pulses transmitted to the exposure device have an amplitude between 540 – 580 V, the cells were exposed to an E-field with 12 kV/cm intensity.

A similar microsystem displayed in Figure 15 was developed to expose a higher number of cells simultaneously and it is also based on tungsten electrodes [120]. The electrodes are gold plated to guaranty biocompatibility, they have 100 µm diameter and the distance between the electrodes is 100 µm. They are covered in silicon and sealed with epoxy adhesive to maintain their parallel alignment. This device is suitable for the application of ultra-short pulses of 2.5 - 5 ns duration with intensities up to 1.2 kV. The E-field generated between the electrodes is homogenous according to the numerical characterization.

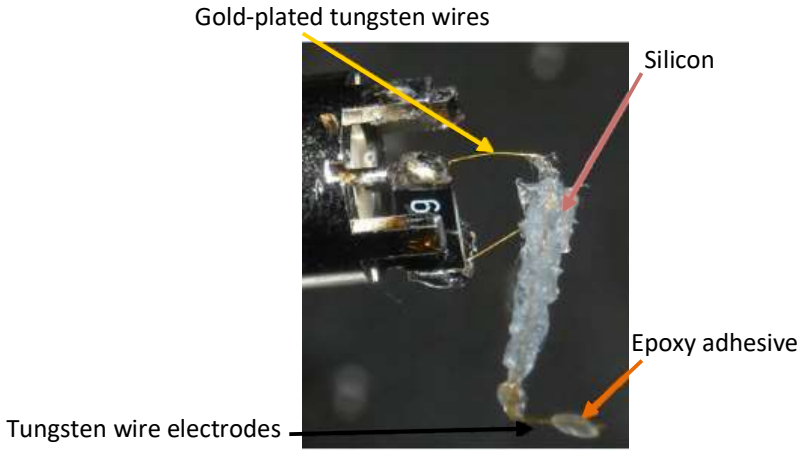


Figure 15 : nsPEF exposure microsystem with tungsten wire electrodes [120].

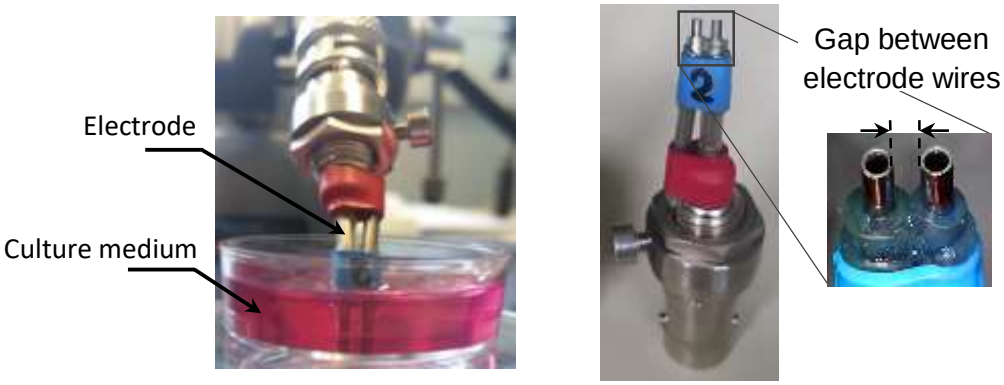


Figure 16 : Wire steel electrodes with round tips for nsPEF exposure [122].

A third wire electrode device is shown in Figure 16 and

Figure 17 where each electrode is a stainless steel hollow tube [122]. The upper part of the electrodes is covered with insulating material to avoid the breakdown of the device and only the tips are used to apply the EF. They can make an angle of about 45° compared to the rest of the device and can take different forms. The wire electrode device with round tips (Figure 16) were positioned to touch the bottom of the medium dish and to be orthogonal to the cell layer [121]. The E-field spatial distribution was evaluated numerically between the electrodes to study its homogeneity in the exposure area. E field amplitude ranged between 35 – 45 kV/cm at the cell level. In [119], the exposure device tips were flattened (Figure 17) and placed at the bottom of the medium dish but parallel to the cell layer. Simulations showed that the E-field was quite homogenous along the tips' length and in the middle of the gap.

a) b)

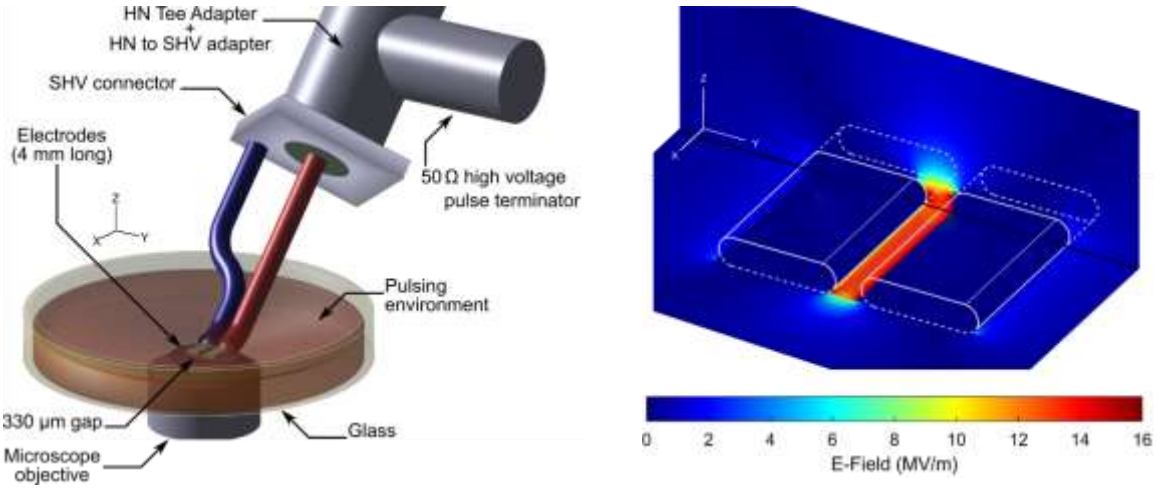


Figure 17 : a) wire steel electrodes with flat tips for nsPEF exposure, b) E-field distribution at the tip of the electrodes [131].

Another contact nsPEF exposure device based on planar electrodes was characterized and used by our group which is the electroporation cuvette presented below.

Electroporation cuvette

The electroporation cuvette is a planar exposure device that consists of two parallel metal plate electrodes in a rectangular section plastic tube [124]. The space between the two electrodes in Figure 18a is filled with the biological medium. The advantage of this device is that it allows the exposure of a large number of cells. The applied field is homogenous and uniform between the electrodes. The cuvette with 1 mm gap can support high intensity pulses up to 5 kV which generates an E-field intensity of 30 - 40 kV/cm [132], [123], [125]. The electroporation cuvette is suitable for pulses with durations down to 3 ns, however, it is not suitable for real-time microscopic observation. Figure 18b shows the connecting transition between the cuvette and the feeding line that consists of two metal plates placed on both sides of the device.

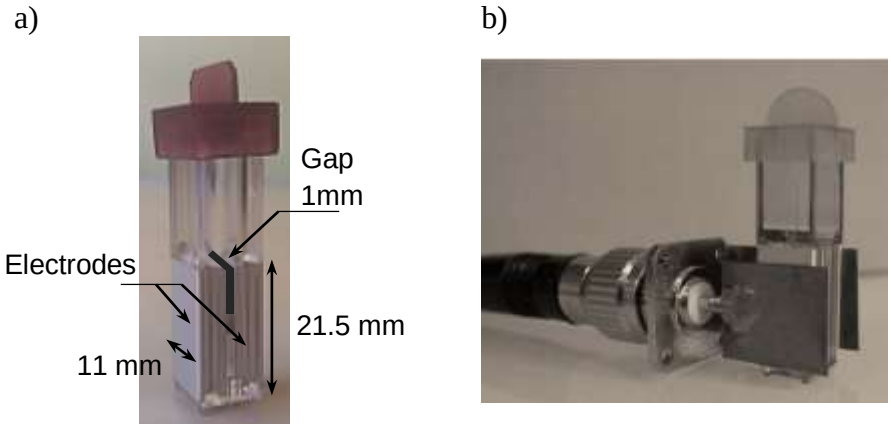


Figure 18 : a) Electroporation cuvette, b) connection of the cuvette to the feeding coaxial cable by two metal plates [125].

For the application of nsPEF, several devices were developed at different scales. For example, the devices mentioned above were fabricated with millimetric dimensions. For the same objective of studying the effects of the nsPEFs, microscale exposure devices were developed as well and characterized such as microchambers and microfluidic channels.

Microfluidic channel / microchamber

These microsystems are based on planar microelectrodes, microfabricated by photolithography technology. They are characterized by the application of an intense, uniform, and homogeneous E-field [133]. Their structure was designed according to the biological and EM requirements such as: an appropriate interelectrode distance allowing the accommodation of cells and the generation of E-field of MV/m intensity and a sufficient channel length allowing the observation of a reasonable number of cells. For real-time microscopic observation, the substrate is transparent to light from ultraviolet to visible and does not fluoresce under the excitation of the microscope [126]. Casciola et al. designed a versatile high voltage microchamber [127], shown in Figure 19b, comprised of two transmission lines based on microstrip planar technology. nsPEF are applied to the planar electrodes with 1 to 3 ns pulse durations and the system can expose a single cell or multi-cells depending on the direction of the channel (longitudinal or transversal). Besides that, the microchamber can operate in fluidic conditions.

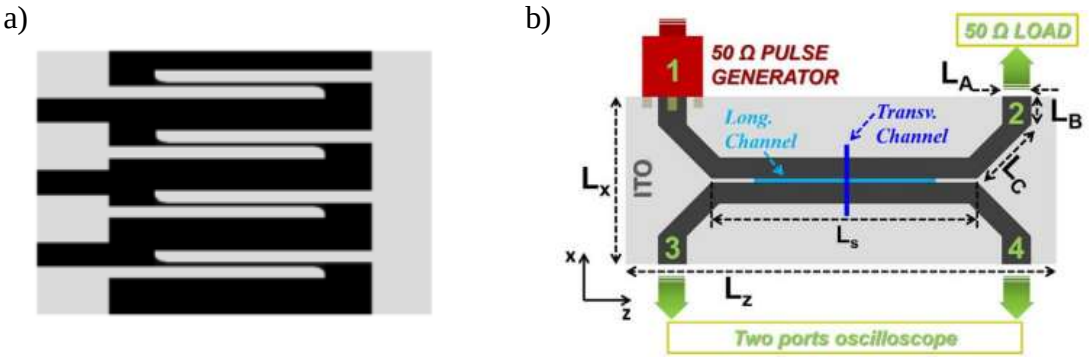


Figure 19 : Microchamber exposure devices, a) multielectrode microchamber [126], b) versatile microchamber with two stripline electrodes operating by coupling [127].

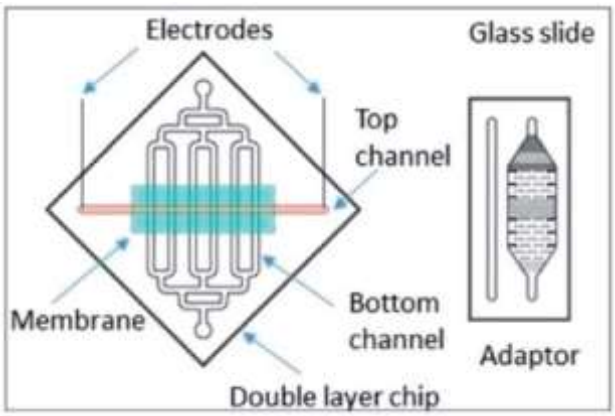


Figure 20 : Schematic of the double layer microfluidic device [134].

Microfluidic channel biochips allow the exposure of cells within a well-controlled fluidic microenvironment. They are designed and optimized for cell analysis [135], [136] and other therapeutic applications (e.g. transfection). Bonakdar et al. [134] developed and fabricated a double layer microfluidic device (Figure 20) to study the permeabilization of the blood-brain barrier under pulsed electric field exposure. The bottom stage contains an array of 6 parallel channels, 800 µm width each and the top stage comprises one 1-mm wide channel perpendicular to the bottom ones. High voltage pulses applied have 100 µs duration and they generate an E-field of 833 V/cm intensity inducing the electroporation of the cells. Low voltage high repetition rate pulses applied continuously caused the increase of cell permeabilization under 25 V/cm E-field level. The microfluidic channel chip of Figure 21 was fabricated, studied, optimized and validated for biological *in vitro* investigations with nsPEF [128], [129]. It was used to apply square shape pulses last for 3 ns or 10 ns with E-field amplitude ranging between 20 and 45 kV/cm. Based on this device, the nsPEF effect on cell permeabilization was investigated with Chinese hamster fibroblast lung cells.

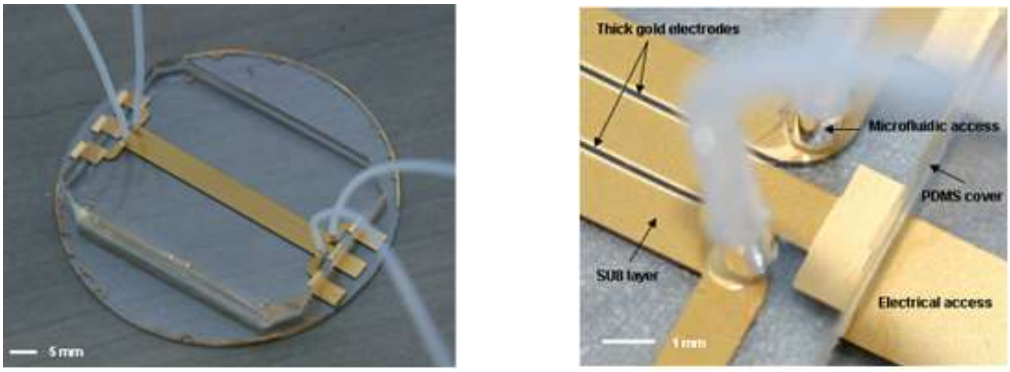


Figure 21 : Photos of the microfabricated microfluidic channel chip, top full view and closeup on the input access [128].

The nsPEFs exposure devices are generally the ones that needs to be in contact with the medium, they expose a small number of cells and are suitable to study the effects of ns pulses on the biological cell including electroporation and other non-thermal effects.

## Conclusion

This chapter presented the general context of the bioelectromagnetic studies performed during this thesis. Communication technology has seen explosive growth during the last few decades. It progressed through a sequence of generation bands from the 1st generation to the 5th generation of nowadays providing better quality services with higher speed data, better coverage and availability. This caused the setup of more equipment inducing the rise of public concerns about the health risks of long-term exposure. Applying EMFs with high intensities exceeding the basic restrictions set by the ICNIRP can cause thermal effects by increasing the local or the whole body temperature. Excessive heat may as well results in other biological changes at the cellular level.

Research studies investigated the different potential non-thermal health effects through epidemiological, clinical and experimental assessments of continuous and pulsed E-field. From the results, it has not been evidenced to date that exposure to continuous mobile communication signals induces risks such as brain electrical activity alteration, sleep disturbance and tumor initiation or growth. The studies that focused on the pulsed E-fields and their impact on the biological cells concluded that high exposure levels above the limits were shown to induce

thermal effects on the samples. Other investigations focused on the non-thermal effects of pulsed E-fields showing that high intensity (up to 10 kV) short pulses (µs - ms) increases the cell plasma membrane permeabilization called electroporation. Ultra-high intensity (> 10 kV) ultra-short pulses (sub-ns - ns) can permeabilize the membranes of the organelles as well. Countless studies focused on the pulsed E-fields and their impact on the biological cells for therapeutically purposes. The electroporation was exploited for numerous therapeutical applications such as tumor ablation, drug delivery and gene therapy also for food processing procedures.

Bioelectromagnetic studies involve simultaneously a constant link of biology, electromagnetism and medical fields to investigate the interaction between the EMFs and the biological entities, determine the effects that can cause health risks and those that are beneficial for therapeutic and medical applications. The biological and electromagnetic *in vitro* experimental studies require specific setups for the exposure of the biological sample and the achievement of the dosimetry including the detection and the observation of the biological effects induced. Various exposure devices were designed for BioEM studies and therefore four different categories were defined (i.e. propagating, resonant, radiating and contact PEF exposure devices). The most known devices of each category were described with a focus on the systems further studied in the context of my thesis.

The next chapter details the objectives of this thesis, the different methods and techniques available for experimental investigations.

# Chapter II.

## Dosimetry materials and methods

# Introduction

Our studies within the Bioelectromagnetic field are focused on the RF-EMFs effects on biological samples at the cellular level mainly at 1.8 GHz. This frequency represents one of the operating frequencies of the 2G and 3G mobile communication bands in Europe. Studies are still ongoing and focusing for example on the detrimental effects on neuronal cells due to the daily use of phones at proximity from the brain. Neurons are the target of our investigations since they are excitable cells, they are the basic working unit of the brain and they help coordinate all of the necessary functions of life.

To detect the microscopic biological changes induced on the neuronal network by RF exposures specifically, relevant techniques should be adopted with suitable devices. Thus, the local energy absorbed by the biological target at the cellular scale should be determined during the EMFs application. SAR values needed can be determined experimentally with direct measurements and numerically with simulation softwares.

The numerical modelling and simulations used for the design and these investigations will be first presented in this chapter as well as the different extracted types of SAR. The experimental methods for SAR retrieval will be also described. To bypass the limitations presented by some standard measuring tools such as the resolution, the accuracy and the size, developed microscopy experimental techniques that are temperature-dependent will be presented. These techniques can be used to detect biological changes at the microscopic level. The microscopy technique adopted required calibration and characterization to study its sensitivity to the exposure parameters. All these assessments are conducted at a macroscopic scale. Therefore, a conversion method needs to be defined to allow the exploitation of the microscopy technique outcomes to determine the SAR at the cellular level.

To conduct the *in vitro* experimental investigation, the exposure setup including the exposure device, the measurement tools and the microscopy technique selected will be detailed.

# II.1. Context and objectives

The dosimetry of the exposure system is typically achieved through the assessment of the E-field generated within the exposure device and applied to the biological target and through the temperature variation detection within the biological sample during the RF exposure. In our case, the E-field is evaluated numerically with a simulation software and the temperature is measured with several methods and techniques. The E-field and temperature data collected are used to determine the SAR values as detailed in equation ( 3 ) and ( 4 ) of section I.1.3.

## II.1.1. Design modelling and simulation software

Numerical simulations allow the analysis and optimization of components and systems in their environment. From the early stage of system development, potential issues can be identified and avoided. To investigate the E-field and SAR behavior through the spatial distribution of our RF devices, a reliable computational tool is needed. For these matters, CST Microwave Studio (MWS) 2017 (Computer Simulation Technology [CST], Dassault Systems, Darmstadt, Germany) was used [137]. CST is a 3D Electromagnetic high performance analysis software for high frequency components. It includes a biomedical workflow that facilitates the study of biological interaction with electromagnetic fields and offers CAD-based and voxel-based biological models and biomedical examples. A material library is present with a wide choice of tissue types pre-defined by their properties. Designs can be meshed with various strategies and approaches as well as various mesh types which include, for volumes, hexahedral and tetrahedral meshes, and for surfaces, hybrid triangular and quadrilateral meshes. CST is selected for its wide range of solver technologies chosen according to the applications. The most commonly used solvers are the general purpose time and frequency domain solvers. The time domain approach is exploited to simulate in a large frequency bands and the second solver is for narrow frequency bands as it discretizes the entire frequency band. CST is able to simulate complex structures and directly calculate all SAR types (i.e. point SAR, whole-body SAR, etc.).

## II.1.2. SAR types

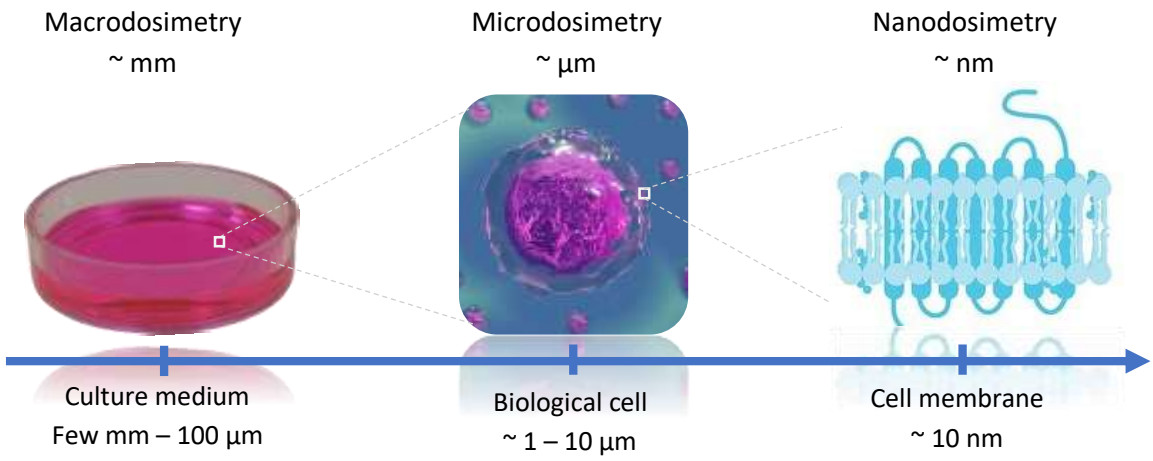


Figure 22 : Schematic representation of multiscale dosimetry, macroscale dosimetry correspond to the investigations averaged at the whole biological sample, microdosimetry interests at the single-cell changes and nanoscale dosimetry focuses at the nanometric scale changes (e.g. cell membrane) [138].

Dosimetry can be achieved at different scales depending on the biological target, the experiment type and the exposure device structure. As depicted in Figure 22, dosimetry at the macroscopic scale corresponds to the investigations performed at a large scale (i.e. centimetric and millimetric). It informs about the effects induced within a large volume such as the whole culture medium. The investigations at the microscopic scale focus on the observation and the detection of the changes at the single-cell level. Microdosimetry is also conducted for fine characterization when using microsystems for RF exposure. The nanoscale dosimetry allows the detection of biological effects at the nanometric scale such as the changes occurring at the cell membrane.

Depending on the biological volume to study, different types of SAR values are required. Our investigations are based on four SAR values at different scales namely the SAR volume, the SAR probe, the SAR bottom and the local SAR. Figure 23 illustrates the defined SAR values and their corresponding volumes. The SAR volume represents the energy absorbed by the biological medium averaged on the total volume of the sample. This value informs about the thermal variation within the whole volume and can be retrieved only with numerical simulation. The SAR probe corresponds to the SAR value averaged over the measuring volume of a temperature probe used experimentally hence the name SAR probe. SAR probe can also

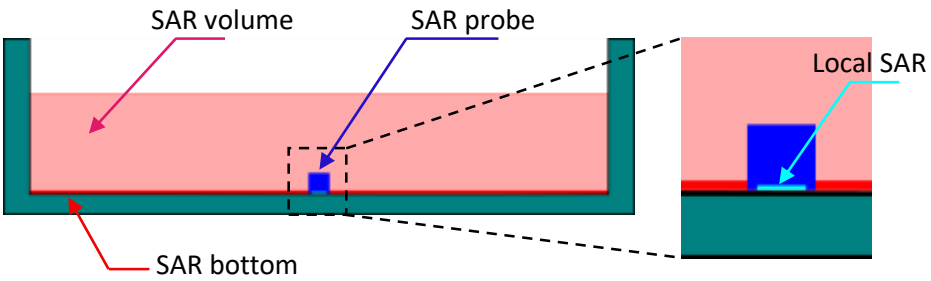


Figure 23 : Scale difference of the volumes from which SAR values are retrieved.

be determined numerically to allow the comparison with the experimental results. The SAR bottom is the SAR at the cells layer obtained by averaging the numerical SAR values over the bottom layer of the sample with a certain thickness, typically about 100 µm. The local SAR is retrieved from a small micrometric volume ($\leq 0.01$ mm$^3$). It is possible to determine this SAR value with microscopy techniques and compare the outcomes with the numerical ones.

A main objective of our study is to achieve microscale dosimetry. Thus, it is essential to develop and evaluate a techniques for microscopic assessments. First, based on the macroscale dosimetry methods, the exposure system needs to be evaluated. For this matter, the microscale measurement devices are presented below by detailing their advantages and limitations.

# II.2. Experimental material and methods

## II.2.1. SAR measurements probes

Measurements at the macroscopic scale are performed directly using probes. For SAR retrieval, some probes can provide SAR values by measuring the E-field within the biological sample and computing the SAR probe values. These types of SAR probes such as those designed by SPEAG [139] and MVG (Microwave vision group) [140] have good dynamic range and low interference with the E-field measured and allow measurements in liquids or in the air. However, they are limiting due to their size as their measuring tips have dimensions of a few millimeters (1.2 – 5 mm) in diameter which makes the probes significantly large for microscopic assessments.

## II.2.2. Temperature probes

Various methods can be exploited to assess the *in situ* temperature variation within the biological solution. Amongst the measuring sensors that are widely used, there are infrared cameras, thermistors, thermocouples and fiber optic probes. The infrared or thermographic cameras provide a temperature map with high resolution [141] by recording the infrared radiation emitted from the biological sample surface. These thermal cameras measure simultaneously the surface radiation of multiple subjects. However, they are not suitable for *in vitro* experiments where temperature needs to be detected within the biological tissues or at the cell layer in the liquid medium.

The thermistors [142] are semiconductor sensors whose resistance depends on the temperature. They are known for their high negative temperature coefficient meaning that their resistance decreases with the temperature increase. Thermistors sensitivity to temperature change ranges between -3%/°C and -6 %/°C [143], [144]. They offer high temperature precision of ± 0.1°C and fast response. They are manufactured in different sizes down to 0.1 mm. However, in an EM environment, the metal parts of the thermistor interfere with the EMFs resulting in erroneous temperature values [145]. Hence, this type of sensor is not adequate for local temperature detection during RF exposure.

A thermocouple is a thermoelectric transducer designed with two different metals welded together at one of the extremities. This sensor can measure the temperature in liquids, air and atmosphere providing accurate results. For microscale investigations, micro-thermocouples were manufactured with different diameter sizes (25, 50, 75 µm, etc.). The temperature outcomes accuracy was shown to be dependent on the thermosensor size [146]. Most accurate values were obtained with the 25 µm sized micro-thermocouple. However, the major limitation of this probe is that it distorts the E-field due to the sensor metal parts [147]. Particularly, an increase of the E-field local values was observed when placing the thermocouple parallel to the E-field. No significant impact is observed when the probe is perpendicular to the E-field but this measuring condition is not compatible with all experimental setups.

Optical fiber probes are non-perturbing RF thermometers because they do not include any metal parts [145]. These thermosensors are mainly based on glass or plastic fibers with a light source (LED, laser, etc.) connected at one end of the fiber and a temperature-dependent

crystal attached to the other end. The light propagates from the source through the optical fiber to the crystal and depending on the nature and the properties of the crystal (phosphors, semiconductor, etc.) [148], the crystal responds by emitting an optical signal through the fiber. The *in-situ* temperature results are provided from the reflected light analysis. These probes have a thermal precision of ± 0.1 °C [145] and they are available in different sizes down to 0.25 mm [149]. Their major advantage is their total immunity to EM interferences making them suitable for measurements in a strong EM environment.

## II.2.3. Microscale temperature assessment techniques

### II.2.3.1. Phosphorescent dyes

Monitoring temperature in real-time with micrometer spatial resolution can be achieved through thermosensitive dyes marking the biological sample or the device under measurement. Temperature-dependent phosphorescence intensity of Europium Thenoyl-Trifluoro-Acetonate (EuTTA) has been used by Kolodner et al. [150], [151] to record in high resolution (i.e. 0.01°C) the surface temperature distribution of integrated circuits. This dye was integrated within Chinese hamster ovary cells to image the intracellular heat evoked [151]. EuTTA intensity is temperature-dependent in the range 15 – 40°C. With temperature increase, phosphorescence quantum efficiency declines rapidly and emission intensity bleached more rapidly. The spatial resolution of the EuTTA technique is limited by diffraction (~300 nm) and its time resolution is limited by the sampling rate [151]. EuTTA is a rare earth element that has low thermal conductivity and is absorbed unevenly into the membrane and the organelles, and most of all that it can be toxic to the cells [152]. Thus, organic fluorescent temperature-dependent dyes were investigated.

### II.2.3.2. Organic fluorescent laser dyes

Genetics and cell biology studies rely heavily on the organic fluorescent laser dyes due to their extremely sensitive emission profiles and their high spatial resolution. They are characterized by a strong absorption band in the visible region of the electromagnetic spectrum [153]. Fluorescence characteristics of some commonly used fluorophores were investigated. Fluorescence intensity of labels such as Carbocyanide (Cy3) (Figure 24), FITC (fluorescein

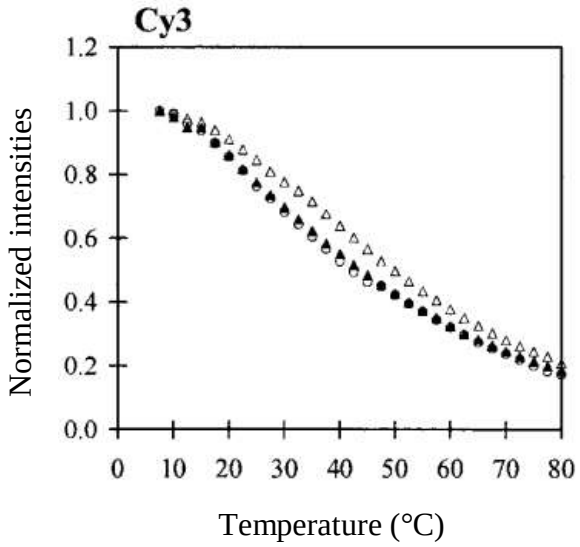


Figure 24 : Normalized fluorescence intensities of Carbocyanide (Cy3) as a function of temperature.

isothiocyanate) and TAMRA (tetramethylrhodamine) showed important temperature dependency [154]. Their fluorescence intensity reduced by 56 – 82 % from their initial normalized values within the 7.5 – 80°C temperature range.

Ideally, the fluorescence quantum yield of a laser dye should reach a value near 100% at low temperature and lowers to a few percentages at the boiling temperature of the solution [153]. The quantum yield is defined as the efficiency of converting absorbed light into emitted light, which can be in the form of fluorescence [155]. Rhodamines fluorescent dyes are well known for their quantum yield values that are nearly 100 % at low temperatures. Kubin et al. [156] determined the quantum yields of several Rhodamine dyes (Rhod-6G, Rhod-101 and Rhod-110) at 25°C to find 95 %, 96 % and 92 %, respectively. In [157], they reported that the Rhod-110 is temperature-independent because its quantum yield is constant over a wide range of temperature.

Numerous research focused on the fluorescence characteristics of the Rhodamine B (Rhod-B) because it is water-soluble and it was reported that it has a constant quantum yield over a wide wavelength range [157]. Its absorption peak is at 554 nm and its fluorescence peak is at 627 nm. From the literature, the fluorescence quantum yield of Rhod-B ranges from 60% [153] to 97% [158]. Figure 25 illustrates the Rhod-B dependency on temperature. Measurements of Kubin et al. [145] show that at 10°C, the quantum yield is about 80 % and decreases to 35% at high temperatures. Other values within this temperature range were

reported in [156], [159] proving that this disparity can be ascribed to the different experimental parameters (i.e. temperature and the dye concentration of the biological solution).

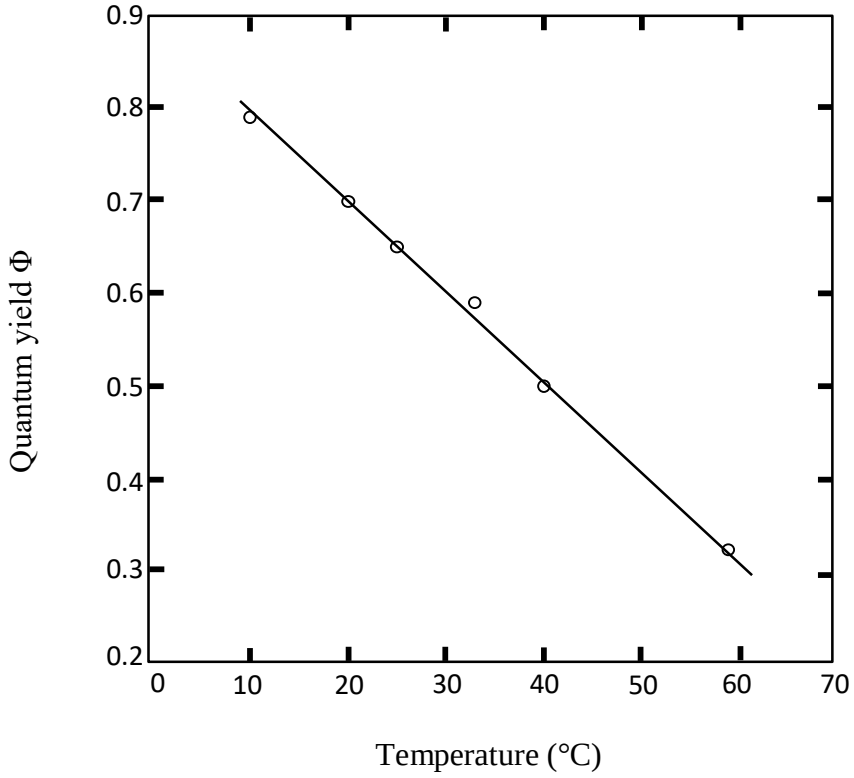


Figure 25 : Rhodamine B quantum yield Φ variation in function of the temperature [156].

Overall, the quantum yield curve of Rhod-B starts at, virtually, 100 % for low temperatures then decreases to a few percentages at around 70°C. Moreover, its strong temperature dependency in aqueous solutions [160], its pH independency above a pH of 6 and its trivial pressure sensitivity [161] makes it a highly recommended candidate for microsystems characterization, thermal effects assessments due to RF exposure and for other biological changes induced at the cellular level.

In an aqueous medium, fluorescence intensity $I$ is dependent mainly on the exciting light intensity and the fluorescent dye characteristics [159], [162]. Their relation is described by equation ( 5 ).

$$I = I_0 \, A\Phi \, \varepsilon \, DC \qquad (5)$$

Where $I_0$ is the exciting laser intensity, $A$ is the fraction of available light collected, $\Phi$ is the marker's quantum yield, $\varepsilon$ is the molecular extinction coefficient, C is the concentration of the solution and $D$ is the optical depth of the solution. Fluorescence intensity depends not only on the dye characteristics but also on the excitation parameters.

When only the excitation light frequency varies, fluorescence intensity varies as well, as it becomes proportional to $\Phi\varepsilon$. However, the quantum yield of Rhod-B is approximately independent of the frequency as it is constant for an extensive wavelength range. Thus, it will only depend on $\varepsilon$ i.e. the strength of the dye on the absorbing light at a given wavelength. When the exciting intensity and frequency are kept constant, fluorescence intensity becomes proportional only to the concentration.

For all the advantages presented, Rhod-B is selected in our studies to investigate the microscale thermal effects caused by the exposure of the biological medium to RF E-fields. The exposure system assigned for these investigations requires to be equipped with microscopy measuring devices.

## II.2.4. Exposure setup

The exposure setup (Figure 26) is mainly composed of a RF signal generator (HP8648B, Hewlett-Packard, USA), followed by a 44 dB power amplifier (M.19.40.50, Nuclétudes, France) and a bidirectional coupler. Using the latter, the incident and reflected power at the input port of the exposure device were monitored through a power meter. The setup ends with a 50 Ω load connected to the output of the exposure device to absorb the transmitted wave and eliminate reflection thus possible interferences.

For local macroscopic temperature assessments during the RF signal application, an optical fiber probe is used. The probe is inserted within the medium and temperature data are registered for SAR retrieval. When microscale temperature assessments are required, the medium is marked with Rhod-B dye and fluorescence intensity is recorded with an inverted microscope.

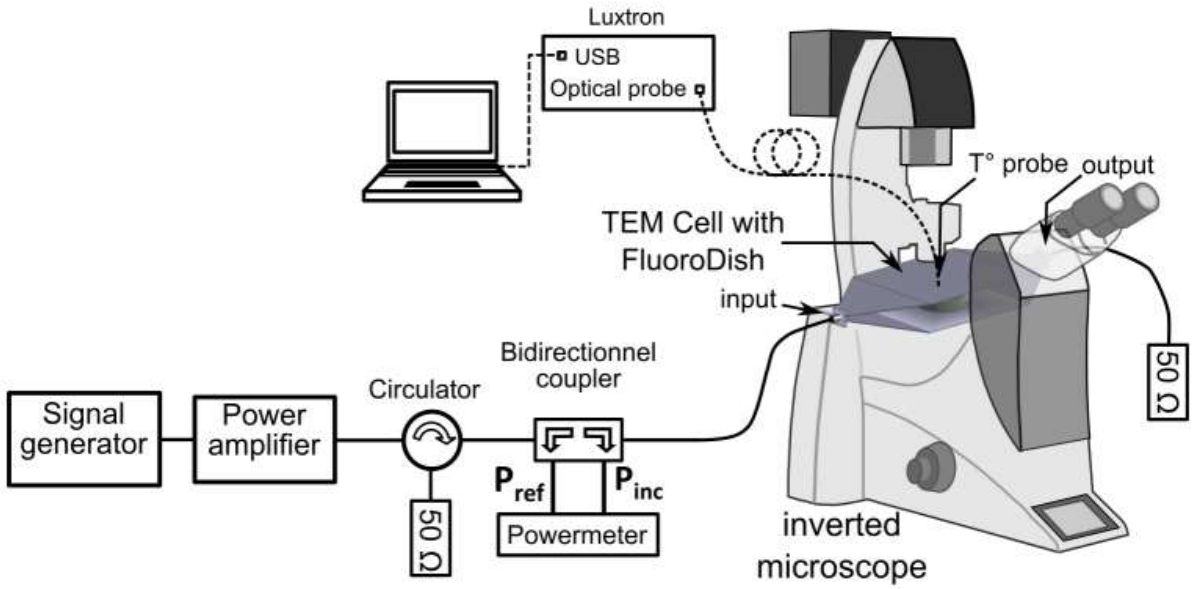


Figure 26 : EMF exposure setup with the TEM cell as an exposure device and a fiber optic probe for real-time temperature detection. Experimental real-time setup for sample RF exposure and temperature and fluorescence recordings.

### II.2.4.1. Luxtron optical fiber probe

For temperature *in situ* investigations, a fiber optic thermometer (Luxtron One, Lumasense Technologies, CA, USA) was used. This probe is non-metallic with a 0.8 mm diameter tip. The probe measures and averages the temperature over a volume that is estimated to be 1 $mm^3$ (Figure 27). It has a sampling rate of 4 samples per second. Based on a fluoroptic technology, the optical fiber probe is equipped with a sensitive phosphorescent sensor at the tip of the fiber. This sensor fluoresces when it receives light pulses from the optical fiber and the decay time of its fluorescence depends on the temperature of the medium in which it is submerged. The thermometer calculates the decay time and determines the temperature.

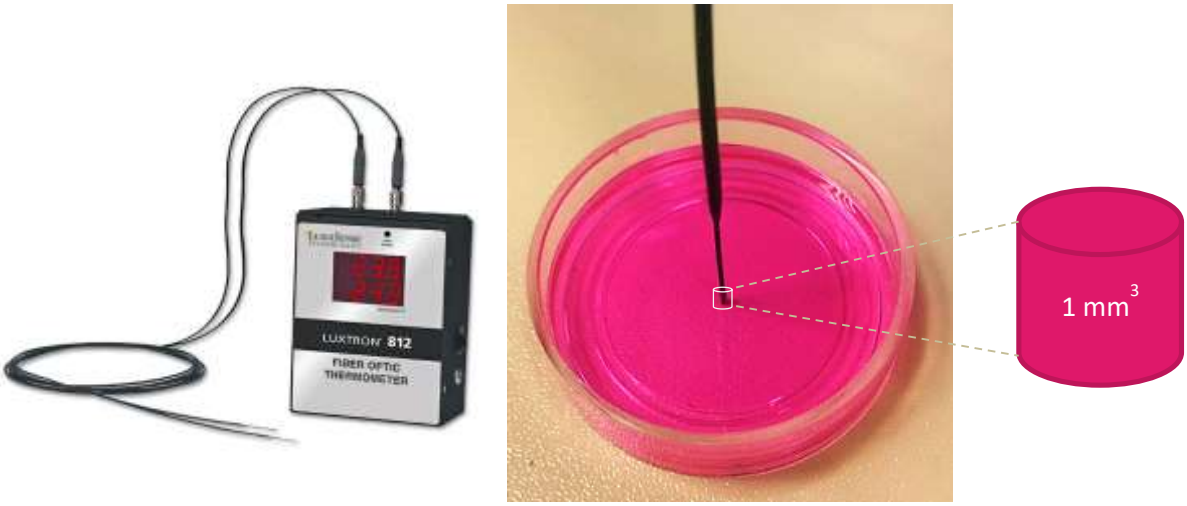


Figure 27 : Optical fiber probe immersed within the culture medium and averaging the temperature over 1 $mm^3$ volume.

### II.2.4.2. Rhodamine B fluorescence measurement technique

Rhod-B dye was selected to evaluate the microscopic thermal changes at the cellular layer. For this matter, the experimental setup is equipped with an inverted microscope (DMI6000, Leica) to record by epifluorescence the intensity of Rhod-B and observe the biological changes. During the exposure, Rhod-B excitation light is generated by a solid-state light source (Spectra 7, Lumencor) attached to the microscope with a 1 mm quartz fiber. Excitation light is separated by a dichroic beam-splitter (89100BS, Chroma) and the fluorescence light is filtered by a filter wheel (MAC 6000, Ludl). The real-time fluorescence acquisition was recorded with a camera (EMCCD Evolve 512, Roper) with 512 × 512 pixels spatial resolution. A 20x objective is used for the observation of a window of about 0.57 × 0.57 $mm^2$. The images collected are analyzed with Image Analyst MJII (Image Analyst Software, Novato, CA) to retrieve the fluorescence intensity variation curve against time.

### II.2.4.3. Radiofrequency exposure device

The RF exposure device used for experimental investigations is the open Transverse Electromagnetic (TEM) cell of Figure 28. As described in section I.2.1.1, the TEM cell is a propagating exposure device consisting of a coaxial line section of rectangular shape. The outer plates are connected to the reference (ground) and the middle plate also known as septum is connected to the feed line. The open structure was designed with no sidewalls to facilitate access to the exposed samples. The small size and the open structure allow the air circulation and

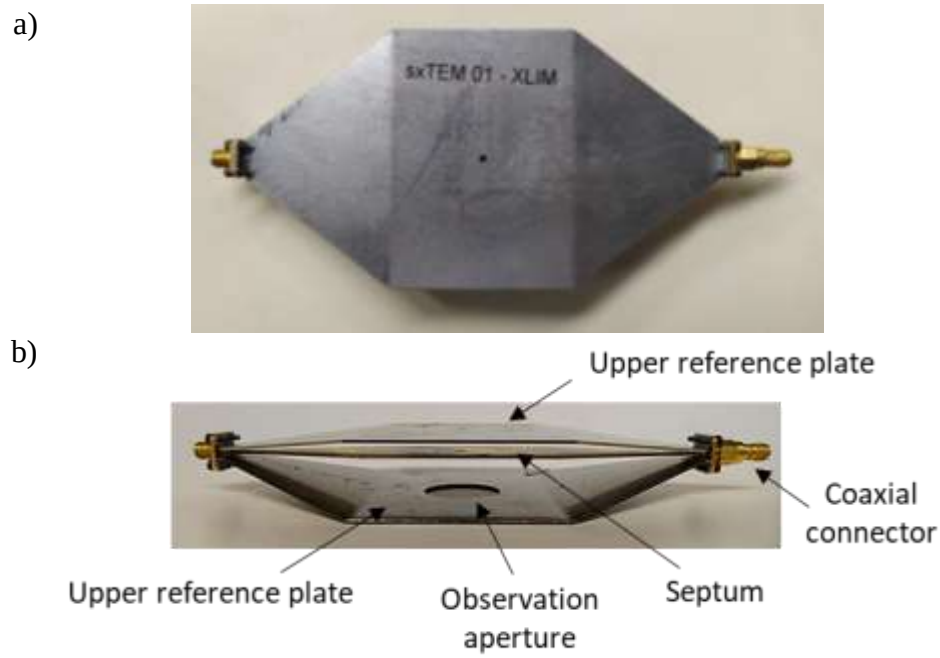


Figure 28 : Open TEM cell with apertures for probe insertion and real time observation. a) top view, b) side view.

temperature control within the device when conducting biological exposures within an incubator. Besides, the TEM cell fulfills essential EM requirements for *in vitro* investigations such as the application of a uniform and homogenous EMF at the area of interest, the device does not radiate as the E-field applied is mainly confined between the plates preventing the coupling with external equipment. Modifications were performed on the TEM delivery device to allow real-time monitoring during experiments. Small apertures were added to the septum and the upper plate to allow the insertion of the thermometer and a larger aperture was made at the lower plate for real-time observation and detection with a microscope. Soueid et al. investigated the effects of the TEM cell observation aperture on the electrical energy absorbed by the medium [163]. They concluded that sealing the aperture with an Indium tin oxide (ITO) layer limits the E-field perturbations caused by the aperture while still allowing real-time observations.

Figure 29 presents the dimensions of the TEM cell used in the experiments and numerically modelled. The side view includes the length of the TEM cell components and the distances separating the septum from the reference plates. The top view shows the width of the plates. The plates thickness is 1 mm.

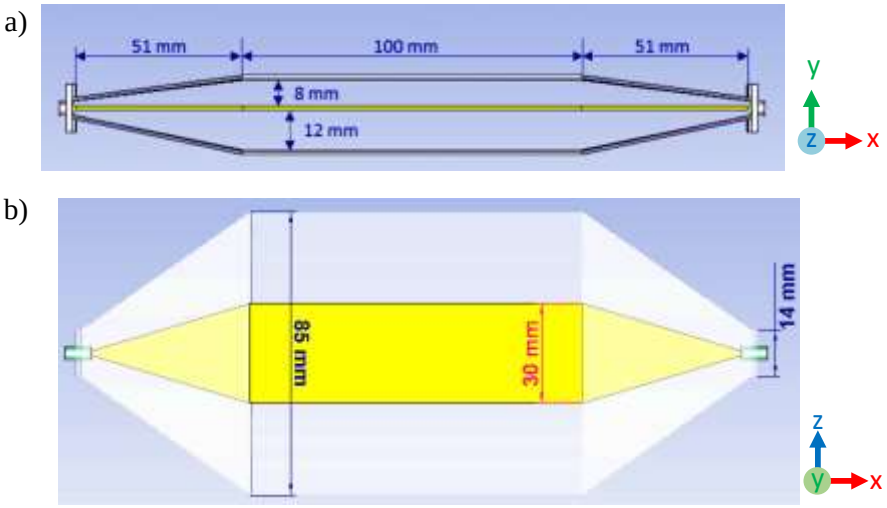


Figure 29 : Dimensions of Transverse Electromagnetic (TEM) cell exposure device, a) front view, b) top view.

Dosimetry of the exposure setup is crucial before the assessment of biological effects. It includes the characterization of the setup devices by verifying their conformity to the recommendations and the optimization of the experimental parameters for a more accurate outcome. Dosimetry typically consists of assessing the E-Field coupling with the exposed medium and retrieving the SAR induced within the sample. Moreover, a frequency characterization of the exposure device is essential to confirm their impedance match through the S parameters.

## II.2.5. TEM cell exposure device characterization

### II.2.5.1. Frequency characterization

The TEM cell was evaluated in the frequency domain by measuring the transmission and reflection coefficients with a vector network analyzer (VNA, 8753E, Hewlett Packard, USA). Figure 30 illustrates the setup used to measure the reflection $S_{11}$ and transmission $S_{21}$ coefficients of the TEM cell. These assessments were conducted when the TEM cell was empty and when it contained a holder with biological medium (3 mL). Figure 31 and Table 2 present the structure and the dimensions of the holder used called fluorodish.

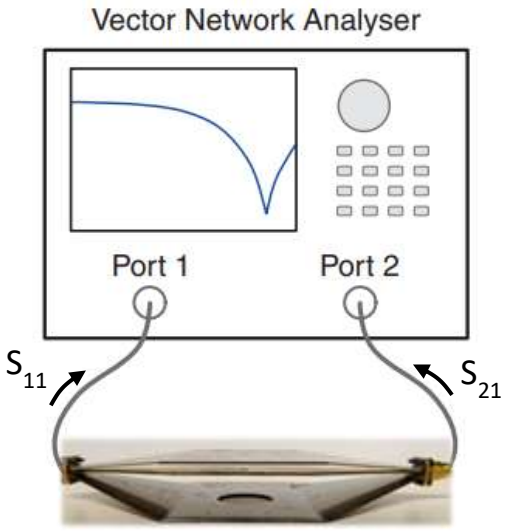


Figure 30 : Experimental setup for the frequency characterization of the TEM cell exposure system.

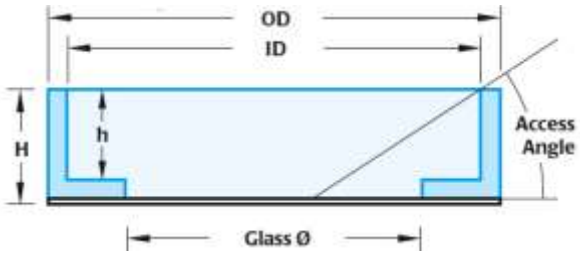


Figure 31 : Schematics and dimensions of the Fluorodish.

| OD | ID | H | h | Glass Ø | Glass thickness | Access Angle |
|---|---|---|---|---|---|---|
| 35 mm | 33 mm | 9 mm | 7.8 mm | 23 mm | 0.17 mm | 29° |

Table 2 : Dimensions of the Fluorodish container.

Figure 32 presents the reflection and transmission coefficients measured by the VNA. The modulus of $S_{11}$ does not exceed -10 dB in our operating frequency range of [0.01 – 3] GHz which proves the good impedance match of the TEM cell. The modulus of transmission coefficient varies between 0 and -1 dB meaning that a minimum of 80 % of the incident energy was transferred within the TEM cell. The frequency response of the TEM cell with the fluorodish shows that the insertion of the sample holder inside the exposure device did not significantly disturb the results.

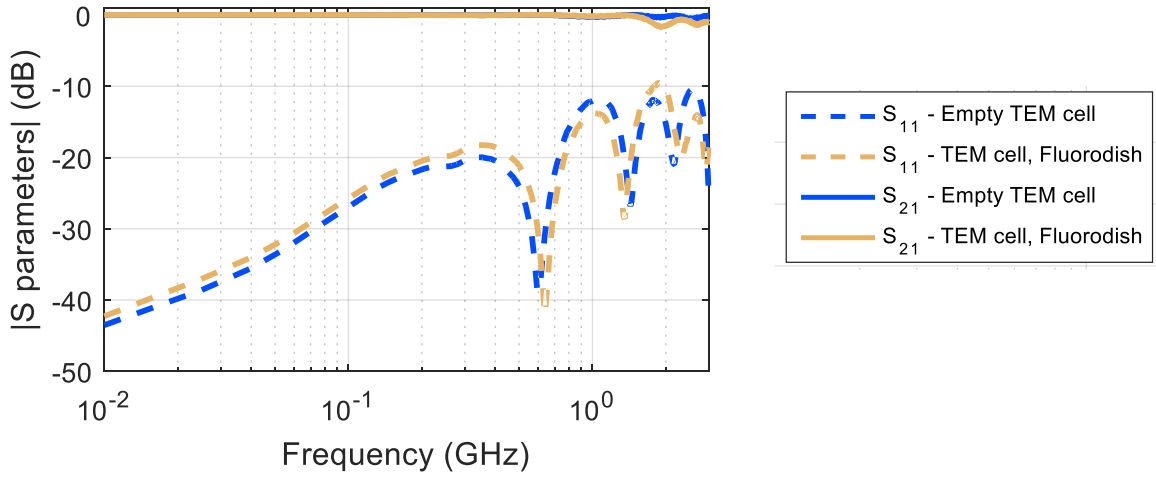


Figure 32 : Modulus of S parameters ($S_{11}$ and $S_{21}$) of TEM cell with a 20 mm aperture, empty and with fluorodish containing 3 ml of culture medium.

### II.2.5.2. TEM cell numerical modeling

The TEM cell design was numerically modeled using CST MWS software based on the dimensions illustrated in Figure 29. All metallic parts were set as a Perfect Electric Conductor (PEC). Meshing was non-uniform and the smallest meshes were set at the coaxial input and output connectors as presented in Figure 33 with a 0.16 mm × 0.17 mm surface grid and a 0.16 mm for the connector length. E-field within the TEM cell was computed numerically at 1.8 GHz and results represent the E-field component ($E_n$) normal to the TEM cell plates as the other components are negligible. Results displayed in Figure 34 represent the spatial distribution of the maximum amplitude of $E_n$ component. The longitudinal plane cut shows the E-field intensity variation at the direction of propagation at the center of the device. The field propagating at the upper section of the device presents higher levels due to the reduced separating distance (8 mm) compared to the field at the lower section (12 mm). Using an excitation signal of 1 W average power, the field varied at the exposure area between 658 and 913 V/m which is comparable to the theoretical value of 830 V/m computed with equation ( 6).

$$E = \frac{\sqrt{2P \times Z}}{h} \quad \text{(V/m)} \qquad (6)$$

a)

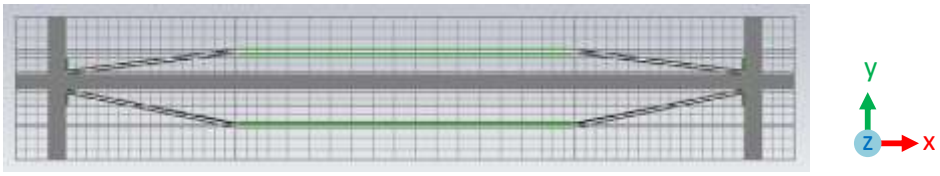


b)

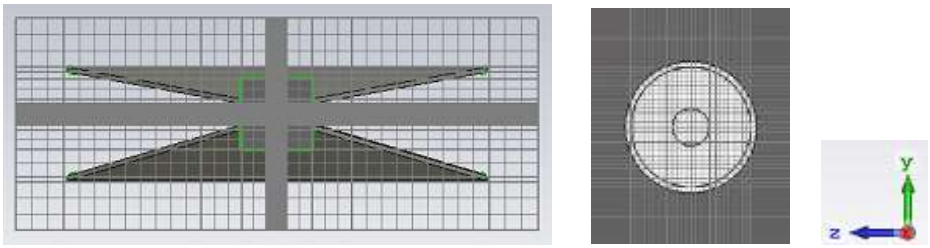


Figure 33 : Schematics of the non-uniform meshing of the TEM cell.

Where P the incident power amplitude in W, Z the characteristic impedance of the device in Ω and h the distance separating the two plates in mm. The theoretical E-field value was found by using a 50 Ω impedance, a 1W average power and a 12 mm distance.

Biological samples are generally placed between the septum and the lower plate of the TEM cell and in the center where the E-field is homogenous. The variation observed (Figure 34a) at the center of the TEM cell between the plates represents a standing wave caused by the reflections induced by the tapers and the connectors. The uniformity of the E-field is observed in the transversal plane cut, the field is confined between the plates and does not propagate outside the structure, thus, limiting the coupling with external equipment.

The 20 mm diameter aperture that was built at the bottom plate of the TEM cell for microscopic recording, slightly changed the E-field within the area of interest as presented in Figure 35Figure 35. The aperture lowers the intensity of the field between the septum and the lower plate along the vertical axis. Outside this area, the E-field was not disturbed and maintained the same intensity as in the configuration without aperture.

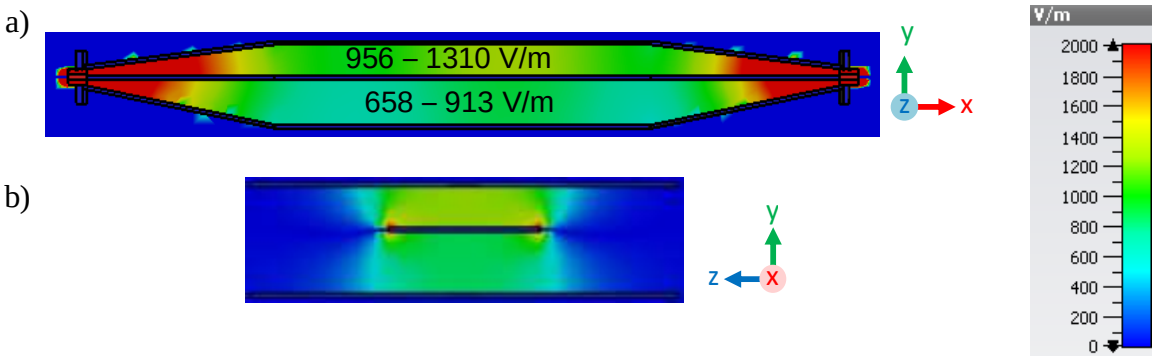


Figure 34 : E-field distribution in the open TEM cell at 1.8 GHz, a) longitudinal and b) transversal plane cuts.

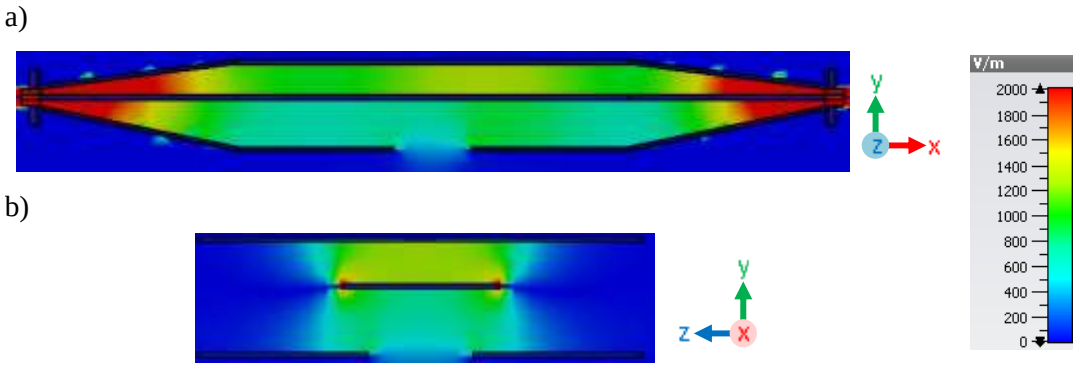


Figure 35 : E-field distribution in open TEM cell at 1.8 GHz with 20 mm diameter aperture, a) longitudinal and b) transversal plane cuts.

The model of the sample holder (i.e. fluorodish) used in experiments was added as shown in Figure 31. The fluorodish is mainly made with a loss-free dielectric material i.e. plastic that was modeled with a relative permittivity of 2.5 and a volume density of 1050 kg/m$^3$. The bottom of the dish is a 0.17 mm glass layer. The electric properties used for the glass were a relative permittivity of 7.5 and a density of 2500 kg/m$^3$. The biological solution often used in our experiments is either HEPES buffered salt solution (HBSS) or Dulbecco's modified eagle medium (DMEM) culture medium. HBSS and DMEM culture media have similar dielectric properties at room temperature and at 1.8 GHz which are $\varepsilon_r = 74.2$, $\sigma = 2.3$ S/m and $\rho = 1000$ kg/m$^3$. The amount used usually with the fluorodish is 3 mL. Thus, the biological medium in Figure 36 was designed with a meniscus and a total height of 5.25 mm corresponding to the 3 mL used in experiments. The numerical design of the medium is uniformly meshed with a 0.1 × 0.1 × 0.1 mm spatial grid as shown in Figure 36. The TEM cell meshing was as described at the beginning of this section.

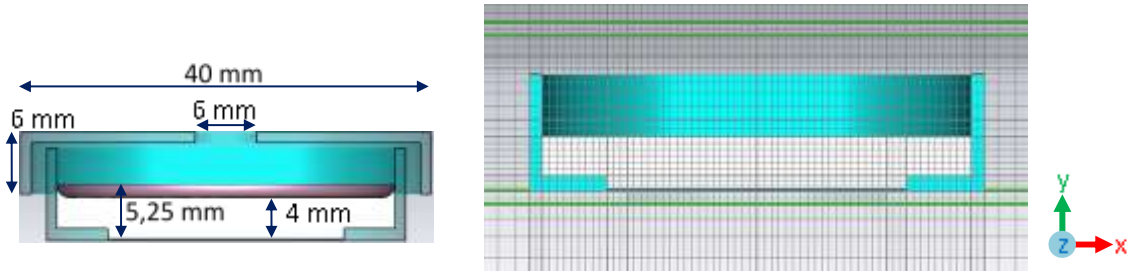


Figure 36 : Dimensions and meshing of the numerical design of the fluorodish with 3 mL of culture medium.

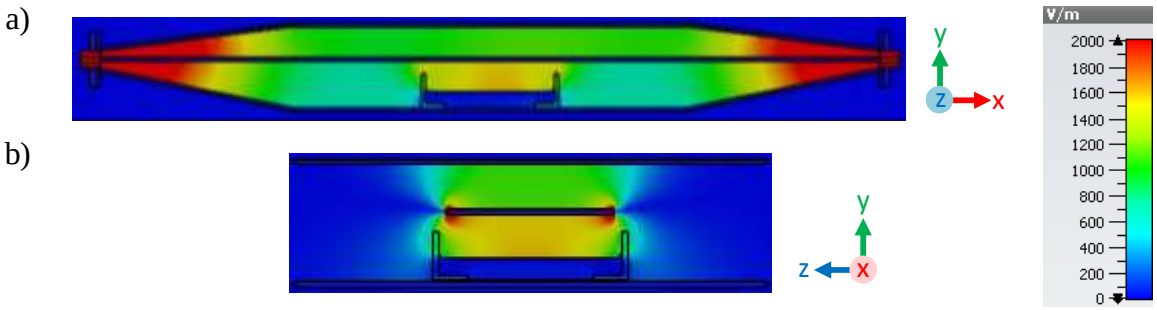


Figure 37 : E-field distribution at 1.8 GHz of the TEM cell containing Fluorodish filled with 3 mL of HBSS, a) longitudinal and b) transversal plane cuts.

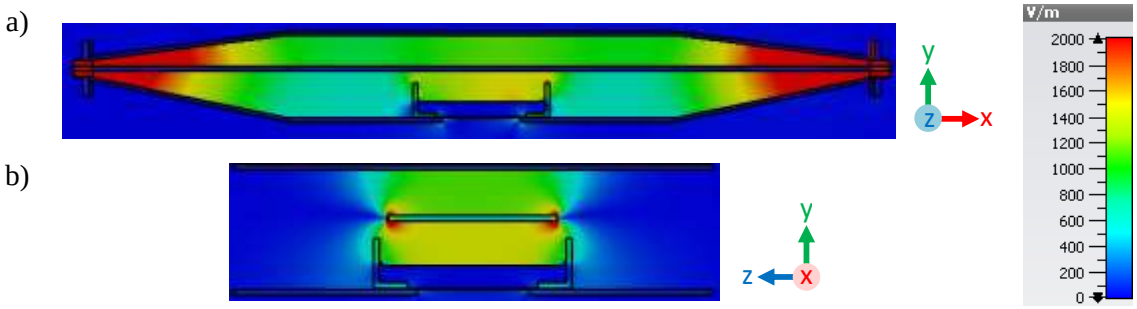


Figure 38 : E-field distribution at 1.8 GHz of the TEM cell with 20 mm diameter aperture containing Fluorodish filled with 3 mL of HBSS, a) longitudinal and b) transversal plane cuts.

Figure 37 and Figure 38 display the numerical spatial distribution of the E-field obtained at 1.8 GHz for a TEM cell containing a fluorodish filled with 3 mL of HBSS. Two configurations were simulated with no aperture and with a 20 mm aperture, respectively. In both cases, the field remains confined between the septum and the surface of the medium.

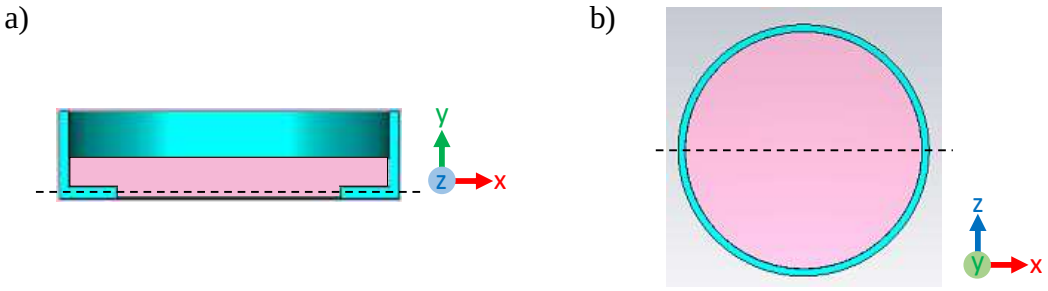


Figure 39 : Cut planes used for displaying the SAR distributions. a) horizontal cut plane at 100 µm above the bottom of the culture medium, b) vertical cut plane at the center of the medium.

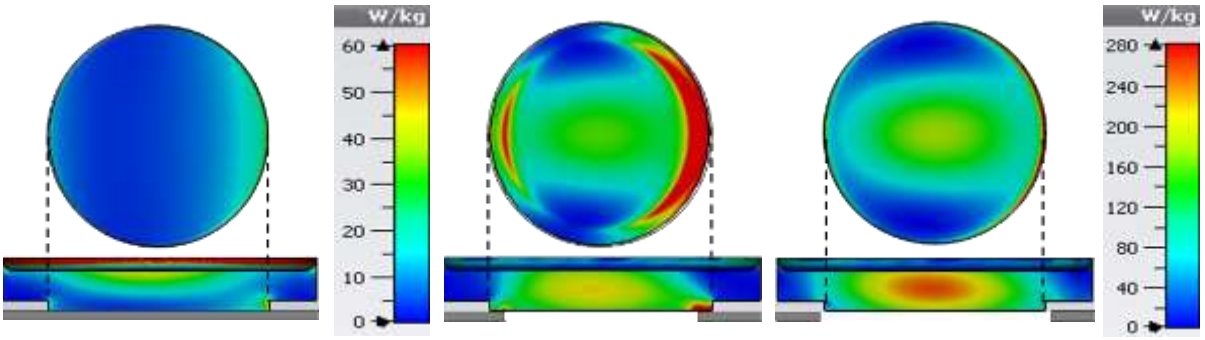


Figure 40 : SAR distribution at 1.8 GHz of 3 ml culture medium within the Fluorodish, horizontal cut at 0.1 mm above the bottom and a vertical cut at the center, a) no aperture in the bottom plate of the TEM cell, b) 20 mm diameter aperture, c) 24 mm diameter aperture.

To investigate the E-field coupling with the biological solution, SAR distribution was calculated. Figure 40 displays the SAR distribution of the 3 ml culture medium within the fluorodish at 1.8 GHz. The SAR is presented according to the plane cuts of Figure 39 i.e. an horizontal cut at 0.1 mm above the bottom of the medium and a vertical cut at the center of the culture medium. Displayed SARs are obtained for a TEM cell with no aperture, with a 20 mm aperture and 24 mm aperture.

Overall, the SAR distribution differs from one case to the other in terms of SAR levels showing the impact of the aperture and its size on the E-field coupling. In Figure 40a, the SAR reveals good homogeneity in the horizontal cut with the lowest SAR bottom efficiency of 7.84 W/kg as presented in Table 3. This latter summarizes all SAR types calculated for the 3 cases and normalized per 1 W. The SAR bottom is calculated at the bottom layer with 0.1 mm thickness. The vertical SAR cut displays a gradual increase of the dose absorbed observed along the medium height. This variation can be considered negligible compared to that of the two

other results where the inhomogeneity increases considerably. The aperture remarkably increases the absorbed energy especially at the center of the sample. SAR values gradually lower while moving toward the fluorodish peripherals. The 20 mm aperture induced a significant coupling at the peripheries of the bottom layer of the medium which is noticeable from the horizontal cut and that explains the high SAR bottom value of 127.45 W/kg. The third design with the 24 mm aperture leads to a significant increase in the middle of the medium which is remarkable in the vertical cut and it resulted in a high SAR probe efficiency of 211.8 W/kg and a standard deviation of 8.6 W/kg.

| | No aperture | 20 mm aperture | 24 mm aperture |
|---|---|---|---|
| SAR volume (W/kg) | 12.25 | 54.73 | 70.53 |
| SAR bottom (W/kg) | 7.84 | 127.45 | 95.90 |
| SAR probe (W/kg) | 6.50 ± 0.62 | 184.80 ± 6.80 | 211.80 ± 8.60 |

Table 3 : Numerical SAR efficiencies normalized per 1 W incident power.

This section discussed the E-field homogeneity within the TEM cell and the influence of the aperture on the SAR values. In the following section, the TEM cell with 20 mm aperture will be used for Rhod-B evaluation.

## II.2.6. Macrodosimetry for Rhodamine B calibration

Rhod-B was previously used in several studies to detect the microscopic cell biological changes occurring during RF exposures [164], [165]. The sample under test was marked with the fluorescent dye. Calibrating the dye is crucial and it consists in determining the fluorescence intensity levels corresponding to different levels of temperature allowing to define a calibration curve. Our objective is to characterize the Rhod-B by evaluating its sensitivity towards different exposure parameters. Varying the experimental setup parameters allows to define the dye limitations, avoid erroneous results and improve the accuracy.

The investigation and the calibration of Rhod-B were performed at the macroscopic scale through a simple measuring method. The fluorodish was filled with culture medium

labeled with Rhod-B and inserted in the RF exposure device (i.e. open TEM cell) between the septum and lower plate. The TEM cell was placed on the microscope stage within the exposure setup as presented previously. During the exposure of the solution to the RF signal, temperature increase was detected with the Luxtron thermometer and Rhod-B fluorescence was recorded by the microscope camera. Both outcomes were compared and superposed leading us to develop a relation between temperature and fluorescence. This procedure was performed with a simple millimeter culture holder (i.e. Fluorodish) because the E-field within the sample is more homogenous in this configuration i.e. on a small sarea above the microscope objective and induces quite predictable temperature values without local high gradient variations. Thus, results from the millimeter (temperature) and micrometer (Fluorescence) scales can be compared.

#### II.2.6.1. Choice of exposure parameters

As the frequency of the RF signal used for all the experiments conducted was fixed at 1.8 GHz, other parameters were studied to determine the impact of their variation on the response of this dye such as the concentration of Rhod-B in the biological sample, the RF signal incident power at the TEM cell input and the RF exposure duration. These measurements were intended to determine the limits of Rhod-B in terms of resolution and accuracy. The TEM cell with a 20 mm diameter aperture was used and set on the microscope stage because it allows the microscopic recordings as the 20x objective has a diameter of 20 mm. In addition, as shown in the previous sub-section this aperture size induces lower SAR values in the medium center compared to the 24 mm aperture.

The first tests were performed while varying the concentration of Rhod-B within the HBSS solution. HBSS is composed of inorganic salts and glucose to maintain cells alive. The Rhod-B concentration values used were 50 µM, 10 µM, 1 µM, 0.1 µM and 0.01 µM. These concentrations were selected based on the literature, research and previous experiments [164]–[166]. The Luxtron probe was inserted inside the TEM cell and into the solution through the openings made at the top plate and the septum. The probe was positioned, as much as possible with an unaided eye at the bottom of the dish and in the center, hence, it was approximate and can cause some uncertainties. Images were recorded with a sampling rate of 1 sample every 5 seconds. The Rhod-B exciting light was generated from the microscope with 2.5 % intensity

**10 W input power**

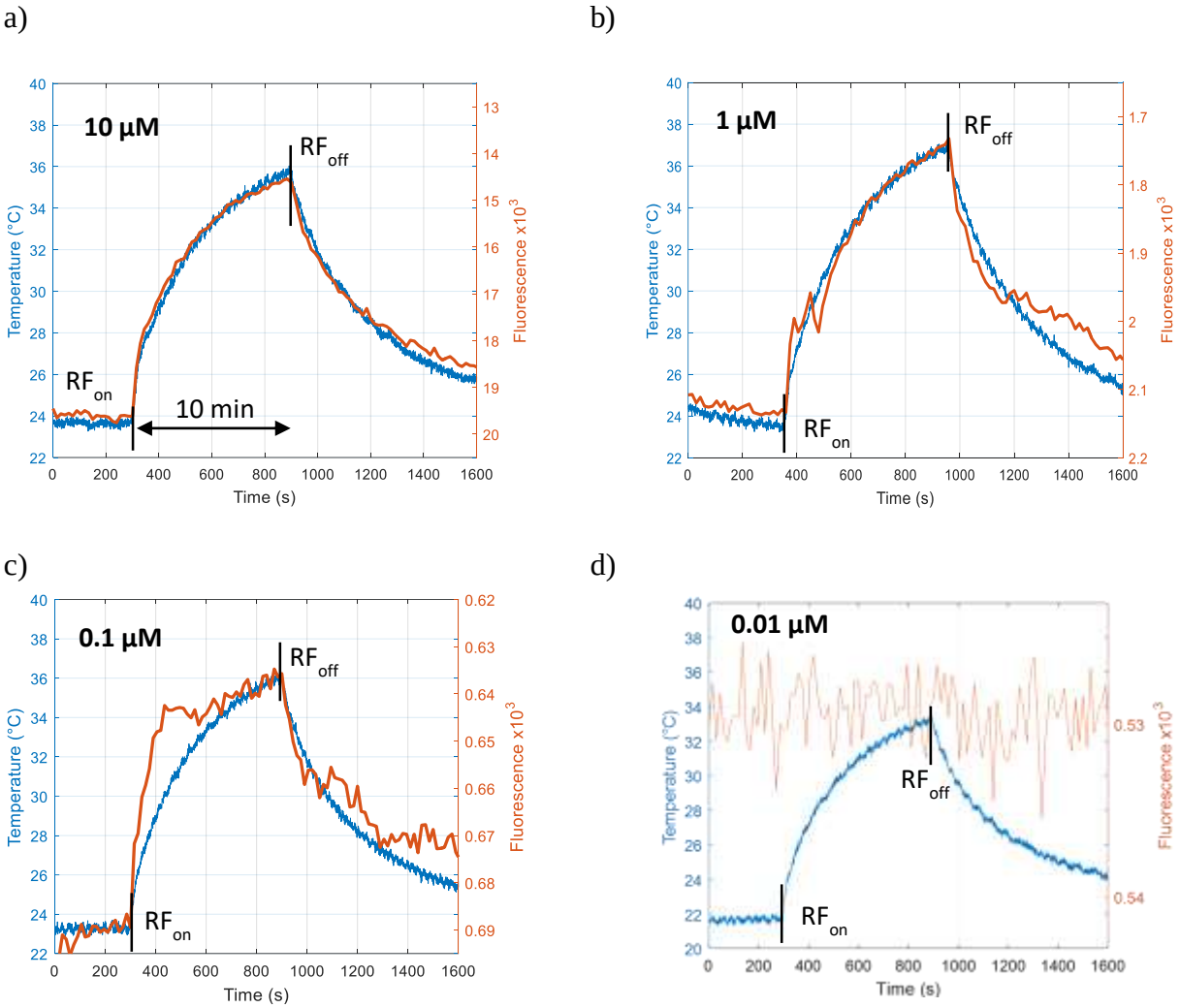


Figure 41 : Variation of Fluorescence intensity and temperature within 3 ml of HBSS labeled with Rhod-B for different concentrations exposed to 10 W power during 10 minutes, a) 10 µM, b) 1 µM, c) 0.1 µM, d) 0.01 µM.

and for a duration of 1 ms with the same sampling rate mentioned. The selected microscope parameters just mentioned are fixed for the rest of this section unless other values are specified.

The generated signal transmitted to the input port of TEM cell was applied with 10 W incident power for 10 minutes long to obtain a significant temperature elevation with sufficient time to evaluate the fluorescence variation. Curves in Figure 41 present the experimental results that consist of the fluorescence and temperature changes recorded within the labeled biological sample for the concentrations of 10 µM, 1 µM, 0.1 µM and 0.01 µM.

The fluorescence intensity of the Rhod-B dye is reversely proportional to the temperature. Thus, to superpose the temperature and the fluorescence curves, the fluorescence axis was reversed. Then, the fluorescence curve is shifted vertically and horizontally until both curves overlay. As a result, the temperature and fluorescence curves have the same initial reference levels, elevation and starting time.

It can be noticed from these plots that a great match between the fluorescence intensity and the temperature curves was obtained with 10 µM concentration. As the concentration lowers, the accuracy of fluorescence intensity decreases and dissimilarities between the two curves begin to appear. At 0.1 µM, fluorescence intensity shows noticeable differences which makes the results unexploitable for SAR retrieval (SAR is determined at the start of the temperature rise). Below 0.1 µM concentration, the Rhod-B fluorescence was undetectable. As a result, based on this exposure configuration and excitation parameters selected, the minimum concentration recommended for reliable results and proper calibration is 10 µM.

The impact of incident power on the response of the Rhod-B was then evaluated. It is important to evaluate the sensitivity of the dye for low RF power to evaluate the technique limitations. Since the minimum concentration recommended is 10 µM, the HBSS medium labeled with Rhod-B was prepared with 50 µM concentration. The power levels used were 10 W, 5 W, 1 W and 0.5 W and in each experiment, one of these values was applied for 10 minutes. Between the measurements, the medium within the fluorodish was replaced with a new non-exposed amount (i.e. 3 mL). It is observed in Figure 42 that the curves of fluorescence measured with the 20x microscope objective have a great match with temperature results measured with the Luxtron thermometer and this remains valid even for low power levels such as 0.5 W. A maximum increase of 16 °C, 8 °C, 3 °C and 1.5 °C were detected for respectively 10 W, 5 W, 1 W to 0.5 W.

**50 µM concentration**

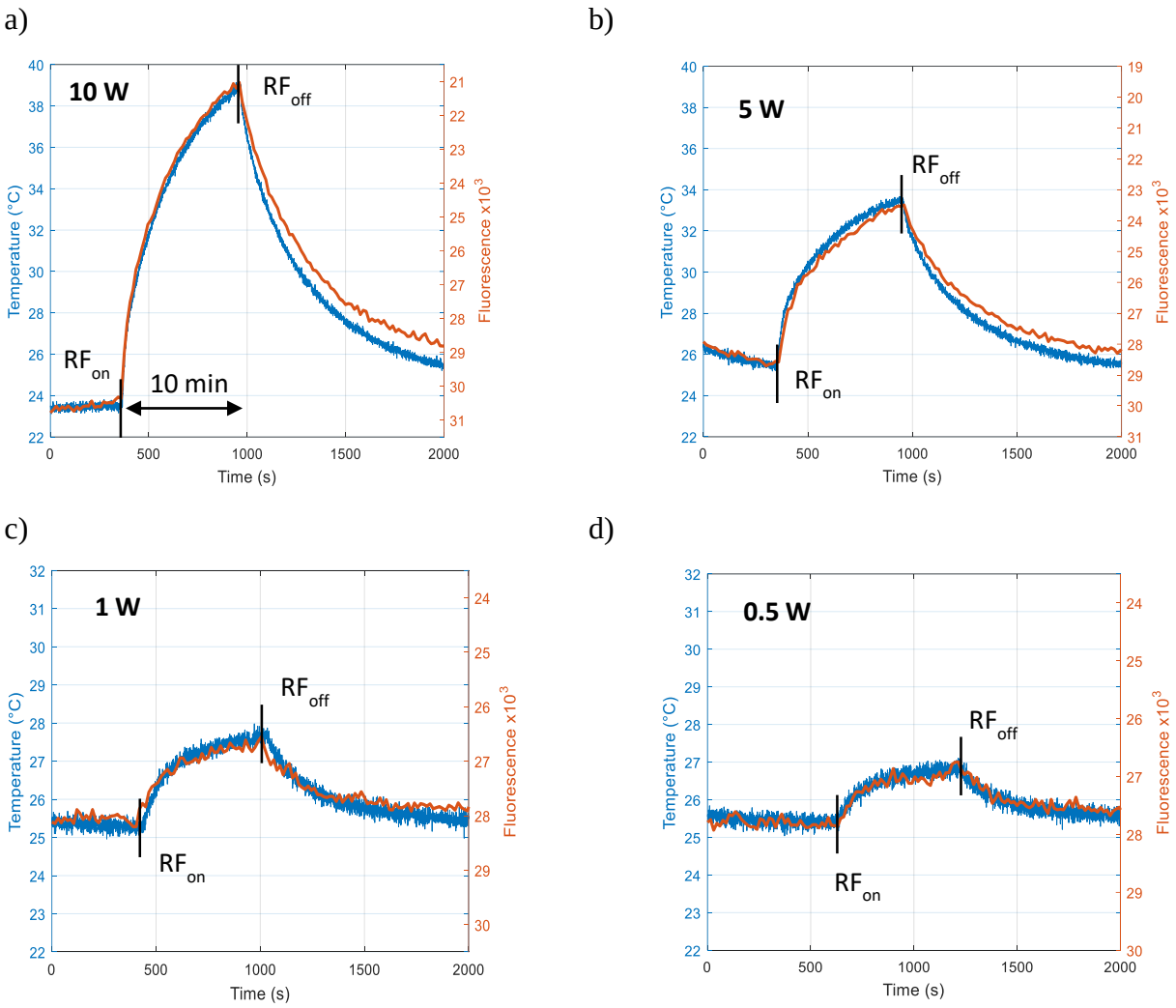


Figure 42 : Variation of Fluorescence and temperature within 3ml of HBSS labeled with Rhod-B with 50 µM concentration exposed to different incident power for 10 minutes, a) 10 W, b) 5 W, c) 1 W, d) 0.5 W.

Since the 50 µM concentration was sufficient for thermal detection of few Celsius degrees, several tests were also conducted with a concentration of 10 µM. The exposure duration was set for 1 minute and the recording sampling was increased to 1 image/s. Figure 43 shows the changes in temperature and fluorescence detected by the thermometer and the microscope camera for an input power of 10 W, 5 W, 1 W and 0.5 W. Curves resulted from the application of 10 W have a good match between the start and the end of exposure which means that the fluorescence outcome can be exploited for SAR extraction. However, for lower power levels

**10 µM concentration**

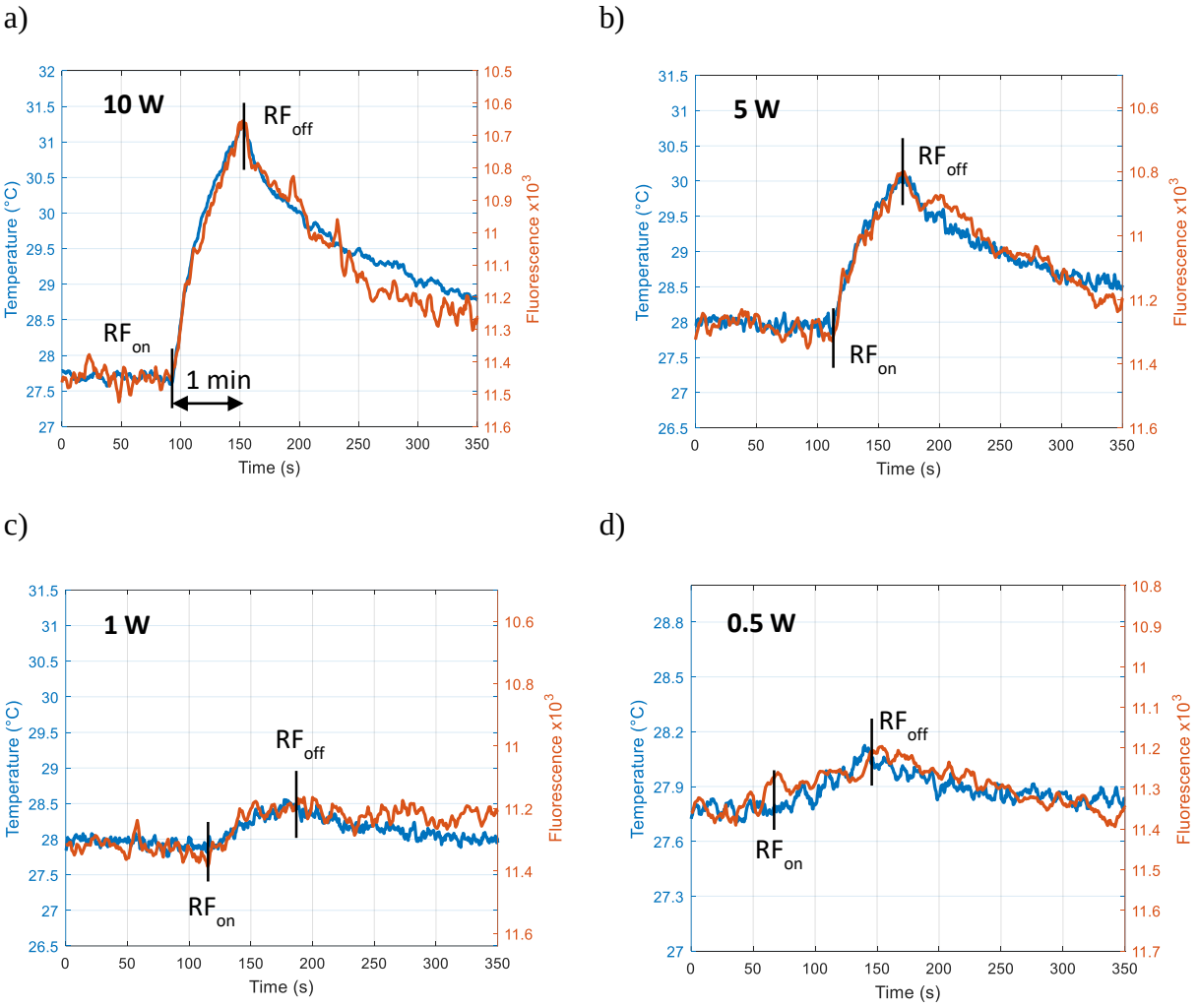


Figure 43 : Fluorescence and temperature change within 3 ml of HBSS labeled with Rhod-B (10 µM concentration) exposed to different incident power for 1 minute, a) 10 W, b) 5 W, c) 1 W, d) 0.5 W.

and even with a high sampling rate, Rhod-B fluorescence intensity measured hardly followed the heat change, thus, results are not reliable for SAR retrieval.

To conclude, mediums with low Rhod-B concentrations such as 10 µM can be used for high power exposure above 10 W. For low power level applications, a minimal concentration of 50 µM is required to guaranty the reliability and the reproducibility of fluorescence results. For the following assessments conducted with the Rhod-B dye, the 50 µM concentration was used.

**50 µM concentration, 10W power**

a) b)

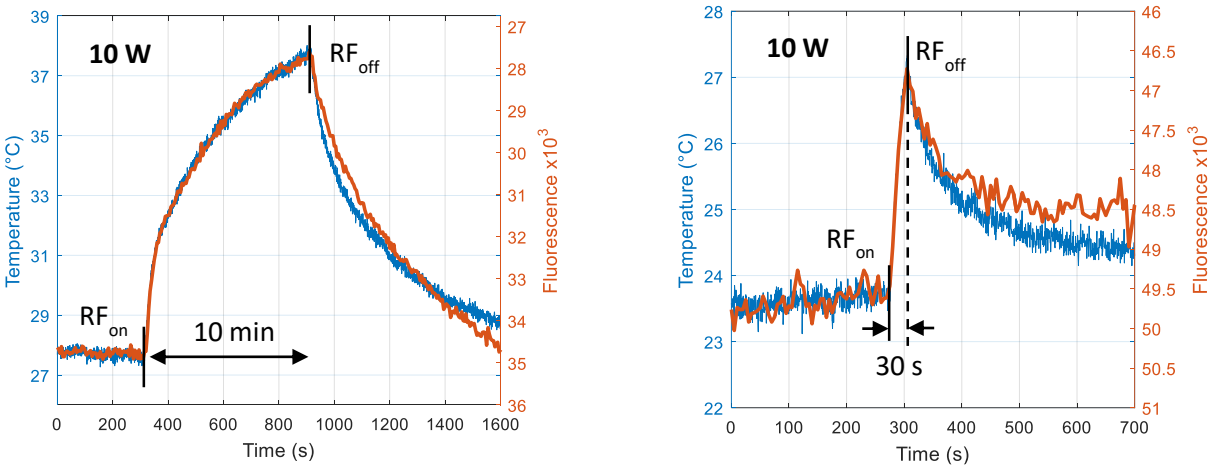


Figure 44 : Variation of temperature and Rhod-B Fluorescence of 3 ml of HBSS and Rhod-B (50 µM concentration) exposed to 10 W power for two different exposure durations, a) 10 minutes exposure, b) 30 seconds exposure.

The next parameter evaluated was the exposure duration. RF signal application was performed for two durations that were 10 minutes and 30 seconds. The power intensity level was set at 10 W. Temperature variation and Rhod-B fluorescence intensity curves of Figure 44 display the recordings obtained with both durations. Within the time range of interest which starts at RF-on and ends at RF-off, results show a good fit even for short time exposure conditions. This means that exposure duration has no particular limitation over the fluorescent dye at least down to 30 seconds exposure duration.

The sampling rate used for microscope configuration is also important. It corresponds to the emission frequency by the light engine toward the medium for dye excitation and it also corresponds to the number of images per second recorded by the microscope camera. An excessive sampling rate can cause the photobleaching of the dye, therefore, resulting erroneous fluorescence intensity results. In this context, two values of the sampling rate were exploited, which were 1 record/5s and 1 record/1s. The RF signal was applied for 30 seconds with an input power of 10 W. Changes in fluorescence and temperature are plotted in Figure 45. In the range where temperature rises, both sampling methods induce great match between curves even when the sample medium was exposed for short durations (i.e. 30 seconds). Some dissimilarities appear toward the end of exposure due to the lack of sampling points in Figure 45a. It is recommended to ensure that measurements are conducted with sufficient sampling especially

**50 µM concentration, 10 W power for 30 s**

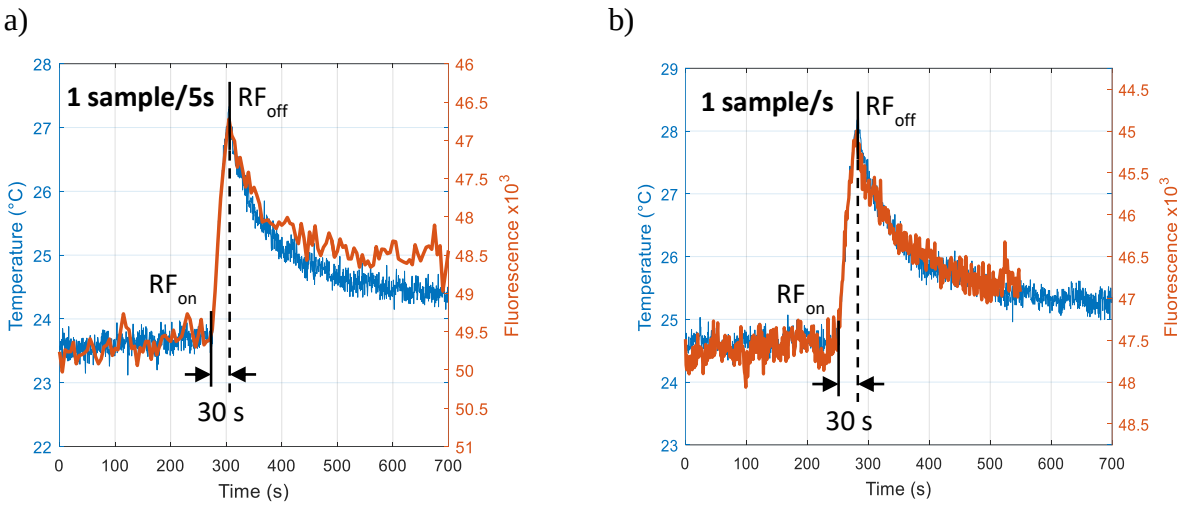


Figure 45 : Fluorescence intensity and temperature variations recorded within 3 ml of HBSS labeled with Rhod-B (50 µM concentration) exposed to 10 W for 30 s with different microscopic sampling rate, a) Fluorescence measured with 1 sample/5s, b) Fluorescence measured with 1 sample/s.

when characterizing microsystems as they require more precise evaluations. Hence, a 1 record/s sampling rate was selected for the rest of the microscopic experiments.

These investigations allowed the optimization of Rhod-B usage and the recording of its fluorescence intensity. With the adequate configuration, the calibration of the fluorescence can be achieved by establishing a relation between its intensity and the temperature variation.

The experiments conducted to evaluate the fluorescence of Rhod-B are rather complex since several parameters of the measurement setup related to 1) the biological medium preparation, 2) the RF exposure system, and 3) the imaging fluorescence recordings require to be adjusted and optimized simultaneously. Despite the tuning, some uncertainties still exist that can slightly affect the outcomes. The temperature fiber optic probe position within the biological medium was approximate and the use of air-conditioning to control the room temperature can cause ± 1°C variation on room temperature which may lead to the variation of the dielectric properties of used culture medium. Moreover, the position of the fluorodish within the TEM cell was also approximate since it needs to be taken out after each experiment to renew the medium.

The experiments conducted showed that to guarantee good accuracy and reproducibility, it is important to properly select the parameters values. First, Rhod-B fluorescence intensity depends on its concentration and it was concluded that the minimum Rhod-B concentration recommended for reliable results is 10 µM. However, this concentration can be used only when applying high power levels ( > 10 W) to obtain an accurate SAR value. Fluorescence intensity recorded while using 50 µM concentration showed a great match with temperature results measured with the Luxtron thermometer. The accuracy remained valid even for low power levels such as 0.5 W.

Fluorescence intensity is independent of the incident electric power levels and measurements proved that exposure duration has no particular limitation over the fluorescence even for short 30 seconds exposure durations. Choosing an adequate sampling rate is essential as well for better precision.

### II.2.7. Influence of the microscope working distance

The distance between the bottom of the fluorodish and the microscope objective is important as it can impact the SAR value. Hence, numerical investigations were conducted with home-made software based on the Finite Difference Time Domain (FDTD) method. The top part of the objective was modeled with the TEM cell, the fluorodish and the biological sample. The SAR spatial distribution illustrated in Figure 46 is obtained by setting the microscope at a working distance of 200 µm. This distance corresponds to the gap between the bottom of the fluorodish and the top of the objective. The inset schematizes the volume used to compute the SAR probe, it corresponds to the measurement volume of the Luxtron probe. Using the FDTD method, this volume is defined as a cylinder of 1 mm in height and 1 mm in diameter.

The curves plotted in Figure 47 represent the variation of SAR depending on the working distance. The gap variation affected mostly the bottom layer of the biological medium resulting in changes of the SAR bottom and SAR probe. The position of the microscope objective must be considered as SAR values considerably increase with the remoteness of the objective. For example, at a 500 µm distance, the SAR probe and the bottom SAR values are about 80 and 100 W/kg, respectively. When the objective is close to the fluorodish it almost seals the TEM cell aperture and approaches the closed TEM cell configuration.

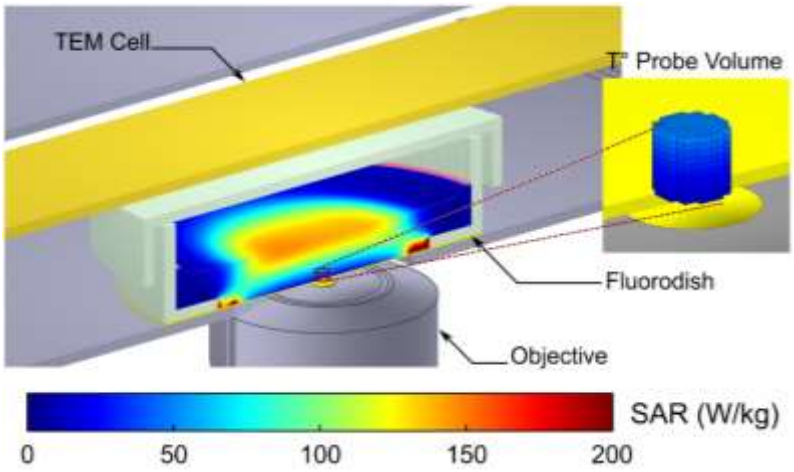


Figure 46 : Transversal cut of the numerical SAR spatial distribution at the center of the biological medium inside the fluorodish in the TEM cell. SAR values at 1.8 GHz, normalized per 1 W incident power while the objective is distant by 200 µm from the fluorodish bottom [167].

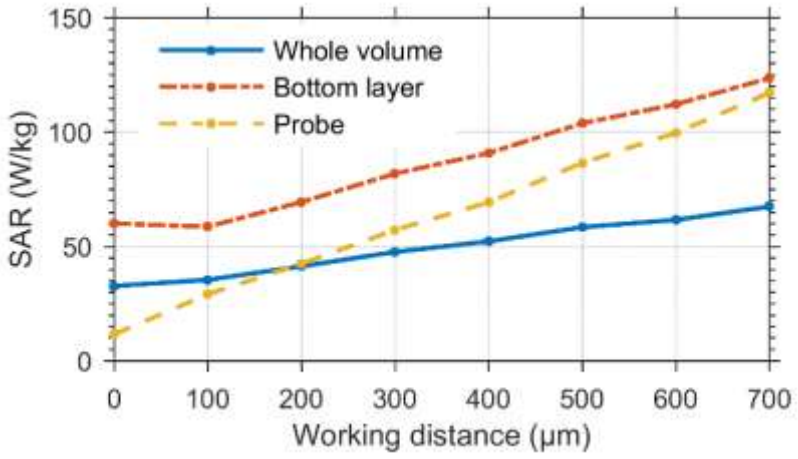


Figure 47 : SAR variation along the distance between the bottom of the fluorodish and the microscope objective [167].

## II.2.8. Temperature extraction from fluorescence intensity results

Rhod-B temperature dependence was extensively studied. In some reviews, fluorescence shows a linear variation to temperature [156], [168]. However, Ross et al. [166], Fu et al. [169], and Samy et al. [170] fitted the fluorescence calibration curve by a third-order polynomial equation presented below.

$$T = A_0 + A_1 I + A_2 I^2 + A_3 I^3 \qquad (7)$$

where $T$ the temperature of the medium in °C, $I$ the fluorescence intensity normalized by its initial value measured at room temperature and $A_{0\text{-}3}$ are the coefficients in °C of the fitting equation. The coefficients of each of these three papers are classified in Table 4. The coefficient $A_0$ of the three papers are not significantly different. However, dissimilarities are observed with the $A_1$, $A_2$ and $A_3$ coefficients where those of Fu et al. are higher and those of Ross et al. and Samy et al. are quite similar. The equation parameters can vary from one paper to the other due to the difference in their measurement configurations. For example, the setup of Samy et al. is different and based on a temperature measuring chip which may lead to the difference in its calibration curve compared to the other ones as presented in Figure 48. The calibration curves of the three papers were compared in [161] and overall they have a similar tendency in the temperature ranging between 20 – 100°C. For low fluorescence intensity values ( < 0.8 ), temperature values extracted from each curve can be dissimilar. As the intensity tends toward 1, the values become highly similar with only a few degrees difference.

| | Ross et al. | Fu et al. | Samy et al. |
|---|---|---|---|
| $A_0$ | 132 | 149.15 | 141.53 |
| $A_1$ | -250 | -317.84 | -250.25 |
| $A_2$ | 220 | 323.41 | 228.02 |
| $A_3$ | -79 | -131.84 | -96.904 |

Table 4 : Fitting equations coefficients from three literature papers.

The typical temperature interval for our measurements is between 20 and 37 °C. Within this range, the curves tendency of Figure 48 can be considered linear. A first-degree equation was determined to allow the retrieval of temperature increase values from fluorescence intensity detected. The equation ( 8 ) is defined as the normalized fluorescence variation $\Delta Fluo/Fluo(0)$ multiplied by a coefficient named conversion coefficient α.

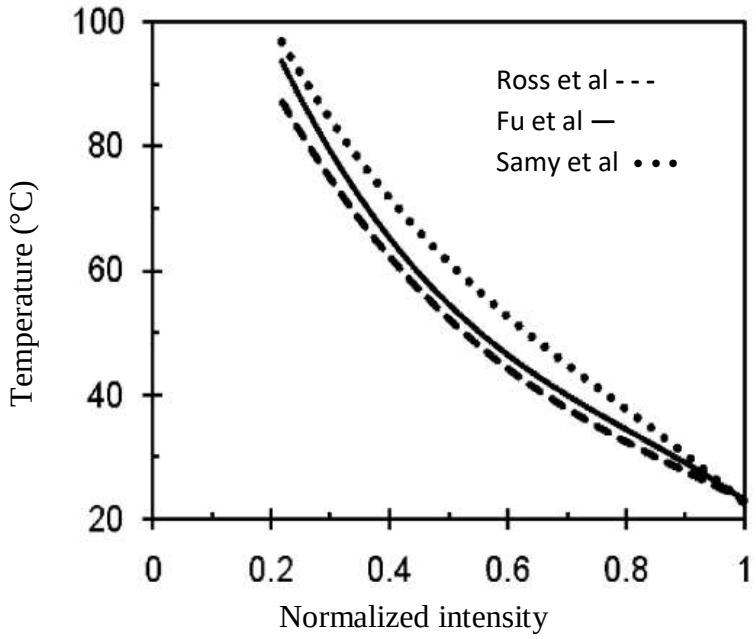


Figure 48 : Variation of the temperature as a function of the normalized fluorescence [161]. Comparison of the fitting equations of Ross et al., Fu et al. and Samy et al.

$$\Delta T = \alpha \frac{\Delta Fluo}{Fluo(0)} \qquad (8)$$

In equation ( 8 ), $Fluo(0)$ is the initial fluorescence value before exposure, $\Delta Fluo$ is the fluorescence difference between the recorded value at a certain instant and the initial value $Fluo(0)$. The conversion coefficient α was computed to be -57 with a 2.5 standard deviation. From our investigations [167], it was determined that normalized Rhod-B fluorescence intensity varies by about 2% per 1°C. Unlike the conversion method of Ross et al., Samy et al. and Fu et al. our conversion coefficient α and our conversion method are independent of the initial (or reference) temperature value.

Figure 49 shows the temperature variation extracted from the fluorescence intensity using equation ( 8 ) versus the temperature measured directly with the Luxtron probe. An RF signal was applied for 30 seconds with 10 W power inducing 3°C heat as observed in Figure 49a. Another test was also conducted by applying 0.5 W for 10 minutes causing an increase of 1.5°C (Figure 49b). The medium used was prepared with 50 µM Rhod-B concentration. Fluorescence was recorded with a rate of 1 sample/s and 1 sample/5s for the 30 s and 10 minutes exposures, respectively. The agreement observed between the probe measured temperature and

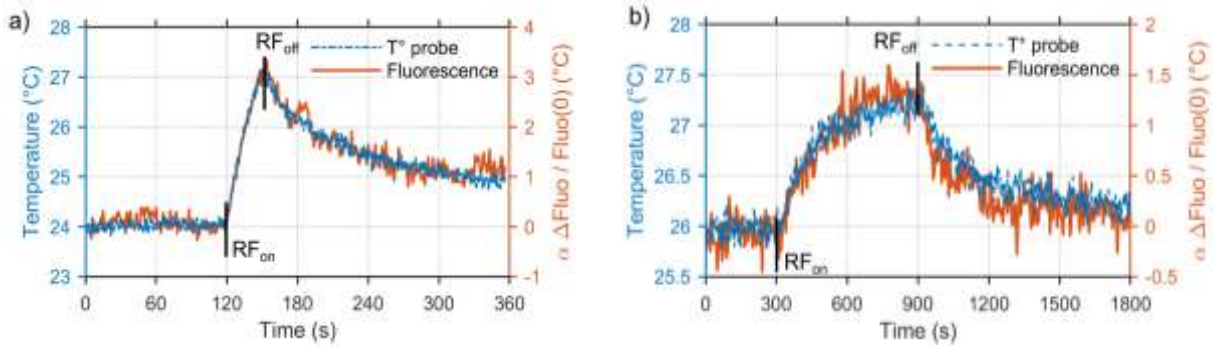


Figure 49 : Temperature change recorded by the fiber optic probe alongside the temperature increase retrieved from the fluorescence intensity measured, a) application of 10 W for 30 seconds, b) application of 0.5 W for 10 minutes.

the fluorescence retrieved temperature proves and verifies the accuracy of the conversion coefficient α.

In this case, SAR retrieved from macroscopic Luxtron probe measurements can be compared to the SAR determined with the microscopic Rhod-B technique. Although, the probe averages the temperature over 1 $mm^3$ volume and fluorescence is detected within a 570 $\mu m^2$ surface, the outcomes can be compared as the SAR is homogenous thus independent on the selected volume. SAR values normalized per 1 W incident power are presented in Table 5. The SAR efficiencies determined from Rhod-B fluorescence are called local SAR since they were extracted from microscopic surfaces. Local SAR and SAR probe values computed from the temperature measured with the Luxtron probe are comparable.

| | 10 min exposure | 30 s exposure |
|---|---|---|
| SAR probe (W/kg) | 95.5 ± 2 | 72.2 ± 4.8 |
| Local SAR (W/kg) | 98.5 ± 6.1 | 73 ± 5.9 |

Table 5 : SAR values at 1.8 GHz for 50µM Rhod-B concentration and different incident powers. SAR values are normalized per 1 W incident power.

To confirm the accuracy of the α conversion coefficient value, a comparison was conducted between the different conversion equations, which means comparing equation ( 7 ) using its different coefficients of Table 4 with the equation ( 8 ). The same data of fluorescence intensity recorded during a CW exposure were used for temperature variation extraction with

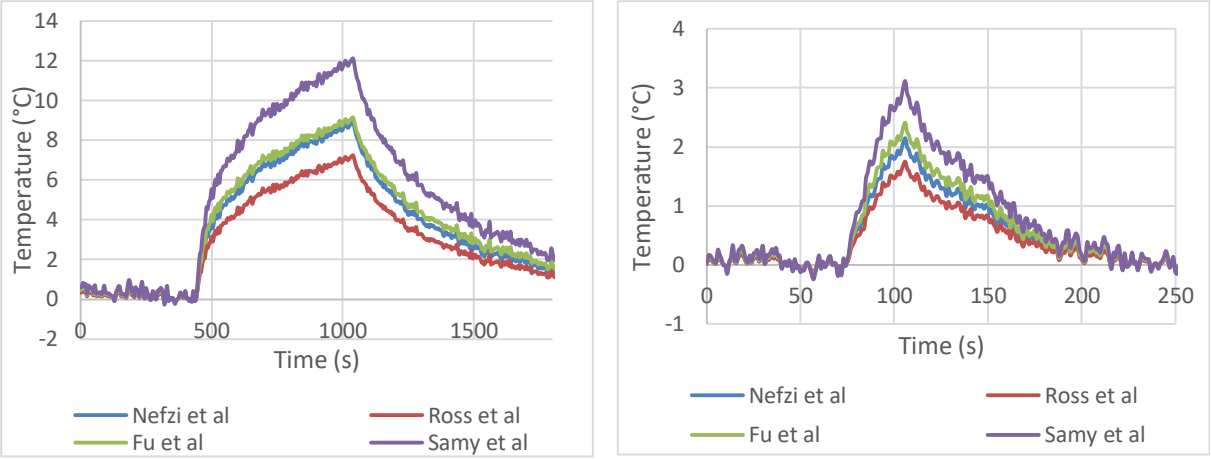


Figure 50 : Fluorescence intensity variation retrieved with 4 conversion equations.

the different equations. The power intensity of 5 W was applied for 10 minutes and 30 s exposure duration. The results presented in Figure 50 are the outcome of the conversion by our equation (i.e. Nefzi et al.) and the equations of Ross et al., Fu et al. and Samy et al. described previously. The temperature variation calculated shows great agreement between our method and the one of Fu el al. while the curve of Ross et al. is also comparable. The gap observed with Samy et al. curve can be explained by the difference in the use of Rhod-B with the exposure device. SAR efficiencies of Table 6 were determined as well for each curve. The plot of Samy et al. has the highest temperature maximum value which resulted in the highest SAR efficiency.

Local SAR (W/kg/W)

| | Ross et al. | Nefzi et al. | Fu et al. | Samy et al. |
|---|---|---|---|---|
| 10 min | 81.9 | 100.23 | 114.3 | 147 |
| 30 s | 81.5 | 90.1 | 92.6 | 118.6 |

Table 6 : SAR efficiencies in W/kg normalized per 1 W incident power determined from temperature curves of each conversion equation.

Thus, temperature can be retrieved from the fluorescence intensity through the first-degree equation defined previously. The equation and its conversion coefficient were validated by confirming their accuracy with other conversion methods. The Rhodamine B technique can now be used to evaluate the local temperature variation within microsystems.

# Conclusion

This chapter presented the macroscale characterization of the experimental setup and the methods and techniques implemented for the following microscale investigations. The size, the resolution and the accuracy limitations showed by certain measuring probes and devices do not allow the detection of the SAR or temperature within the cellular layer. Microscopy technique based on temperature-dependent dyes is an alternative with better accuracy and resolution. Based on the literature and previous studies, Rhod-B has high efficiency is strongly dependent on the temperature in aqueous solutions, has a constant quantum yield over a wide range of wavelength, its quantum yield is about 100 % at low temperature and decreases to few percentages at the boiling temperatures. A biological dye with these features is recommended for biological *in vitro* experiments.

The experimental setup described includes devices that expose the biological sample, measures the macroscale temperature, observe in real-time the biological changes and detect the local fluorescence intensity of the Rhod-B. The dosimetry of the exposure setup started by evaluating the exposure device (i.e. TEM cell). The TEM cell has various advantages and it was highly suitable for our studies. It was shown numerically that in the area of interest within the fluorodish (cellular layer) the SAR bottom is homogenous reflecting a uniform E-field exposure.

Furthermore, being part of the microscopic experimental setup, Rhod-B required a thorough evaluation. A set of experiments were conducted for its sensitivity evaluation. The sensitivity of the biological dye was conducted by investigating the influence of certain parameters (e.g.: concentration, input power, sampling rate, etc.) on its fluorescence intensity. This technique was optimized by selecting the proper settings for improved accuracy. For example, it is recommended to use a Rhod-B concentration of 50 µM as it provides accurate results even at low power intensities. For short exposure durations, the sampling rate of fluorescence intensity recording should be sufficient (exp: 1 sample/s) but not too high to cause dye bleaching. To retrieve temperature elevation from the fluorescence intensity recorded, we determined a conversion coefficient ($\alpha = -57$) that is independent of the reference temperature value. Our conversion method was validated by comparing it with other literature approaches. The reliability of this technique was then confirmed by the macroscale dosimetry based on temperature measurements with Luxtron probe.

# Chapter III.

## Macrodosimetry characterization

# Introduction

The efficiency of the Rhod-B technique was proved following the investigations conducted to calibrate and study the dye limitations. Therefore, this microscopy technique can be now used for microsystems characterization. A Microelectrode Array (MEA) is a recording device based on microelectrodes. This microsystem is designed to record electrophysiological measurements i.e. the spontaneous electrical activity of neuronal networks under RF exposures.

This chapter presents the characterization of an MEA recording microsystem at the macroscopic scale before proceeding to the microscopic scale evaluation. The study of the MEA stands within the framework of a collaboration with the IMS (Integration from Material to Systems) laboratory of Bordeaux.

The macroscopic scale assessments consist of temperature measurements within the device during the EMF application. Two MEA devices with some structural differences will be described. Their evaluation aims to study the E-field homogeneity within the sample and to reveal the impact of their structure differences on the SAR outcomes. For the EMF application, the electrophysiological devices requires to be combined with an exposure device. First, a frequency characterization will be conducted of the MEAs inserted in the TEM cell to verify the impedance adaptation and the energy transfer ratios. The numerical and experimental assessments of both MEAs in different configurations will show the influence of their dissimilarities on their response during the exposure.

# III.1. Microelectrode array (MEA)

Micro Electrode Array (MEA) devices are electrophysiological recording devices used for decades due to their ability to interact with cells through the surface microelectrodes (Figure 51). They were first introduced by Thomas et al. in 1972 as a new platform to monitor the extracellular electrical activity of cardiac myocytes [171]. The quality of the MEA devices has undergone various technological improvements to provide an efficient non-invasive platform for long term recording. The major enhancements resulted in the development of a wide range of MEAs based on planar or 3D electrodes [172], [173], CMOS, silicon and other materials for the substrates with rigid or flexible structures [174]. These characteristics are selected based on

a) b)

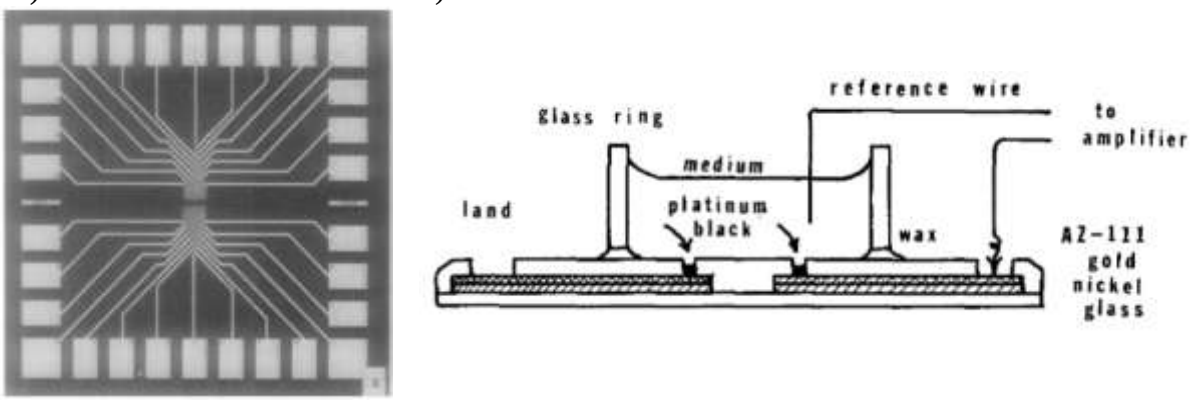


Figure 51 : The microelectrode array (MEA), a) plan view of the MEA, b) a cross-section schema of the microelectrode array [171].

the application areas of the MEA (*in vitro*, *in vivo*, implantable MEA) [175]–[178]. MEAs can also be active or passive and can operate in static or microfluidic conditions. Besides, they should be durable, reusable, biocompatible and allow real-time observation and detection.

### III.1.1. MEAs geometry

Two passive planar MEAs were evaluated. The first MEA called MEA-1 (Biosciences, Lausanne, Switzerland) depicted in Figure 52 is the upgraded version of the MEA presented in [105] that has contact pads at the top side of the PCB. The second MEA called MEA-2 (Multi-Channel Systems, Reutlingen, Germany) displayed in Figure 53 is a newer custom-designed version. An MEA is mainly composed of a culture chamber holding the biological medium, a glass chip as a substrate for electrodes, top connecting lines and a printed circuit board (PCB) (Figure 54). The electrophysiological interface has 60 microelectrodes forming an almost 8 × 8 matrix, 59 of them are used to record the neuronal response and one is used as a reference. Electrical signals are conveyed from the electrodes by thin conductor lines (Figure 52b, Figure 53b) to the output pads placed at the bottom side of the PCB and coupled to external equipment (pre-amplifier) to retrieve and analyze the signals. The microelements (electrodes, lines) are deposited on top of the glass substrate by microfabrication based on a photolithography technology. The substrate and the culture holder are then attached to the 50 × 50 mm PCB to form the culture chamber. The arrangement and the dimensions of these components vary from one MEA to the another, as detailed in Figure 54. In the case of MEA-1, the 15 × 15 mm glass is affixed to the bottom of the PCB. The reference plane is embedded within the PCB and a 10

a) b)

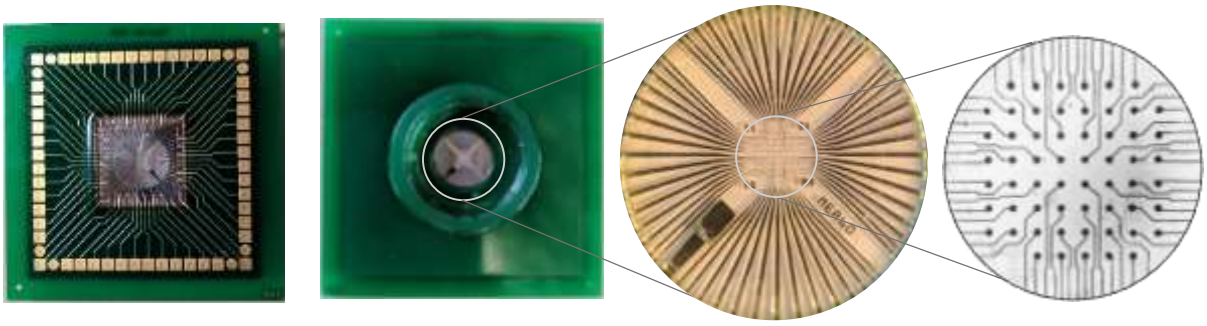

Figure 52 : Photos of MEA-1, a) bottom side view of the conductor lines and the contact pads, b) top side view including a zoom on the upper conductor lines and the electrodes.

a) b)

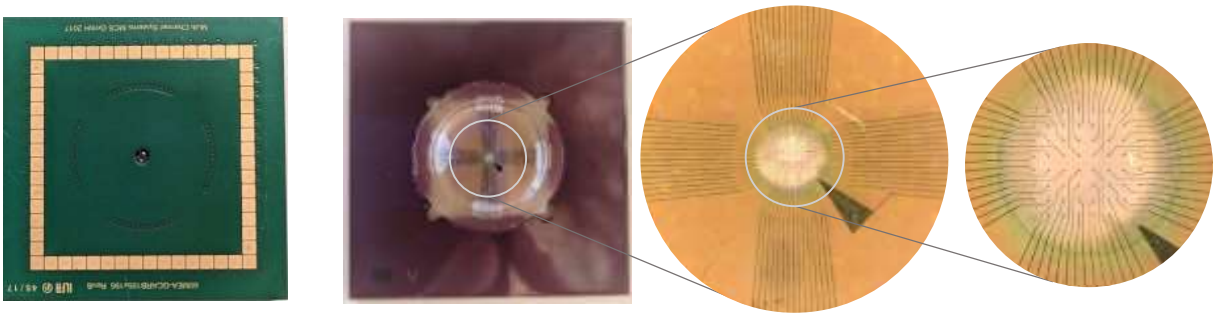

Figure 53 : Photos of MEA-2, a) bottom side view of the contact pads, b) top side view including a zoom on the upper conductor lines and the electrodes.

mm diameter cavity is made at the center for microscopic observation. Platinum is the material used for the electrodes that have 40 µm diameter tips and they are placed at 200 µm gap center to center.

Regarding MEA-2, the 24 × 24 mm glass substrate is inserted from the top within the PCB. Inside this latter, 4 reference planes are embedded, one at the level of the electrode, one at the contact pads level and two inside the PCB. The electrodes of 30 µm diameter, 60 µm height and 200 µm gap center-to-center and the lines are made of indium-tin-oxide (TiN). In this structure, lines go through the PCB and the metal plates through vias linked to the pads. The observation cavity of MEA-2 has a 2.5 mm diameter. In both devices, a layer of insulator covers the top conductor lines leaving the surface of electrodes for the adhesion of neurons terminations.

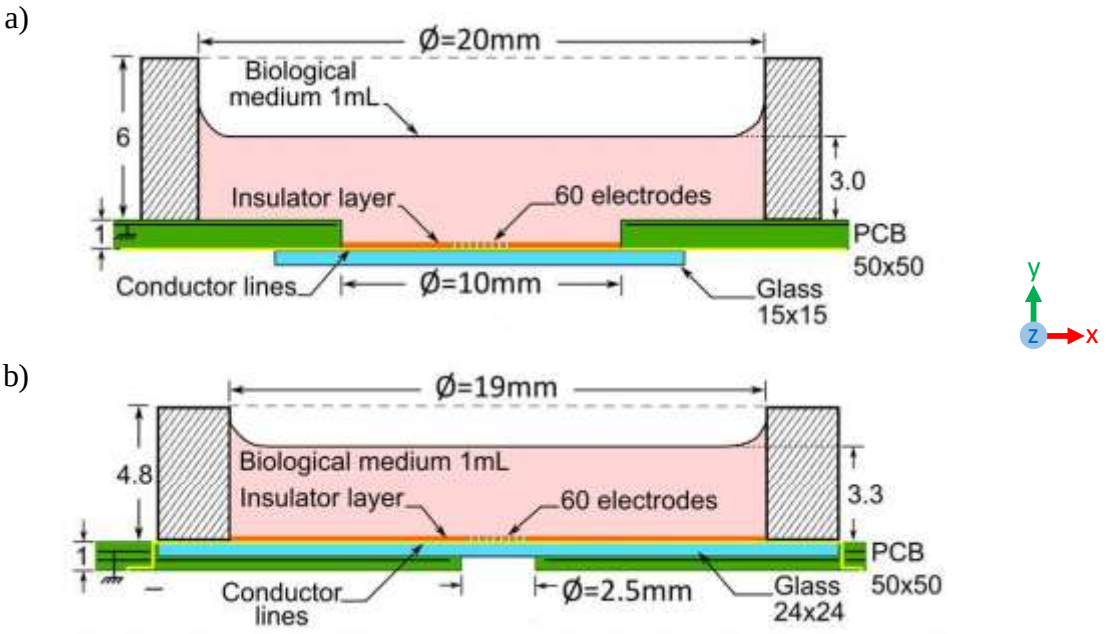


Figure 54 : 3D CAD models (transversal cut) of a) MEA-1, and b) MEA-2.

## III.1.2. Frequency characterization of the MEAs within a TEM cell

The two MEAs require an EM characterization before further detection of the neuronal electrical activity. The open TEM cell was a suitable exposure device to be combined with the MEA under test. The 20 mm aperture of the TEM cell was enlarged to be 24 mm diameter to fit the MEA culture holder. Reflection ($S_{11}$) and transmission coefficients ($S_{21}$) of Figure 55 were recorded with a VNA when the TEM cell was empty or when MEA-1/MEA-2 were inserted. The insertion of the recording devices does not significantly disturb the RF signal propagating as the curves seem to be quite similar and the reflection is under -10 dB for the entire operating frequency band confirming the good impedance match. The transmission is between 0 and -1 dB. At 1.8 GHz, $S_{21}$ is around - 0.4 dB indicating that at least 90 % of the incident energy is transmitted through the TEM cell.

S-parameters were calculated as well by simulating the empty TEM cell, the TEM cell with MEA-1/MEA-2. The results of $S_{11}$ and $S_{21}$ are displayed in Figure 56 and they are consistent with the measurements. Similarly to the measurements, the reflection is below -10 dB and the transmission $S_{21}$ values are between 0 and -1 dB. At 1.8 GHz the transmission is around -0.3 and -0.2 dB meaning that at least 93 % of the incident energy was transmitted to the biological medium within the TEM cell.

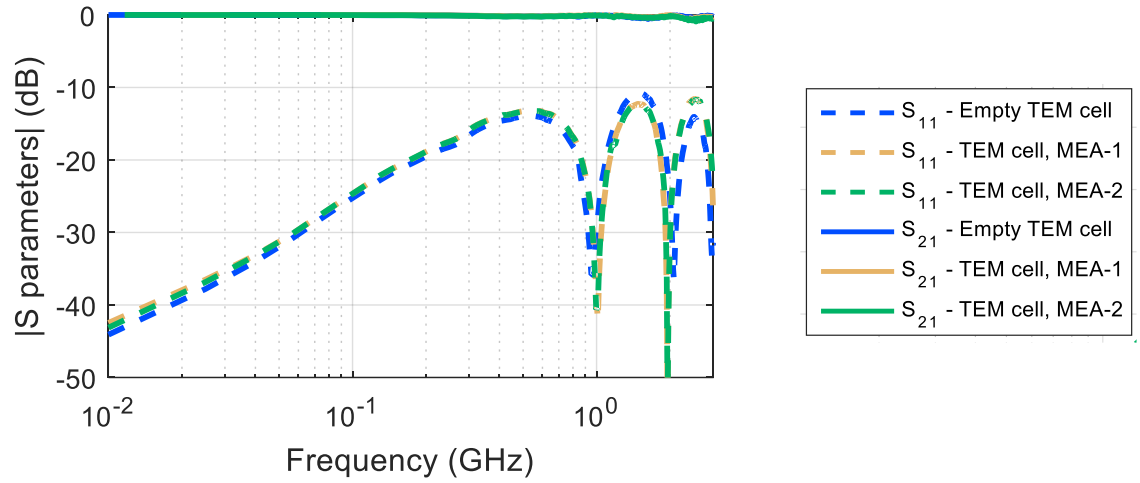


Figure 55 : Reflection ($S_{11}$) and transmission ($S_{21}$) coefficients measured at the terminals of the empty TEM cell, TEM cell with MEA-1, and TEM cell with MEA-2.

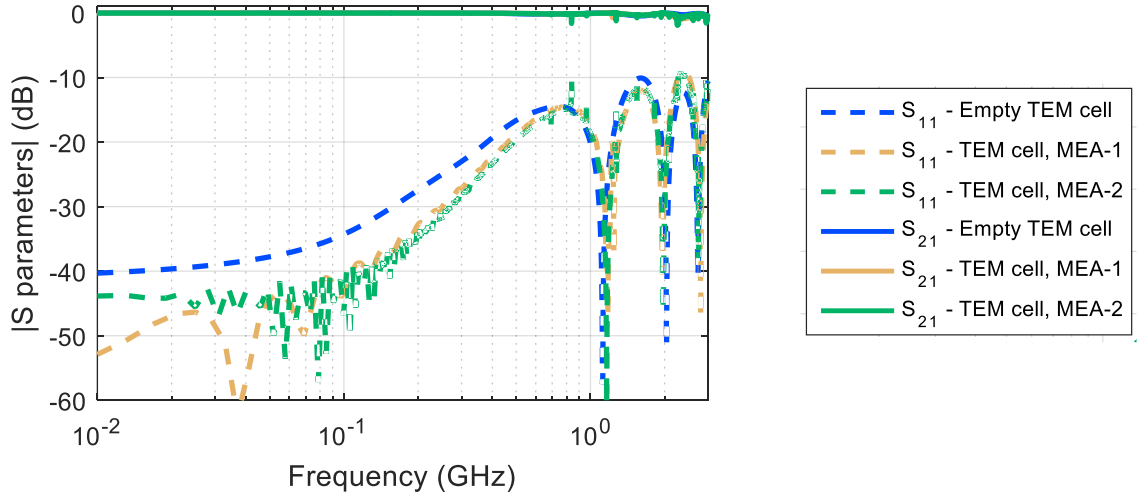


Figure 56 : Numerical reflection ($S_{11}$) and transmission ($S_{21}$) coefficients of the empty TEM cell, TEM cell with MEA-1, and TEM cell with MEA-2.

## III.1.3. Impact of the environment on the MEA dosimetric results

The exposure and recording devices were combined and characterized in different configurations (i.e. suspended, above a dielectric, above a conductor, etc.) to study the impact

of the environmental changes on each MEA. A CW RF signal at 1.8 GHz with various power intensities was transmitted to the input of the TEM cell for 5 minutes exposure each. The MEA's culture chamber was filled with 1 mL of DMEM medium. Measurements consist of temperature assessment of the biological medium with Luxtron thermometer leading to the evaluation of SAR. The temperature recording begins a few minutes before the EMF application and ends a few minutes after. The probe was placed at the bottom and in the center of the culture chamber of the MEA to evaluate the temperature changes in the area of microelectrodes. Figure 57 presents the five configurations used in the experimental assessment of the TEM cell exposure device and the MEA recording device. In the first case, the devices were suspended in the air by 4 metal rods as depicted in Figure 57a. In the second case of Figure 57b, the devices are placed above a dielectric support (i.e. wood). In the third case, the devices are placed on top of a conductor support as presented in Figure 57c. In the fourth case (Figure 57d), the MEA was sealed to the bottom of the TEM cell with metallic foil (i.e. aluminum foil) to mimic a metallic cavity. For the fifth case, the TEM cell and the MEAs were fixed on top of the original electrophysiological setup for bioelectrical activity recording which is composed of an interface board and a pre-amplifier. The pre-amplifier attached to a support sustained the MEA and the TEM cell as shown in Figure 57e. This was custom made with the MEA to connect through conductor pins to the output pads of the MEA and this device is used to collect and amplify the signals recorded by the MEA chip. The pre-amplifier was just used in our experiments as a support and it was not turned on. The metal plate had a rectangular 50 × 50 mm aperture permitting the coupling of the pre-amplifier's pins with the MEA's pads. For reproducible results, each experiment was conducted 4 times minimum.

Figure 57 : Photos of the different experimental configurations used in the evaluation of the exposure system i.e. the TEM cell and the recording device MEA. a) system suspended in the air (open), b) system placed on top of a metal plate, c) system sealed with a metal cavity, d) system placed on the preamplifier of the electrophysiological recordings device.

#### III.1.3.1. MEA-1 recording device

Figure 58 presents the temperature variation recorded with the optical fiber probe within the 1 mL DMEM medium inside MEA-1. Measurements are performed with the TEM cell and the MEA-1 in the five configurations described previously. For MEA-1 the temperature rise measured during the 5 minutes exposure in the first configuration was 6.5°C, 5.8°C, 3.2°C and

a)

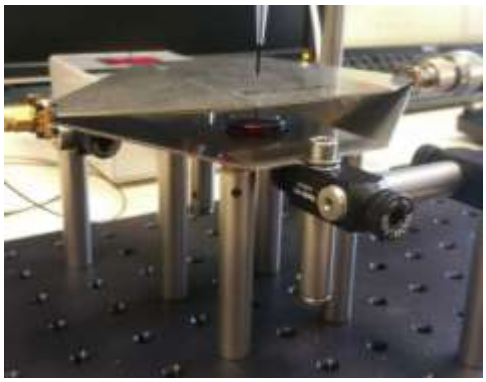

b)

c)

d)

e)

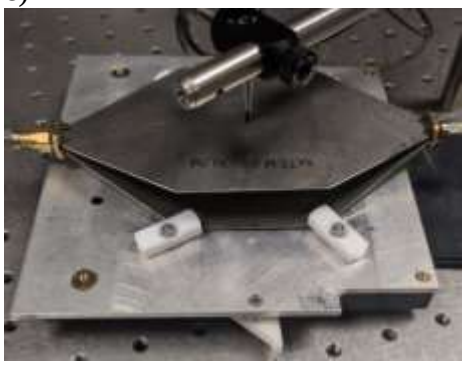

3.6°C respectively for 20 W, 20 W, 10 W and 10 W incident power (Figure 58a). The mean temperature elevation retrieved from the four experiments is 0.32 ± 0.02°C per 1 W incident power.

After the exposure in the second configuration with the dielectric support, the temperature recorded was 3°C for 10 W incident power and it varied between 4.35 and 5.6°C for 20 W (Figure 58b). The average value was calculated to be 0.27 ± 0.03°C per 1 W power which is consistent with the result of the previous configuration since the system was above a dielectric in both cases.

The third configuration consists of placing the TEM cell and MEA-1 above a metal table. The temperature elevation recorded was 1.26°C and 1.2°C for 10 W incident power and 0.7°C and 0.87°C for 20 W (Figure 58c) resulting in an average of 0.07 ± 0.01°C normalized per 1 W power. This mean temperature value is about 4 times lower than the two previous

values which mean that the presence of a conductor material results in the reduction of temperature rise.

The fourth configuration was achieved by sealing the MEA-1 to the TEM cell with metal foil and they were then placed on top of a conductor. The temperature was measured to be 1.6°C, 1.6°C, 0.72°C and 0.44°C for a power of 20 W, 20 W, 10 W and 5 W, respectively (Figure 58d). The 1 W normalized average is 0.08 ± 0.006°C which is comparable to the previous value of the conductor support. The standard deviation is lower meaning that adding conductor layers further stabilizes the MEA and the temperature rise.

For the fifth configuration with the pre-amplifier, temperature increase was recorded to be in the range 4°C - 4.7°C for 20 W and 2.5°C for 10 W (Figure 58e) which leads to an average of 0.23 ± 0.02°C per 1 W. Due to the aperture of the interface board, the average temperature value of MEA-1 is close to the open and the dielectric configurations.

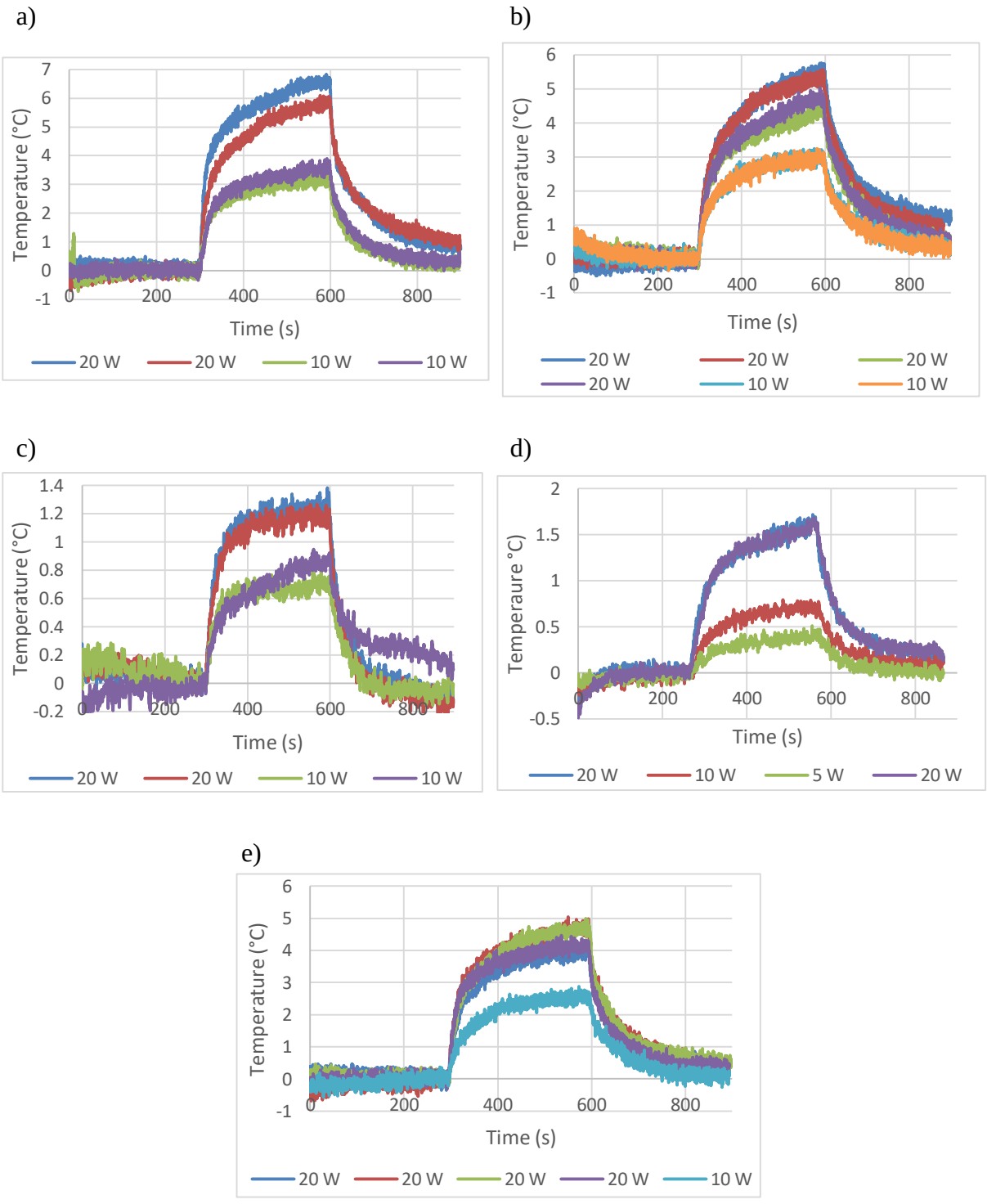


Figure 58 : Evaluation of the temperature variation within MEA-1 filled with 1 ml DMEM medium in different configurations, a) devices suspended by 4 metal rods, b) devices above a dielectric support, c) devices above a conductor support, d) MEA-1 sealed to the bottom of TEM cell with a conductor foil, e) devices fixed on top of the pre-amplifier.

The MEA-1 shows different results proving that surrounding materials can affect its performance. In addition, as this MEA has one reference plane within the PCB with a large

aperture, adding another conductor underneath the device seals the opening and lowers the coupling, thus, decreasing the temperature rise. Furthermore, adding metal layers under the MEA-1 enhanced its stabilization which was proved by the drop of the standard deviation and the improvement of results reproducibility. An opening in the metal plate under the MEA can also influence the MEA's response by increasing the coupling with the culture medium. Due to the large size of the aperture of the pre-amplifier support, the system can be considered as open with a dielectric underneath.

#### III.1.3.2. MEA-2 recording device

The same experiments were achieved with MEA-2 in the same conditions (1 mL of DMEM medium, application of CW at 1.8 GHz with different incident power). The exposure duration for most of the cases was 5 minutes except for the open configuration (MEA suspended on air) where the RF signal application lasted for 15 minutes. The temperature variation measured during each experiment for the five cases described previously is plotted in Figure 59. Within 5 minutes exposure, temperature rise values normalized per 1 W incident power were recorded to be 0.22 ± 0.02°C for a suspended MEA, 0.12 ± 0.01°C for the dielectric support, 0.08 ± 0.006°C for conductor usage, 0.08 ± 0.01°C for conductor foil sealing and 0.1 ± 0.008°C for the use of pre-amplifier system. It is remarkable that for the same configurations, the medium within MEA-2 heated less than that of MEA-1. This can be due to the fact that MEA-2 has more metal layers and smaller opening that results in lowering EMF coupling.

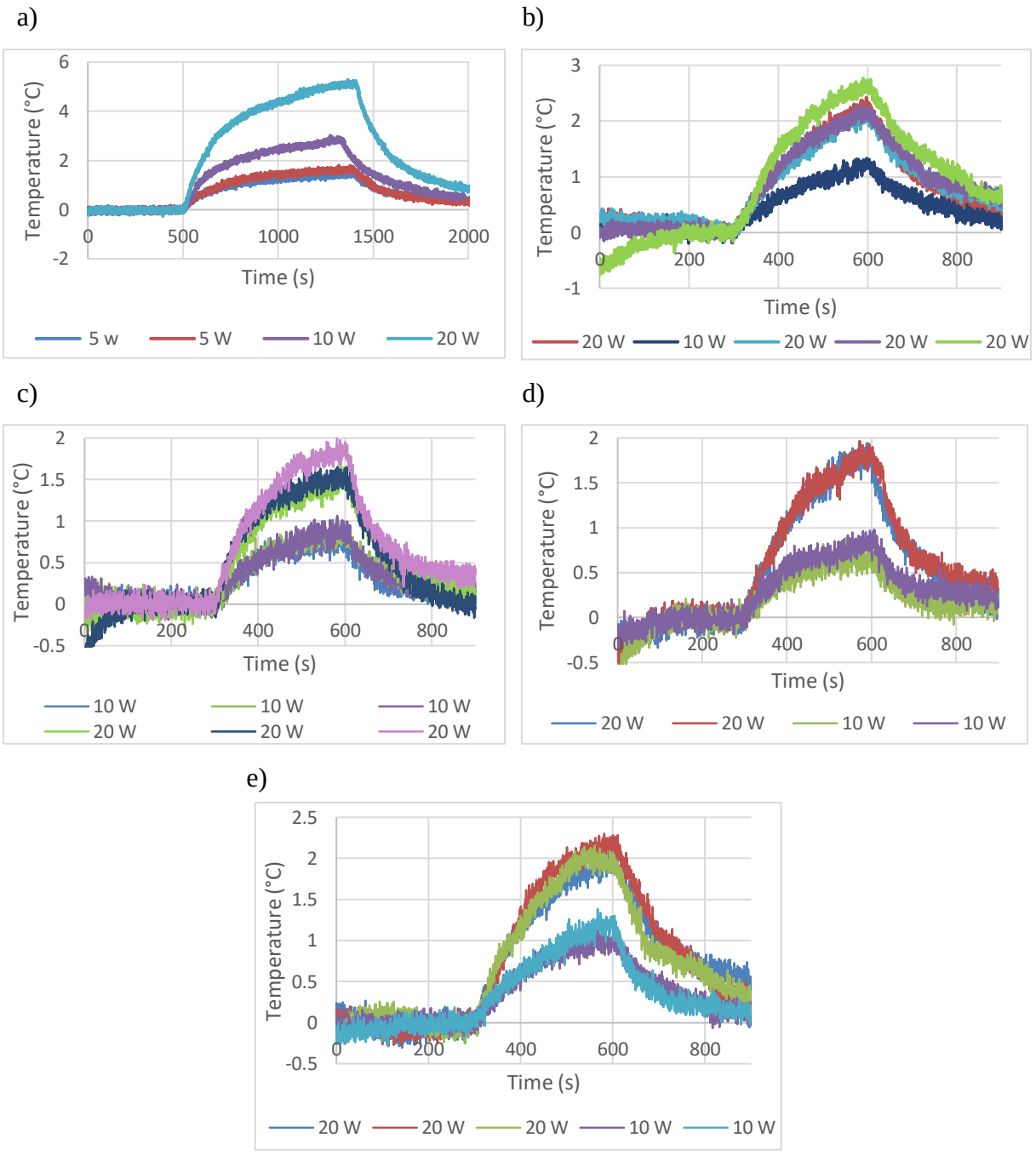


Figure 59 : Temperature variation measured within the MEA-2 in 5 different configurations, a) system suspended, b) Dielectric under the MEA, c) conductor under the system, d) system sealed with aluminum foil, e) system above a pre-amplifier.

Table 7 summarizes the average temperature obtained with the two MEAs for each one of the five configurations. According to the average temperature values, both the MEAs respond similarly to each configuration but with different ratios, the highest temperature rise was recorded when the MEAs were suspended. Adding a conductor below the MEAs decreases the

temperature rise by 78% and 36% for MEA-1 and MEA-2, respectively. For both MEAs, the use of the dielectric or the pre-amplifier produced nearly the same outcomes due to the large aperture of interface board as mentioned previously. To sum up, MEA-2 is steadier and less influenced by the changes made to the surrounding materials and its results have better reproducibility.

| | MEA-1 (°C) | MEA-2 (°C) |
|---|---|---|
| Suspended | 0.32 ± 0.02 | 0.22 ± 0.02 |
| Dielectric support | 0.27 ± 0.03 | 0.12 ± 0.01 |
| conductor support | 0.07 ± 0.01 | 0.08 ± 0.006 |
| Metal foil/cavity | 0.08 ± 0.006 | 0.08 ± 0.01 |
| Pre-amplifier | 0.23 ± 0.02 | 0.10 ± 0.008 |

Table 7 : Average temperature elevation detected with MEA-1 and MEA-2 inside the TEM cell in five different configurations.

### III.1.4. Experimental SAR results

The SAR probe values were retrieved from all the temperature data recorded with the Luxtron probe. SAR values were normalized per 1 W incident power and values were averaged to obtain one SAR probe result per configuration. The SAR probe results are summarized in Table 8. These values have the same variation as the temperature as high temperature variations induce high SAR values. Hence, the highest SAR probe was obtained with the open case with an efficiency of 60.7 W/kg for MEA-1 and 6.4 W/kg for MEA-2. The addition of a conductor lowers the efficiencies by 75.3% and 45.3% respectively for MEA-1 and MEA-2.

MEA-2 SAR probe values are rather homogenous which proves the stability of the device as it is less influenced by the proximate environment. On the contrary, MEA-1 SAR results show a noteworthy disparity indicating the sensitivity of the device to the surrounding materials.

| | MEA-1 (W/kg) | MEA-2 (W/kg) |
|---|---|---|
| Open | 60.7 ± 15.66 | 6.4 ± 1.53 |
| Dielectric support | 45 ± 15 | 3.6 ± 0.9 |
| Conductor support | 15 ± 3 | 3.5 ± 0.5 |
| Metal foil / Cavity | 5.2 ± 0.8 | 3.3 ± 0.4 |
| pre-amplifier | 44.05 ± 6 | 3.9 ± 0.6 |

Table 8 : Normalized SAR probe values retrieved from temperature measured with Luxtron probe at the center and bottom of the DMEM medium in both MEAs for each configuration.

### III.1.5. The influence of the lid on the temperature elevation

When the liquid biological medium is heated under EMF exposures, evaporation can occur and when the quantity of medium decreases, SAR values may vary as well. Hence, to prevent evaporation, a plastic lid was placed on top of the MEA with an opening for probe insertion (Figure 60). The temperature change plotted in Figure 61 was recorded within the culture media in the MEA-1 with and without a lid. A 20 W incident power was applied and the temperature plotted in Figure 61a corresponds to the configuration where the TEM cell and MEA-1 are above a conductor support. Figure 61b corresponds to the dielectric support configuration. The recordings were conducted several times in all the different configurations, but no consistent results proved that the usage of the lid significantly affects the temperature, particularly on the initial slope induced by temperature elevation where SAR values are calculated. Both temperature curves (i.e. with and without lid) provide similar SAR values as they rise with the same slope. Temperature stabilizes nearly at the same value by 0.5°C difference at most.

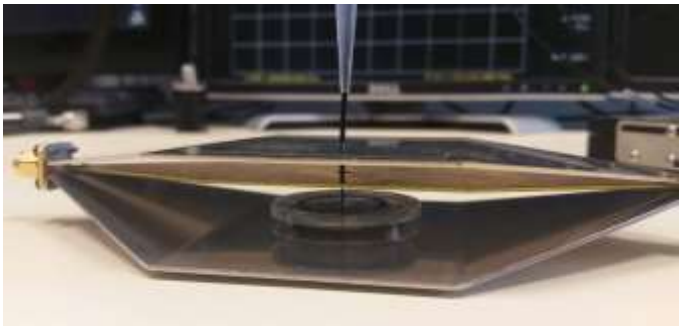

Figure 60 : Temperature recording with Luxtron probe within the biological medium inside MEA-1 covered with a lid.

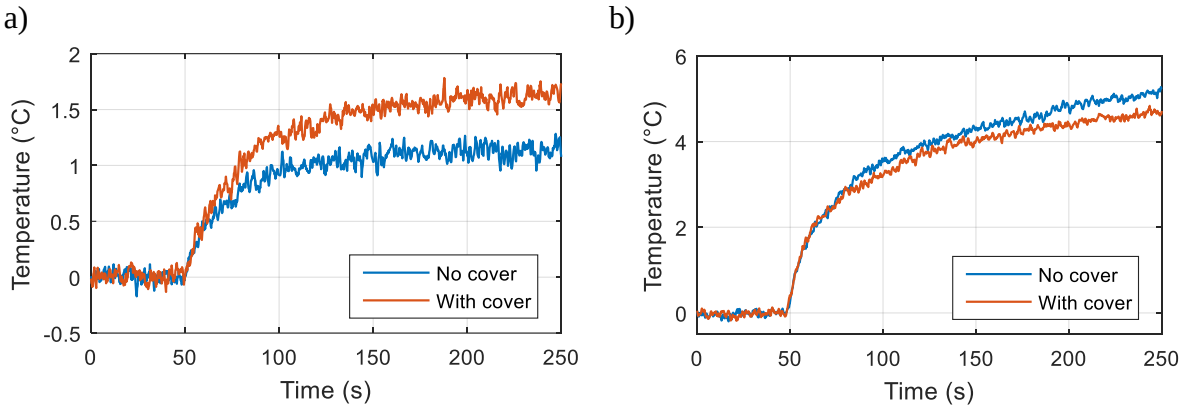


Figure 61 : Temperature change recorded within the MEA-1 during 20 W RF exposure with and without the lid, a) conductor configuration, b) dielectric configuration.

# III.2. Numerical modeling and characterization of MEAs environment

To further investigate the impact of the materials surrounding the MEAs on the E-field propagating within the TEM cell, the five experimental configurations were reproduced numerically as shown in Figure 64. The open TEM cell with an aperture of 24 mm diameter and the MEA with its two versions were modeled and simulated. All metallic components were designed as Perfect Electric Conductor (PEC) and as a preliminary design, the MEAs were simplified to gain in simulation time. For the MEA-1 (Figure 62), all the electrodes and conducting lines and the contact pads were disregarded, thus, the design consists just of the glass chip, the culture chamber, the PCB with the reference plane inside including the 10 mm diameter aperture. As for the MEA-2 (Figure 63), almost all the components were modeled except the electrodes and the top conductor lines. The glass chip, the culture chamber, the PCB with the 4 reference planes, the inner vias and lines also the bottom pads were considered. The MEA-2 has also a glass observation cavity which was modeled with a 2.5 mm diameter.

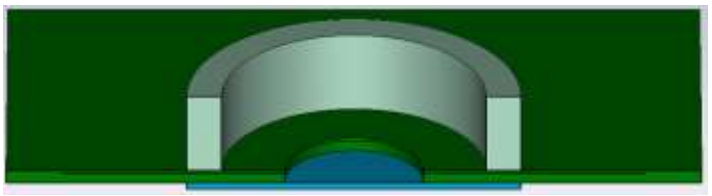

Figure 62 : Cross section of the MEA-1 simplified design on CST software consisting of the glass chip, culture holder, the PCB and the embedded reference plane.

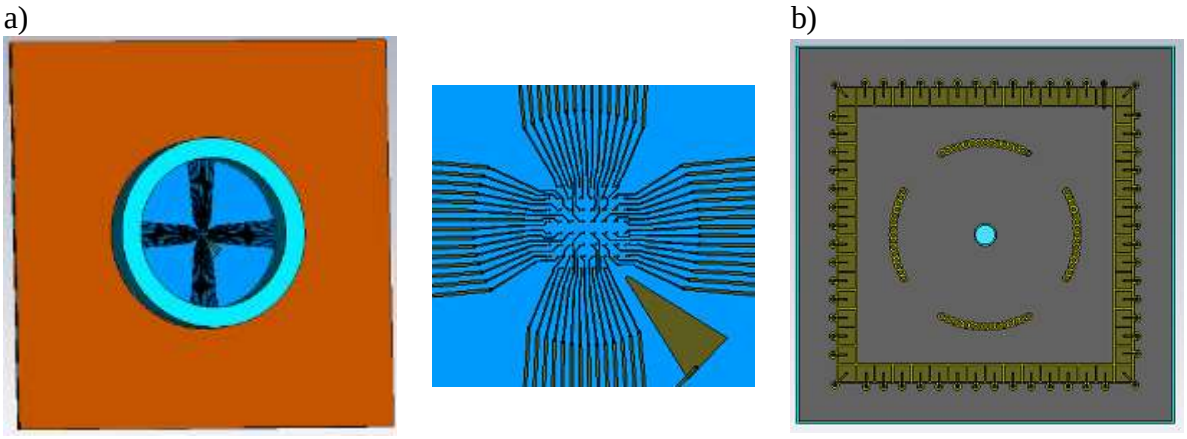


Figure 63 : MEA-2 full design on CST software, a) top view of the microelectrodes, the top conducting lines and the culture holder with a zoom central area of the microelectrodes, b) bottom view of the contact pads.

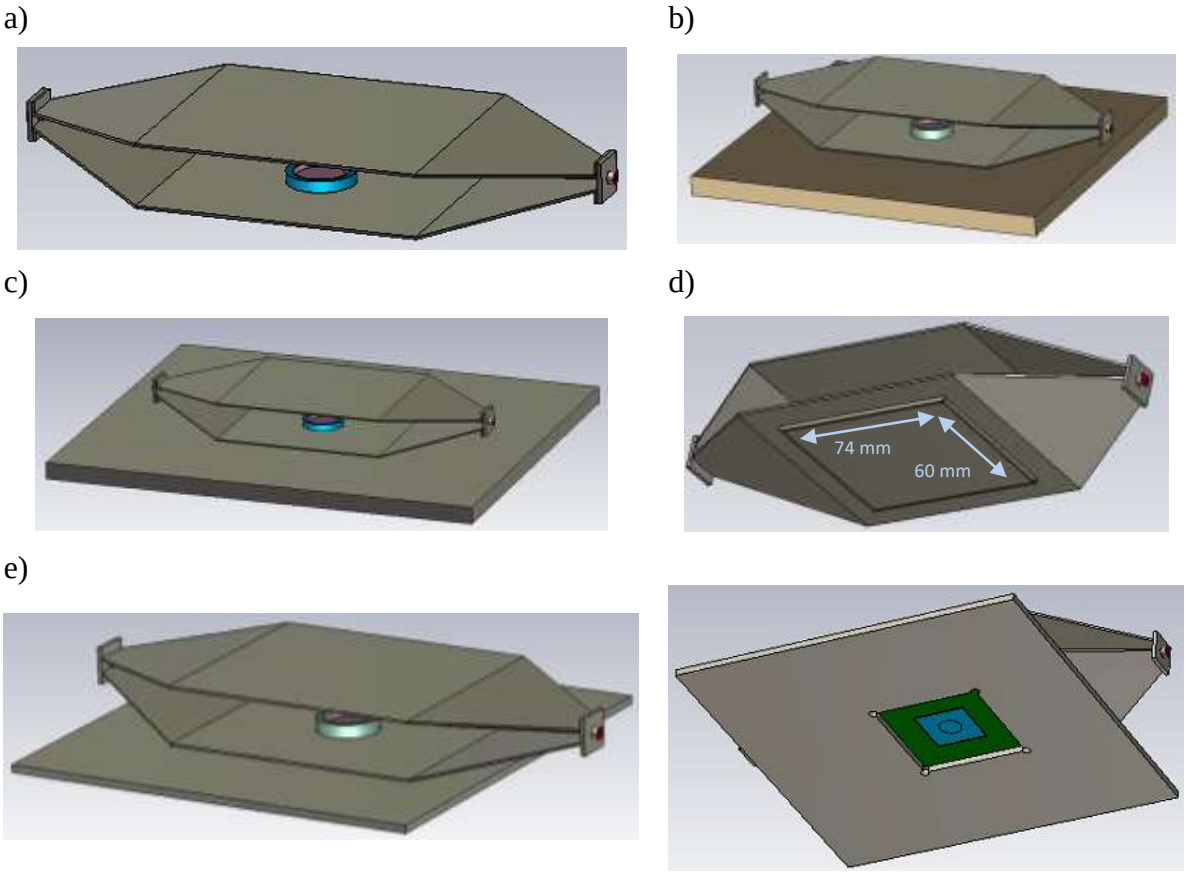


Figure 64 : Numerical design of the TEM cell and MEA-1 in several configurations; a) open (suspended), b) dielectric underneath, c) above a conductor, d) MEA sealed with a metal cavity, e) metal plate of the pre-amplifier.

| | Conductivity (S/m) | Relative permittivity | Volume density ($kg/m^3$) |
|---|---|---|---|
| Biological medium | 2.3 | 74.2 | 1000 |
| Culture chamber<br>Glass chip<br>Observation cavity (MEA-2) | - | 4.6 | 2230 |
| PCB | - | 4.4 | 1850 |

Table 9 : Electric properties used in simulations of the MEAs components at 1.8 GHz.

The electromagnetic dielectric properties of the MEAs components are detailed in Table 9. The culture medium was defined with the same values as previously in section II.2.5. The culture chamber, the glass chip, the observation cavity, and the PCB were defined as loss-free. The heights of culture medium designs within the MEAs correspond to 1 mL used in experiments and they were meshed with a uniform 0.1 × 0.1 × 0.1 mm spatial grid.

The numerical designs of the material surrounding the system are depicted in Figure 64. For the open configuration (Figure 64a), no material was added under the MEA. For the dielectric case (Figure 64b), a 10 mm thick rectangular loss-free brick was added under the MEA with $\varepsilon_r = 3$ and $\rho = 500$ kg/m$^3$ density. For the metal configuration (Figure 64c), a 10 mm thick conductor was designed below the MEA and defined as PEC. For the fourth experimental configuration (Figure 64d), the MEA-1 was sealed with a metal cavity to the bottom of the TEM cell. The cavity has 1 mm thick walls and its bottom is in contact with the MEA. The cavity was simulated with two different inner dimensions 74 × 60 mm and 60 × 60 mm but with the same height. The 74 × 60 mm cavity is referred to as cavity 1 and the 60 × 60 mm as cavity 2. Regarding the pre-amplifier configuration (Figure 64e), only the metal interface board connected on top of the pre-amplifier was modeled with the proper aperture dimensions.

SAR distribution results obtained thru numerical simulations of the TEM cell with the MEAs in each configuration at 1.8 GHz are represented in Figure 65 and Figure 66 for MEA-1 and MEA-2, respectively. Table 10 summarizes the values of SAR retrieved from the culture medium within both MEAs. The SAR probe refers to the values averaged over 1 mm$^3$ volume in the bottom center of the medium which represents the probe measuring volume. The SAR bottom refers to the values that were averaged at the cell level with 100 µm thickness. The bottom layer volume is about 7.9 mm$^3$ and 28.4 mm$^3$ for MEA-1 and MEA-2, respectively. This volume difference is due to the difference in the structure of the MEAs. Bottom SAR

values are presented without standard deviation because the variation of SAR over the medium height was not evaluated.

Figure 65 presents the SAR distribution at 1.8 GHz of all the six cases simulated, with horizontal cut planes at the cell level and vertical cut planes at the center of the medium. The results show the influence of the proximate materials on the MEA's response. Suspending the recording device, placing a dielectric below, or adding the metal board of the pre-amplifier induce similar SAR distribution. In these cases with MEA-1, in Figure 65a, b and f, the SAR shows less homogeneity with the highest values of SAR probe around 25 W/kg. The SAR bottom values of these cases are similar as well. The design that offers good homogeneity and low SAR values is the one with the conductor plane (Figure 65c). The SAR probe and SAR bottom obtained are the lowest amid the rest of the values. They are determined to be 0.85 et 1.3 W/kg, respectively which makes them lower by 96.5% and 95% compared to the highest values. This indicates that the presence of conductors lowers the coupling of the biological medium with E-Field.

| | MEA-1 (W/kg) | | MEA-2 (W/kg) | |
|---|---|---|---|---|
| | SAR probe | SAR bottom | SAR probe | SAR bottom |
| Open | 24.30 ± 5.70 | 26.50 | 0.51 ± 0.27 | 0.96 |
| Dielectric support | 25.50 ± 6 | 27.65 | 0.52 ± 0.20 | 0.91 |
| Conductor support | 0.85 ± 0.53 | 1.30 | 1.27 ± 0.34 | 1.00 |
| Cavity 1 (74 × 60 mm) | 5 ± 1.60 | 12 | 1.44 ± 0.38 | 1.10 |
| Cavity 2 (60 × 60 mm) | 19 ± 3.10 | 51.40 | 1.42 ± 0.40 | 1.10 |
| Pre-amplifier | 24.30 ± 5.73 | 26.45 | 0.46 ± 0.26 | 0.90 |

Table 10 : Numerical SAR values retrieved when simulating the simplified MEAs.
(SAR normalized per 1 W incident power)

Figure 65d and Figure 65e depict the SAR distribution within the MEA-1 while it is sealed with the two cavities (74 × 60 mm and 60 × 60 mm). SAR distribution maps of both these designs show higher values compared to the metal plate configuration. They present good homogeneity at the cell layer but with uneven levels which shows the importance of the cavity dimensions. The 60 × 60 mm cavity resonated at 1.8 GHz inducing higher SAR values within the culture medium which explains the disparity with the 74 × 60 mm cavity results.

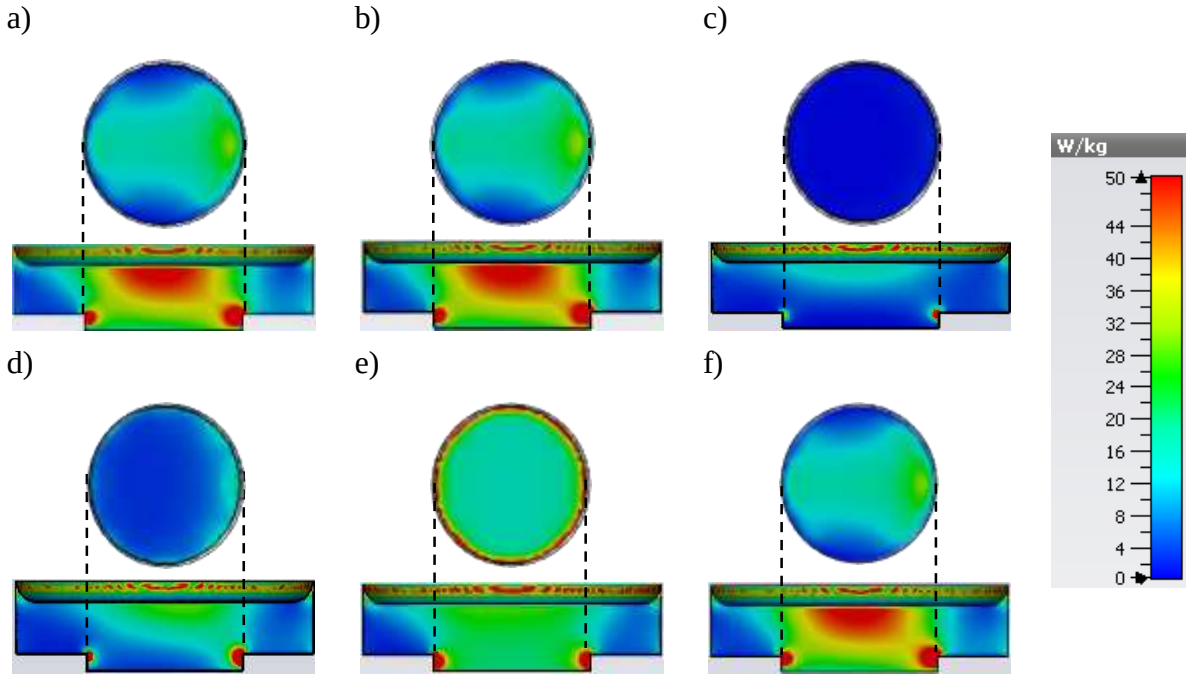


Figure 65 : Numerical SAR distribution of culture medium within MEA-1 at 1.8 GHz. SAR at the cell level along a vertical cut. a) system suspended, b) system above a dielectric, c) system above a conductor, d) system sealed with metallic 74 × 60 mm cavity, e) system sealed with metallic 60 × 60 mm cavity, f) system fixed above the signal pre-amplifier.

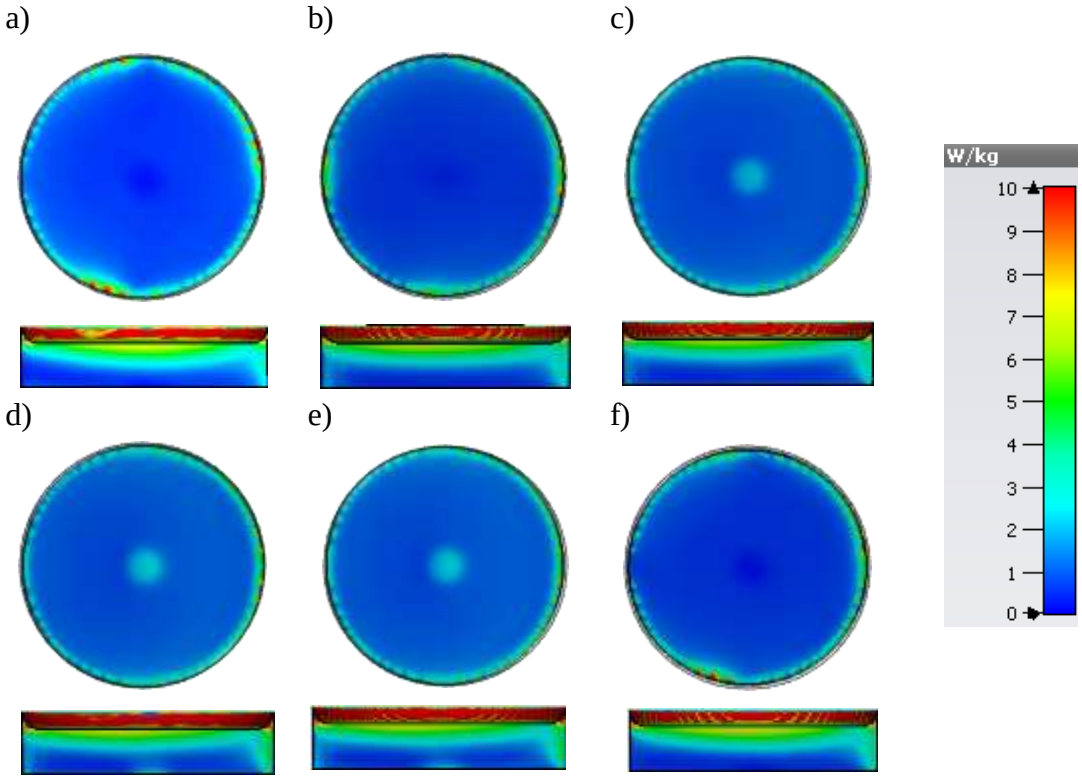


Figure 66 : Numerical SAR distribution of culture medium within MEA-2 at 1.8 GHz. SAR at the cell level along a vertical cut. a) system suspended, b) system above a dielectric, c) system above a conductor, d) system sealed with metallic 75 × 60 mm cavity, e) system sealed with metallic 60 × 60 mm cavity, f) system fixed above the signal pre-amplifier.

The SAR efficiencies increased by about 4 times from 5 to 19 W/kg for the SAR probe and from 12 to 51 W/kg for the localized SAR.

Figure 66 presents the SAR distribution at 1.8 GHz of all the six cases simulated, with horizontal cut planes at the cell level and vertical cut planes at the center of the medium. The numerical design of the MEA-2 showed different responses regarding the proximate materials compared to the MEA-1. It is noticeable that the results are comparable and show great homogeneity despite the changes performed on the system. The numerical results agreed with the experimental ones regarding the similar SAR results of the open, dielectric and pre-amplifier cases.

The values of SAR presented in the horizontal cut of Figure 66c, d and e, show a slight increase at the center due to the metal plate and cavities. This resulted in the rise of the SAR probe by roughly 3 folds compared to the outcomes of the rest of the cases. This variation opposes to the measurement as the SAR lowers while using a metal plate. The area where the SAR increased corresponds to the observation opening of the MEA-2. Vertical SAR cuts depict a gradual increase of energy along the medium height but it is considered not significant. Unlike the first MEA, the cavity dimensions did not influence the response of the device and simulations confirmed the experimental results about the stability of this MEA. MEA-2 has good isolation from external environment changes and it induces less temperature and SAR increase within the sample.

# Conclusion

This chapter was dedicated to the macroscale investigations of the microelectrode arrays (MEA-1 and MEA-2). First, the electrophysiological microsystems were described that were developed to record the spontaneous electrical activity of neuronal networks under RF exposure. The MEAs are based on microelectrodes and they show some differences in their designs and structures. Thus, macroscale dosimetry was achieved for both devices numerically and experimentally.

The experimental temperature and SAR assessments with both MEAs showed that both the MEAs respond similarly to each configuration. For example, the highest temperature rise was recorded when the MEAs were suspended and by adding a conductor below the MEAs the

total temperature elevation decreases. However, this decrease was not with the same ratios as the temperature within the MEA-1 lowered by 78% and that of MEA-2 lowered by 36%. MEA-2 is steadier and less influenced by the surrounding materials also the MEA-2 results have better reproducibility. On the contrary, the MEA-1 SAR results show a noteworthy disparity indicating the sensitivity of the device to the surrounding materials.

Numerical simulations were conducted with simplified versions of the devices. The numerical results agreed with the experimental. The SAR spatial distribution showed remarkable variation within MEA-1 confirming its sensitivity to surrounding materials. The SAR spatial distributions of MEA-2 were highly homogenous in comparison proving its stability. However, numerical and experimental SAR probe values showed some dissimilarities likely due to the lack of the MEAs micro-components in the numerical designs.

Since the macroscale evaluation of the MEAs was performed and the efficiency of the Rhod-B dye technique was validated as well at the macroscopic scale, the characterization of the MEAs at the microscopic scale can proceed by exploiting the fluorescent dye.

# Chapiter IV.

## Microscale dosimetry

# Introduction

The Temperature-dependent dye Rhod-B was assessed at the macroscopic scale with TEM cell. After the characterization of the dye and the optimization of the exposure settings, this technique showed good accuracy and high resolution. Standard measuring tools shows limitations regarding their size that is not suitable for measurements within microsystems and within small sample volumes. Therefore, we had recourse to this dye based technique to investigate the thermal effects induced at the cellular layer within microsystems and to assess the impact of the microelectrodes on the neurons within the MEAs to further contribute detecting other biological changes that can occur under RF exposure. This chapter aims to test the efficiency of the dye with microsystems.

The Rhod-B technique was utilized to complete the evaluation of MEA recording devices. It is important to guarantee homogenous cell exposure and to study the impact of the electrodes on their exposure. A potential coupling of the electrodes can induce the exposure of nearby neurons to higher E-field intensity which may perturb, in turn, the bioelectrical activity recordings and lower the accuracy of biological results. Microscale measurements defined the homogeneity levels within both MEAs at the electrodes area and the numerical analysis focused on the assessment of the new MEA design (MEA-2).

After the microscopic characterization of the MEAs, the objective was to characterize another microsystem based on the Rhod-B dye technique. The microsystem under test is a microchannel chip that operates with a micrometric liquid medium quantity. Thus, as an intermediate step, experiments were firstly conducted with a drop of medium of a few microliters labeled with the biological marker on a glass slide. This step allows testing the microscopic measurement technique before further experiments. Numerical analysis is presented showing the SAR spatial distribution within the drop.

The microchannel exposure device is investigated both experimentally and numerically to quantify the local E-field variation between its electrodes and the local SAR values. Exposure devices that are based on microelectrodes can apply E-fields with extremely high intensity even when the incident power is low. Hence, it is crucial to assess the local E-field intensity propagating between the electrodes and the thermal effects induced to avoid extreme heating that can lead to the cell death during the experiments and cause erroneous biological outcomes.

# IV.1. Microelectrode Array (MEA)

From the macroscale dosimetry of the MEAs presented in chapter 3, we determined that the material supporting or placed under the MEA is important and can impact the response of these electrophysiological recording devices. The investigations showed that the first MEA is more sensitive to surrounding materials, whereas the second one is more stable with better homogeneity. It is, therefore, crucial to investigate the devices at the microscopic level. Thereafter, Rhod-B was exploited after calibration to achieve this finer characterization.

The evaluation of the MEAs consisted of fluorescence and temperature measurements during the application of the CW signal at 1.8 GHz. The signal was applied with 20 W power for 1 minute. The fluorescence intensity was detected with the 20x microscope objective with 1 record/s rate. This objective allows the recording from a 0.57 mm² surface. The light emitted by the microscope camera was set at 1 ms and 2.5 % intensity. The temperature was measured simultaneously using the fiber optic probe with 4 records/s rate. The recordings were conducted at several positions within the MEAs to inform about the spatial distribution of temperature within the biological sample.

## IV.1.1. Microelectrode Array MEA-1

Fluorescence intensity and temperature were recorded in five different positions within the MEA-1 (i.e. center on top of the electrodes, upper lines, lower lines, right lines, left lines). The measuring positions are illustrated in Figure 67 by the red dots. These measurements were conducted to determine the temperature variation in each area and to analyze the homogeneity within the MEA. Figure 68a illustrates the electrodes area of the MEA where the fluorescence was recorded during the application of the signal. The fiber optic probe was placed around the same area to measure the temperature without disturbing the fluorescence measurements by avoiding the microscope detection window. A reversed microscope is used, thus, the MEA was placed above the objective. The dark areas represent the electrodes and the conductor lines. The biological medium is observed from the lighter surfaces.

Fluorescence intensity was collected from the surfaces represented by yellow squares. The detection was repeated 5 times to ensure reproducibility. To evaluate the effects of the electrodes on the fluorescence, among the areas chosen, we selected surfaces with electrodes or

Figure 67 : Photo of MEA-1 with red dots representing the positions where fluorescence and temperature were recorded (i.e. electrodes area, upper lines, lower lines, right lines, left lines).

a) b)

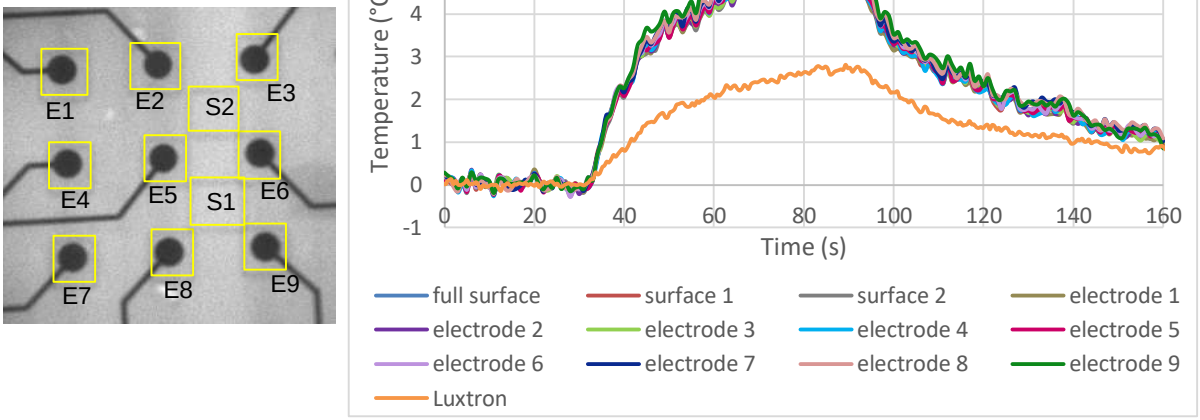


Figure 68 : Fluorescence recorded at the electrodes area of the MEA-1, a) image taken by the microscope 20x objective of the MEA electrodes. The yellow squares represent the surface from which the fluorescence data was collected, b) temperature variation retrieved from the fluorescence intensity measured at several areas within the caption and compared to the temperature measured with the probe.

without electrodes. Results were converted to temperature with the coefficient α equal to -57 and were plotted alongside the temperature measured with Luxtron thermometer (see Figure 68b). The temperature variation retrieved from the several positions within the fluorescence image (Figure 68a) is similarly showing a good uniformity of temperature and by extension of E-field exposure. The values extracted from surfaces with and without electrodes are similar indicating that the electrodes do not cause additional coupling that may lead to a further temperature rise. Results emphasize the great homogeneity in the areas between the electrodes of the MEA-1.

The maximum temperature was recorded to be around 5.4°C which corresponds to 0.27°C per 1 W incident power. Luxtron probe's outcome was around 50 % lower comparing to the Rhod-B results and that can be explained by the differences in the measuring volume. The probe averages temperature over 1 mm height. The microscope objective detects the fluorescence on a surface with a much smaller thickness and the temperature along the medium height can vary.

For the case of MEA-1, the size of the observation aperture is large enough to allow Rhod-B fluorescence measurements at the conducting lines area. The experiments conducted on top of the MEA lines were repeated 3 times in each position. Figure 69 illustrates the position (red dot) where fluorescence intensity and temperature were recorded. Images were taken by the microscope 20x objective within that position (Figure 69a) during the RF exposures. Figure 69b is a zoom on the red point captured for fluorescence measurements. The dark areas represent the conductor lines and the biological medium is present in the lighter surfaces where the fluorescence is measured. In this position, temperature values retrieved from the different surfaces selected and curves were plotted in Figure 70. The results are similar and at the end of the exposure, the temperature has reached 3.7°C which is 30 % lower than what was obtained at the electrodes area (Figure 68b). The elevation measured by Luxtron probe reached 2.36 °C, this value is 34.5 % less than that obtained by Rhod-B technique.

a) b)

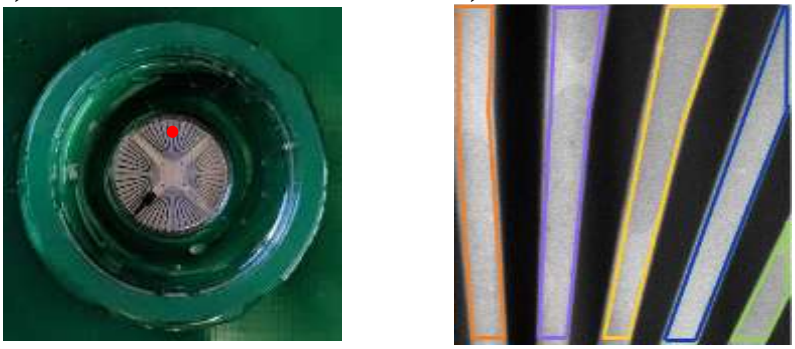

Figure 69 : Fluorescence recorded at the upper section of the MEA-1, a) photo of MEA-1 with red dot representing the position where the fluorescence intensity and temperature were recorded, b) image recorded by the microscope 20x objective of the MEA-1 showing the upper conductor lines.

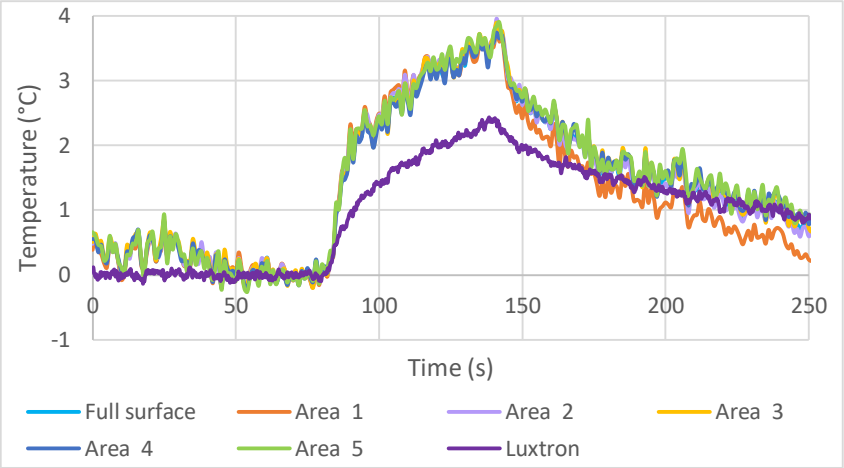


Figure 70 : Temperature variation retrieved from the fluorescence intensity measured between the upper lines of MEA-1 (Figure 69b) and compared to the temperature measured directly with the Luxtron probe.

The fluorescence intensity was then detected at the lower section of MEA-1 represented by the red dot in Figure 71a. The temperature was measured as well in the same area as the Luxtron probe. The image shows the medium between the lines that are numbered to match the temperature curves of Figure 72. The heat curves determined with the microscopy technique have comparable progressions with a 5.4°C maximum temperature increase. The Luxtron probe detected a maximum of 1.35 °C that is 75 % lower compared to the Rhod-B technique. This difference is considerably higher than that of the two preceding results.

a)

b)

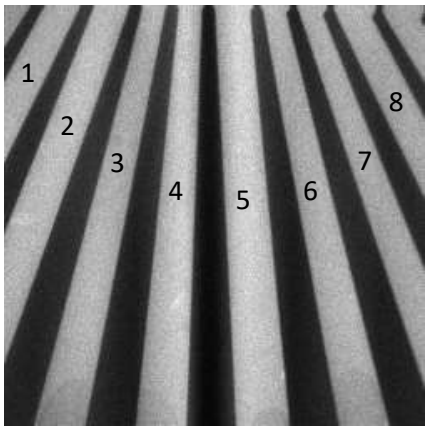


Figure 71 : Fluorescence recorded at the lower section of the MEA-1, a) photo of MEA-1 with red dot representing the position where the fluorescence intensity and temperature were recorded, b) image recorded by the microscope 20x objective of the MEA-1 showing the lower conductor lines.

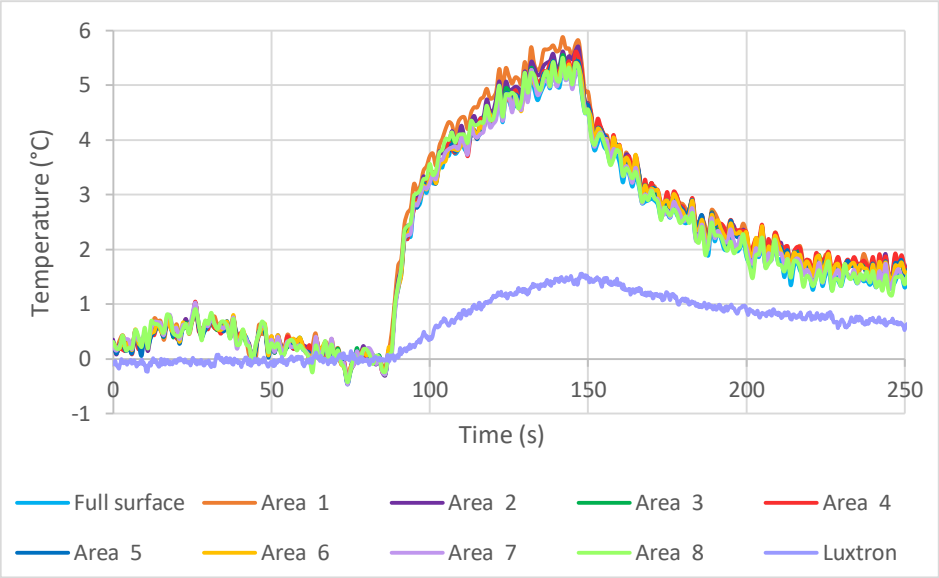


Figure 72 : Temperature variation retrieved from the fluorescence intensity measured between the lower lines of MEA-1 (Figure 71b) and compared to the temperature measured directly with the Luxtron probe.

The measurements were performed in the right section of MEA-1 represented by the red dot in Figure 73a. The temperature elevation is retrieved from the four areas enumerated in Figure 73b. The temperature curves determined with Rhod-B technique are illustrated in Figure 74 along the variation recorded with the thermometer. Luxtron probe recorded a maximum temperature value of 2.5 °C which is lower by more than 45 % compared to the outcome obtained by fluorescence measurements and showing a maximum of 4.8 °C.

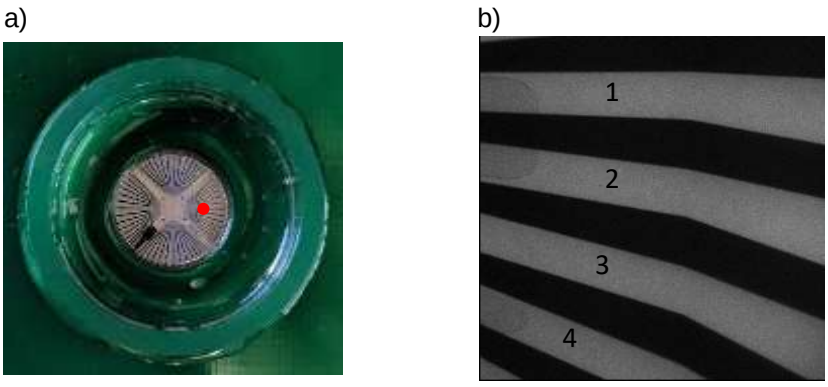


Figure 73 : Fluorescence recorded at the right section of the MEA-1, a) photo of MEA-1 with red dot representing the position where the fluorescence intensity and temperature were recorded, b) image recorded by the microscope 20x objective of the MEA-1 showing the right conductor lines.

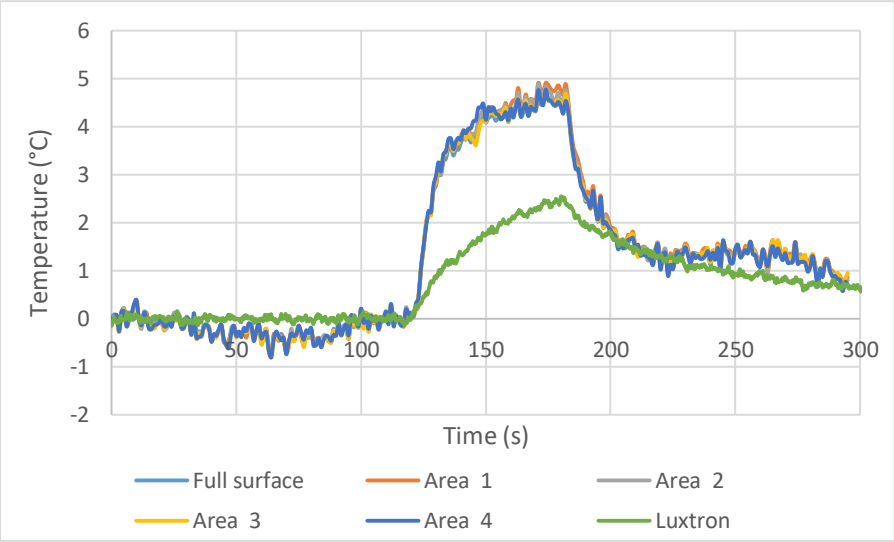


Figure 74 : Temperature variation retrieved from the fluorescence intensity measured between the lines at the right section of MEA-1 (Figure 73b) and compared to the temperature measured directly with the Luxtron probe.

Finally, the recordings at the left section of the MEA-1 (red dot Figure 75a) were achieved. The fluorescence data were collected from 5 different areas enumerated in Figure 75b and the temperature results determined within these surfaces were plotted in Figure 76. The maximum temperature reached was 4.6 °C from Rhod-B technique and 1.8 °C detected with the fiber optic probe. The macroscopic temperature value is 61 % lower compared to the Rhod-B technique outcome.

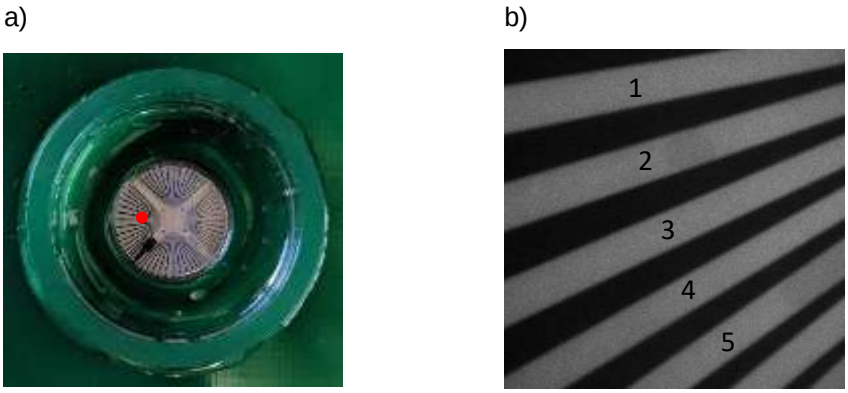


Figure 75 : Fluorescence recorded at the left section of the MEA-1, a) photo of MEA-1 with red dot representing the position where the fluorescence intensity and temperature were recorded, b) image recorded by the microscope 20x objective of the MEA-1 showing the left conductor lines.

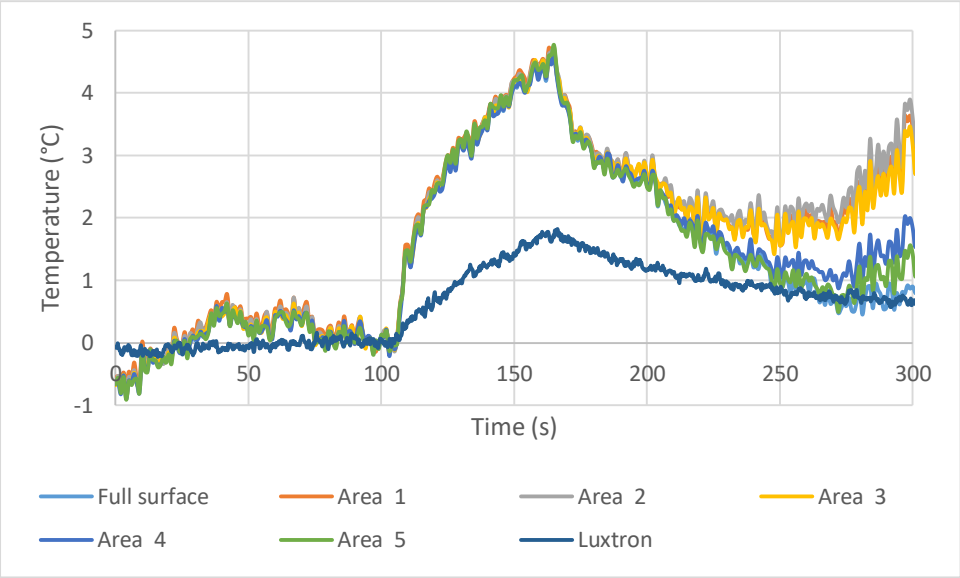


Figure 76 : Temperature variation retrieved from the fluorescence intensity measured between the lines at the left section of MEA-1 (Figure 75b) and compared to the temperature measured directly with the probe.

Both measurement techniques allowed the assessment of the temperature variation in different positions within the MEA-1. The Rhod-B technique offers more precise outcomes by providing temperature variation with higher spatial resolution and accuracy. The highest temperature value of 5.4 °C was obtained with this method at the center of the MEA-1 (i.e. microelectrodes) and at the lower section (i.e. lines). The temperature detected at the right and left positions are similar with 4.8 and 4.6 °C, respectively. The lowest value was obtained at the upper position with 3.7 °C presenting a difference of 31 % from the highest value.

SAR was then calculated from the previous results presented and values were organized and displayed in a schematics in Figure 77 according to the position where measurements were conducted. The red values correspond to the efficiencies and the standard deviation of the SAR probe computed from temperature data recorded by the Luxtron probe. The blue values are the microscale SAR determined from the fluorescence intensity obtained by the microscopy technique. As mentioned, the highest temperature was detected in the center of MEA-1 where the microelectrodes are located. Thus, the highest SAR values are at the zone of the electrodes with efficiencies of 70 and 159 W/kg/Winc for the SAR probe and the micro-local SAR, respectively. As shown in this schematics, micro-local SAR values are significantly higher than the SAR probe efficiencies. Both methods revealed the inhomogeneity of SAR within MEA-1.

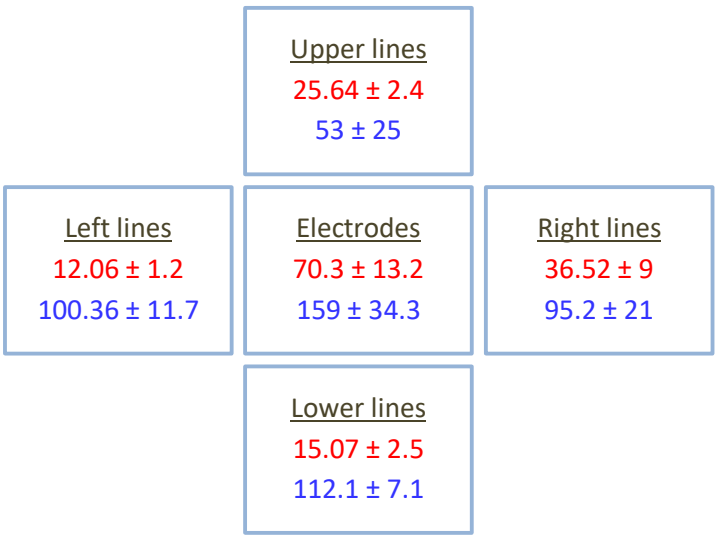


Figure 77 : Experimental SAR results obtained from temperature measured with the **fiber optic probe** and from fluorescence intensity of **Rhod-B** dye at different positions within the MEA-1.
SAR normalized by 1 W incident power.

Rhod-B technique showed that within the MEA-1, the biological sample is not exposed homogenously because the temperature elevation values retrieved from the fluorescence data at different positions were in disparity. This inhomogeneity is not critical because, during the biological experiments with the MEAs, neuronal activity is measured from the nerve cells placed at the electrodes area at the center of the device. The temperature detected at the microelectrodes area is homogenous reflecting the uniformity of the exposure. It was also found from Luxtron probe and Rhod-B technique measurements that the highest temperature values were obtained at the center of MEA-1, conducting to obtaining the highest SAR values. The two methods did not provide similar temperature values because of their measuring differences.

The same measurements that consist of temperature recording with the probe and fluorescence intensity detection were performed as well with MEA-2 and results are detailed in the next section.

### IV.1.2. Microelectrode Array MEA-2

Temperature measurements were conducted using the fiber optic probe at several positions within the MEA-2. These positions are shown in Figure 78 by red and green dots. The red dots are for the areas where lines and microelectrodes are present and the green dots represent the measuring positions where there are no micro-components (only glass, PCB and

the reference planes inside). The choice of these positions was made to study the impact of the metallic components on the SAR probe and evaluate its homogeneity.

Due to the small size of MEA-2 observation cavity, microscopic monitoring is only possible in the microelectrodes area in the center of the MEA-2. Thus, Rhod-B fluorescence intensity was only measured at this position (center red dot in Figure 78). The small observation cavity was limiting our measuring surface and complexifying the focus adjustments. At the center of the MEA-2, temperature and fluorescence intensity were measured and the temperature was determined with Rhod-B technique only at the electrodes level. The temperature variation in this zone obtained with both methods is plotted in Figure 79. The maximum temperature elevation retrieved from the fluorescence data is around 1.6 °C (Figure 79b) and the one obtained with the fiber optic probe is 47 % lower and it was measured to be about 0.85 °C. The difference can be explained by the probe positioning uncertainty which should be taken into account as it is not placed in the same microscopic window frame. Indeed, recordings cannot be achieved by a microscope if the probe is covering the observation window, so they should not overlap. Also, the microscopy technique based on Rhos-B dye has better spatial resolution compared to the fiber optic probe method.

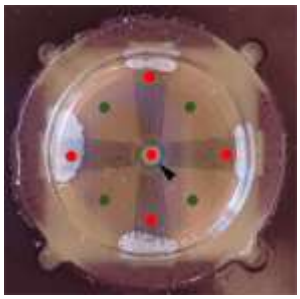

Figure 78 : Photo of MEA-2 with red and green dots representing the positions where the temperature was recorded.

The temperature variation from the fluorescence intensity assessed around each electrode (Figure 79a) and from the full image surface show a great similarity confirming the homogeneity of the E-field exposure. The temperature curve of electrode 3 presents slightly higher values which are probably due to the microscope focus.

a) b)

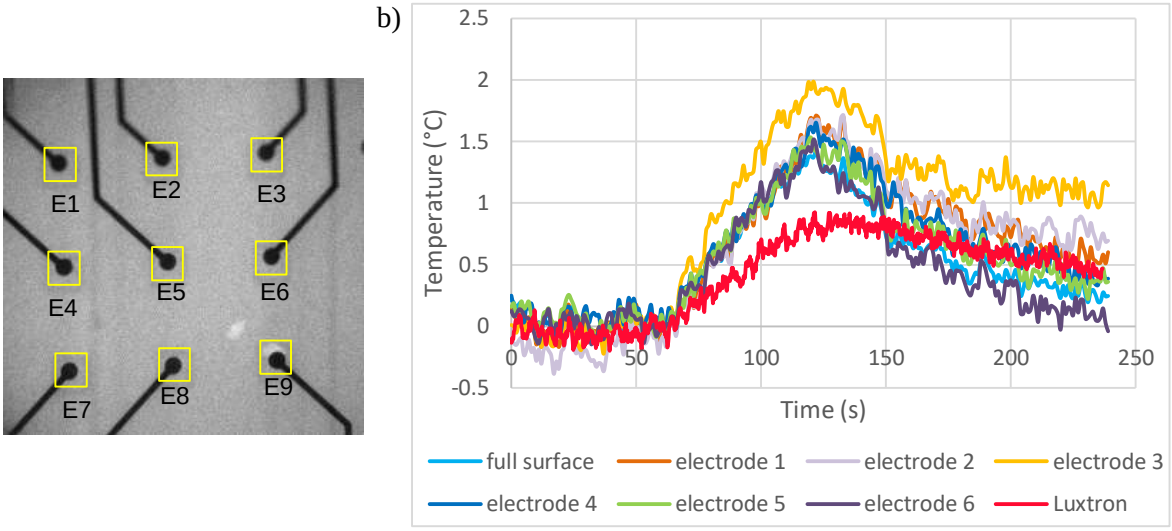


Figure 79 : Fluorescence intensity recorded at the microelectrodes level within MEA-2 (center red dot in Figure 78), a) image recorded by the microscope 20x objective of 9 microelectrodes within MEA-2, b) temperature variation retrieved from the fluorescence intensity compared to the temperature measured directly with the fiber optic probe.

The temperature variation at the rest of the positions of Figure 78 is assessed only with the fiber optic probe. Temperature elevation values presented in Figure 80 are those measured at the four positions of the conducting lines represented by red dots in Figure 78. The temperature curves of Figure 81 are the measurement results at the four positions distant from the metal components (i.e. electrodes and lines) represented by green dots in Figure 78. These temperature values are the outcome of a 20 W power application. Most of the temperature assessments resulted in maximum values between 1 and 1.5 °C whether they were conducted close or far from the conducting lines. The measurements conducted at the right lines area induced higher temperature values displayed in Figure 80a with an average of 3°C indicating an elevated E-field coupling. Except for this value, temperature elevations at the different positions vary within 35 % range at maximum. From these temperature data, the SAR probe results were retrieved.

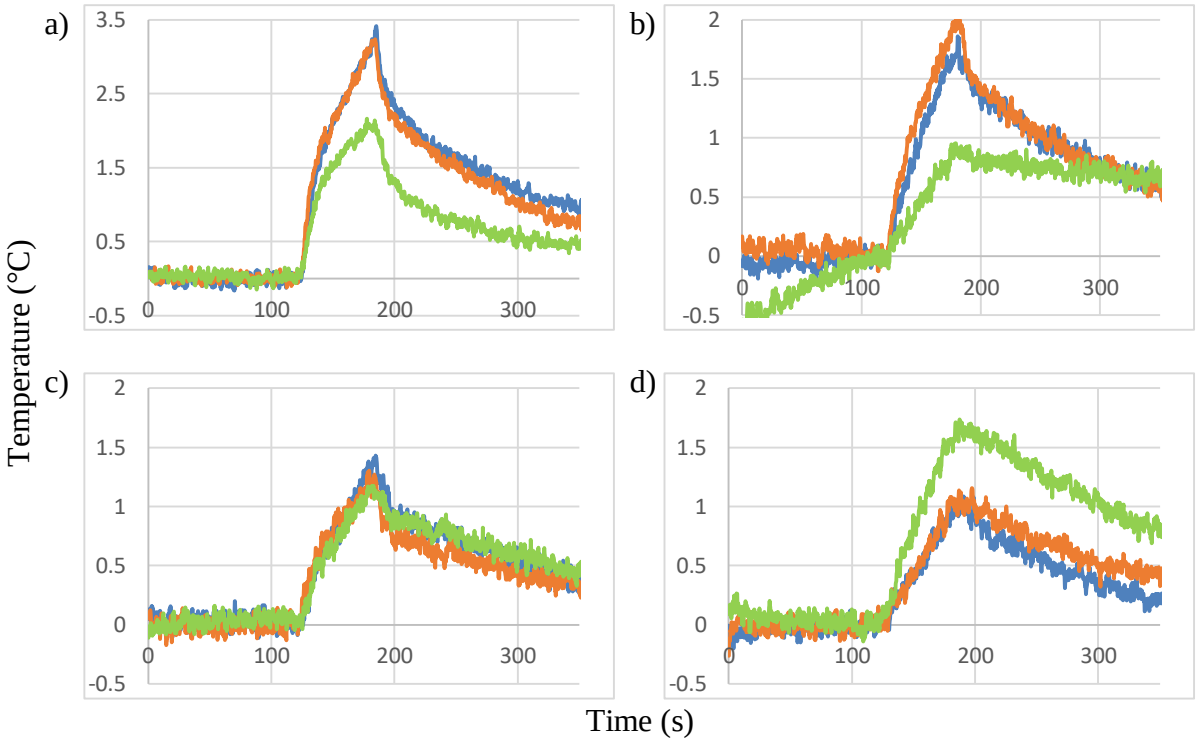


Figure 80 : Temperature elevation measured with the fiber optic probe at the four positions (red dots of Figure 78) where the top conducting lines are located, a) right lines, b) left lines, c) upper lines, d) lower lines.

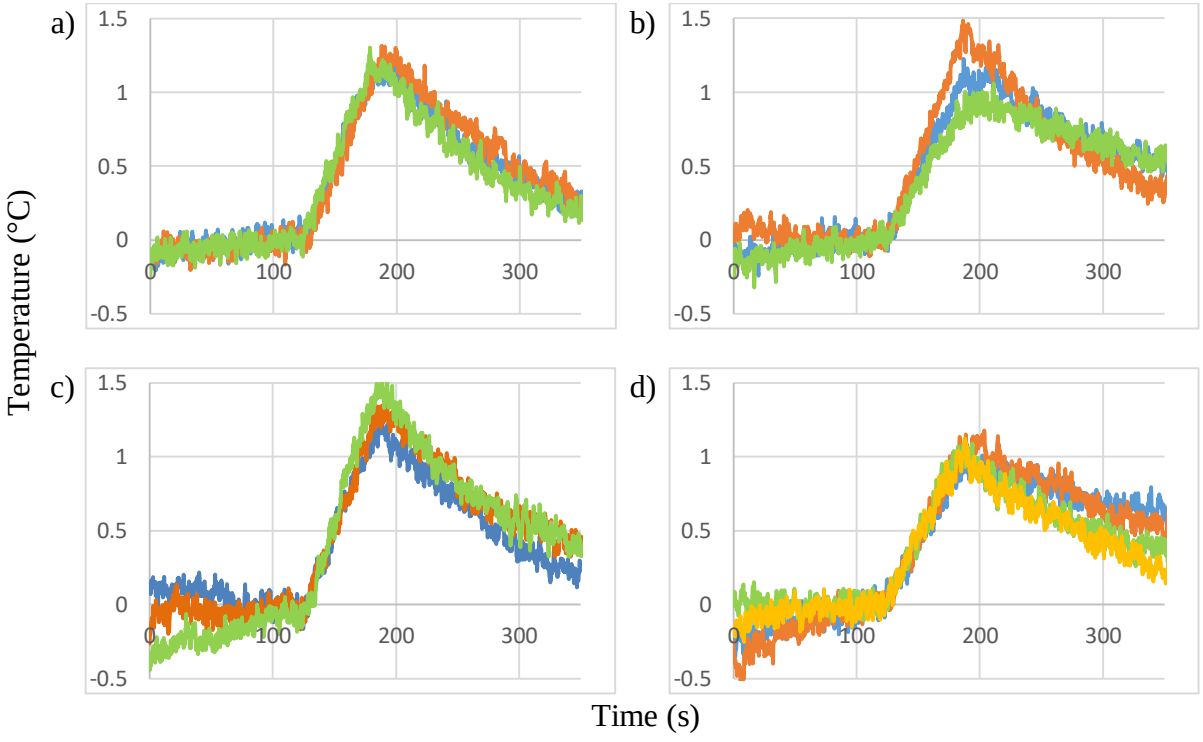


Figure 81 : Temperature elevation measured with the fiber optic probe at the four positions (green dots of Figure 78) distant from the metal micro-components, a) right upper position, b) left upper position, c) right lower position, d) left lower position.

a)

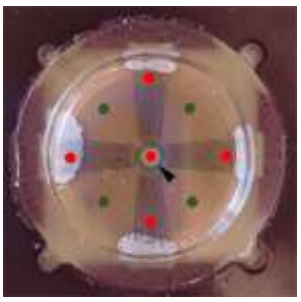

b)

| | | |
|---|---|---|
| 4.93 ± 0.70 | Lines<br>11.32 ± 2.30 | 5.76 ± 0.53 |
| Lines<br>12.55 ± 5.90 | Electrodes<br>3.76 ± 0.74<br>7 ± 1.04 | Lines<br>45 ± 11.60 |
| 5 ± 0.70 | Lines<br>6.13 ± 2.75 | 6.70 ± 1.20 |

Figure 82 : a) Photo of MEA-2 with red and green dots representing the positions where the temperature was recorded, b) experimental SAR values normalized per 1 W incident power obtained by **Rhod-B** fluorescence measurements and **fiber optic probe** recordings.

The SAR retrieved from the microscopic recordings with Rhod-B technique at the microelectrodes level (blue value) and from the macroscopic optic probe measurements at several positions (red values) within MEA-2 are classified within the schematic of Figure 82b. Values are normalized per 1 W incident power. SAR probe values show some spatial inhomogeneity reflecting the inhomogeneity obtained with the temperature data at a few different positions. Since the lowest temperature elevation value was obtained at the microelectrodes area, the lowest SAR value was found as well at the area of the microelectrodes with a value of 3.76 ± 0.74 W/kg from the fiber optic probe measurements. The SAR obtained with Rhod-B technique is higher by about 1.8 folds and it was determined to be 7 ± 1.04 W/kg. Similar to the temperature distribution, the highest SAR probe value is found at the right line position with 45 ± 11.6 W/kg. SAR probe values at the green positions (Figure 82a) are rather homogenous considering the standard deviations.

The experimental evaluation of MEA-1 and MEA-2 showed that the induced temperature at several positions is more elevated within the MEA-1. As the area of interest is where the microelectrodes are located, the temperature obtained with Rhod-B technique at that position within MEA-1 was around 5.4 °C. It represents the highest temperature value within this MEA-1 and it is 6 folds higher than that of MEA-2 at the same position. Unlike the MEA-1 results, the lowest temperature within the MEA-2 is found in the microelectrodes area around 0.85 °C. This outcome difference can be explained by the larger opening of MEA-1 with its bigger size microelectrodes.

Analyzing the SAR outcome from the probe method or the fluorescent dye technique within the two MEAs confirms that MEA-2 is more stable and induces lower thermal effects. The SAR probe values within the MEA-2 is more homogenous than the MEA-1 SAR results. MEA-2 needs to be further investigated by numerical simulations because it is a newer version and it was less used in the electrophysiological studies, unlike MEA-1 that has already been exploited to record neuronal electric activity.

### IV.1.3. Numerical characterization of MEA-2

A numerical microdosimetry was performed to complete MEA-2 characterization. Thereby, it initially was designed with all its components. The simulation was complex because the system contains objects at different scales. For instance, there is a significant size difference between the TEM cell which is a centimetric device (21 × 8.5 × 2.3 cm) and the microelectrodes which are micrometer-sized (30 × 60 µm). Meshing properly the thin lines and the microelectrodes produce an infinite simulation time. Thus, metal components were defined with zero thickness to simplify the model and mesh size was set to 30 × 30 µm grid along the 30 µm electrodes diameter (Figure 83a). That helped gain in simulation time which was still extensively long (102 hours). E-field distribution obtained at 1.8 GHz was showing some discontinuities (see Figure 83b) which indicate the need to enhance the number of meshes around the micro-components. Levels of E-field around the electrodes were extremely high and led to a SAR probe efficiency of 1.74 kW/kg per 1 W incident power which is unrealistic and is incomparable to the experimental SAR probe values obtained. Figure 84b shows the SAR distribution within the medium at the electrodes surface obtained along the horizontal plane cut of Figure 84a. SAR distribution shows high inhomogeneity with extremely high values in some areas. The non-consistent SAR values that heighten around some electrodes and lowers around others indicate its lack of accuracy. Numerous essays and optimization techniques were tested in simulation, but the results of E-field and SAR were incomparable with the experimental ones. Thus, to resolve this issue, the system modeling was further optimized or simplified.

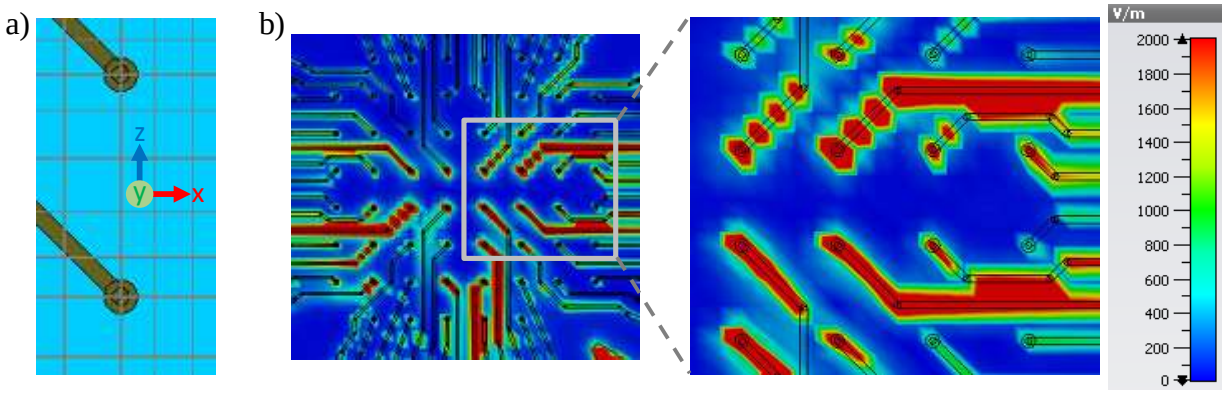


Figure 83 : Simulation of MEA-2 within the TEM cell, a) electrodes surface meshing, b) E-field distribution at 1.8 GHz at the surface of the electrodes with a close-up image.

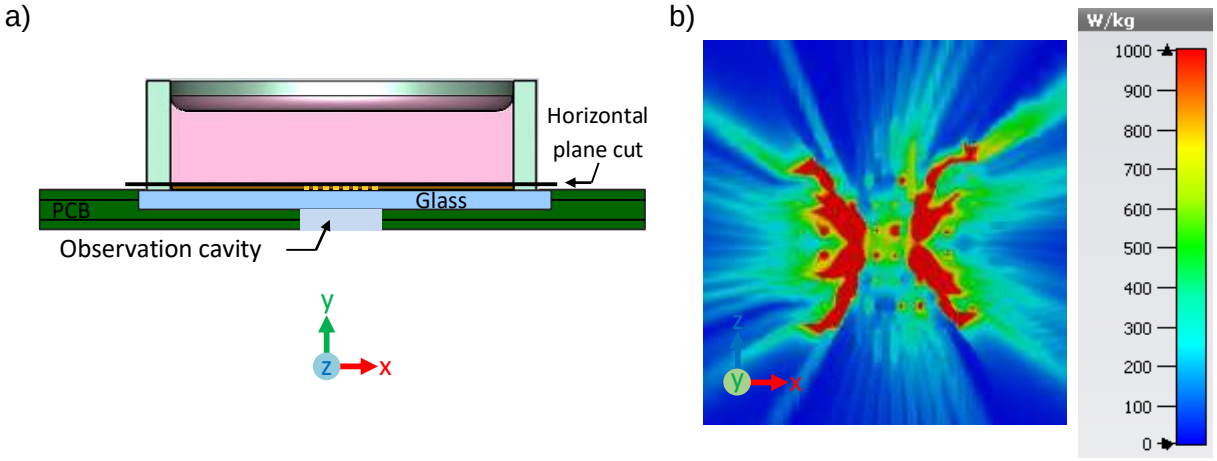


Figure 84 : SAR spatial distribution within 1 ml culture medium at 1.8 GHz, a) horizontal cut at the contact surface between the medium and the electrodes, b) SAR distribution at the microelectrodes area.

## IV.1.4. TEM cell modification

To be able to improve the numerical spatial resolution of the MEA, we needed to reduce the number of meshes assigned to the non-essential area like the space surrounding the TEM cell. Thus, the simulation box size (26 × 13.5 × 7.3 cm) was reduced to the minimum possible (22 × 9.5 × 3.3 cm). However, the gained meshes were not sufficient because the issues observed with the E-field and the SAR results remained and were not solved.

### IV.1.4.1. PML boundaries

A simulation technique used to simplify the TEM cell design consists of cutting out the device before the output and placing absorbents or perfect matching layer (PML) boundary

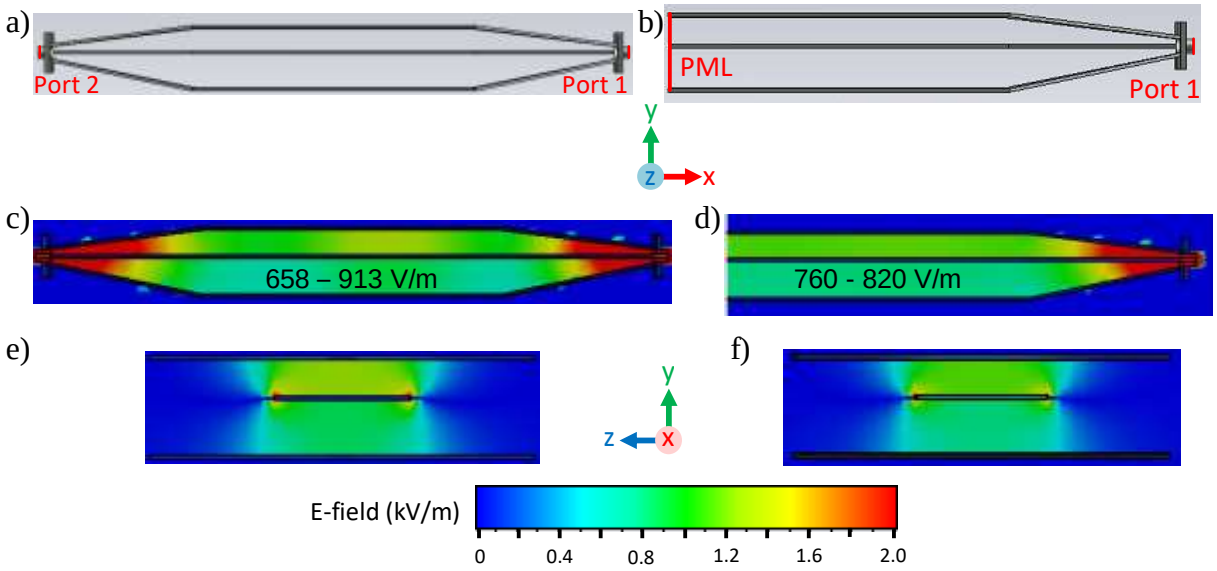


Figure 85 : Design of TEM cell and the numerical E-field results at 1.8 GHz, a) full TEM cell design, b) TEM cell with PML boundary at the output, (c,d) longitudinal cut of the E-field spatial distribution, (e,f) transversal cut of the E-field spatial distribution.

(Figure 85b). A PML boundary extends the geometry virtually to infinity and waves can then propagate with minimal reflections. Thereafter, the TEM cell output tapers and connectors were deleted and replaced with the PML boundary as shown in Figure 85b. Figure 85 shows the difference between the full design of the TEM cell and the modified one in terms of design and E-field distribution results. The longitudinal and the transversal cuts displaying the E-field distribution (Figure 85d, f) at 1.8 GHz show similar results as the TEM cell before modification (Figure 85c, e). PML boundary eliminated the wave reflection thus, the E-field between the septum and the lower plate shows better homogeneity with intensity within 760 – 820 V/m range compared to that within the full TEM cell that varies between 658 – 913 V/m. These modifications decreased the simulation box size hence, diminishing the mesh number from 312180 with the complete TEM cell structure to 192510 mesh using the PML boundary.

### IV.1.4.2. Output waveguide port

Instead of using the PML boundary, a waveguide port was defined and tested at the TEM cell output. Figure 86 illustrates the design of the TEM cell and the E-field distribution obtained associated with this modification. The E-field variation with a normal waveguide port is similar to that obtained with the PML boundary with slightly better homogeneity and levels

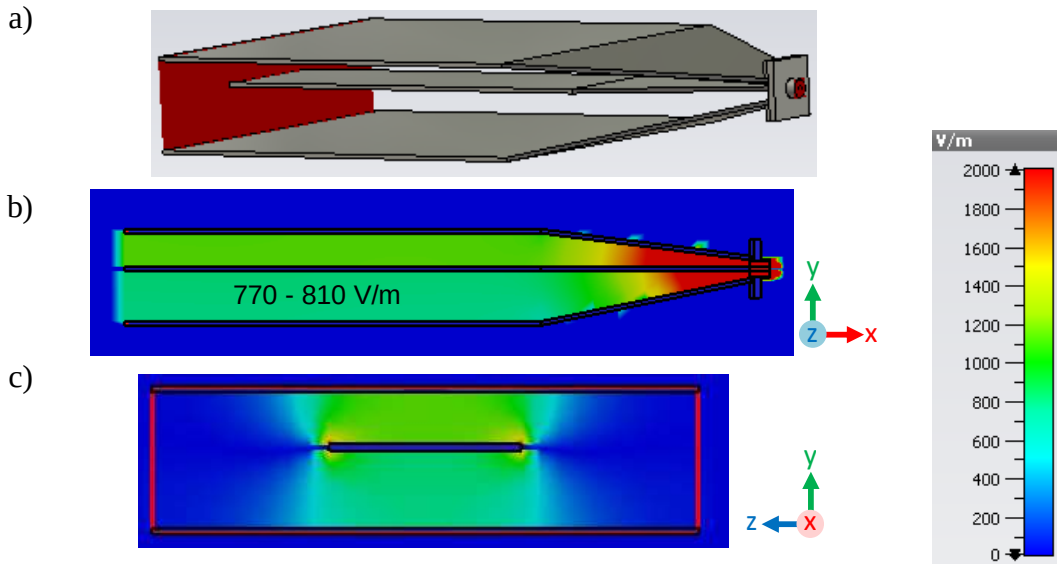


Figure 86 : Design of the TEM cell, a) with a waveguide output port defined at the end of the plates, associated with the E-field spatial distribution at 1.8 GHz, b) longitudinal and c) transversal cut.

between 770 – 810 V/m. These E-field investigations show that the output waveguide port and the PML boundary operate similarly.

### IV.1.4.3. Input and output waveguide ports

Even though the modifications made helped to reduce the mesh number of the simulated structure, additional modifications were made to the TEM cell to further reduce these parameters. The input connector and tapers were deleted as well and replaced with a waveguide input port placed directly at the plates extremity. Only the septum and the reference plates were kept from the TEM cell initial design. Figure 87a schematizes the input and output ports of the tri-plates TEM cell. The E-field distribution at 1.8 GHz was obtained as shown in Figure 87b and c. In this case, the numerical assessments show a remarkable decrease of the E-field intensity from 770 – 810 V/m (Figure 86b) to about half by 360 – 440 V/m. Changing the device's input modified completely the intensity of the transferred energy. We aimed to simplify as possible the exposure device without changing the E-field propagating inside.

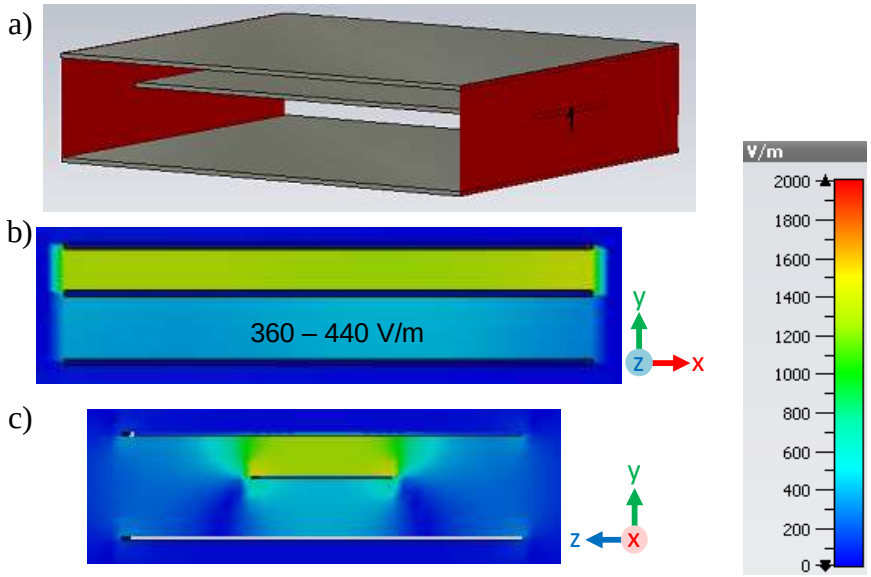


Figure 87 : a) Design of the tri-plates TEM cell with two waveguide ports defined at the extremities of the plates, associated with the E-field spatial distribution at 1.8 GHz, b) longitudinal and c) transversal cuts.

Modifying the design of the TEM cell exposure device helped reduce the total mesh number used in simulations. Deleting the output components (i.e. tapers and connector) and ending the structure with a waveguide output port or a PML boundary represent suitable approaches to use as they improved the E-field homogeneity and maintained the same E-field intensity levels. However, the simulations showed that the input components are essential for the power excitation within the exposure device and replacing them with an input waveguide port perturbs the E-field level between the TEM cell plates. For these reasons, the design of the TEM cell with the output waveguide port is selected to be used for the investigation of the MEA-2 as it offers the best E-field homogeneity.

#### IV.1.4.4. TEM cell and MEA-2

The MEA-2 was added without any simplifications to the TEM cell modified only at its output as pictured in Figure 88a. The simulation of the MEA-2 with the modified TEM cell lasted about 60 hours instead of 102 hours the time of the simulation of the MEA-2 with the full TEM cell. Figure 88b depicts the variation of the E-field normal component within the MEA-2 at the surface of the microelectrodes. The inset illustrates the field variation at the vicinity of the electrodes. The intensity is rather high and changes rapidly and shows some inhomogeneity.

a)

b)

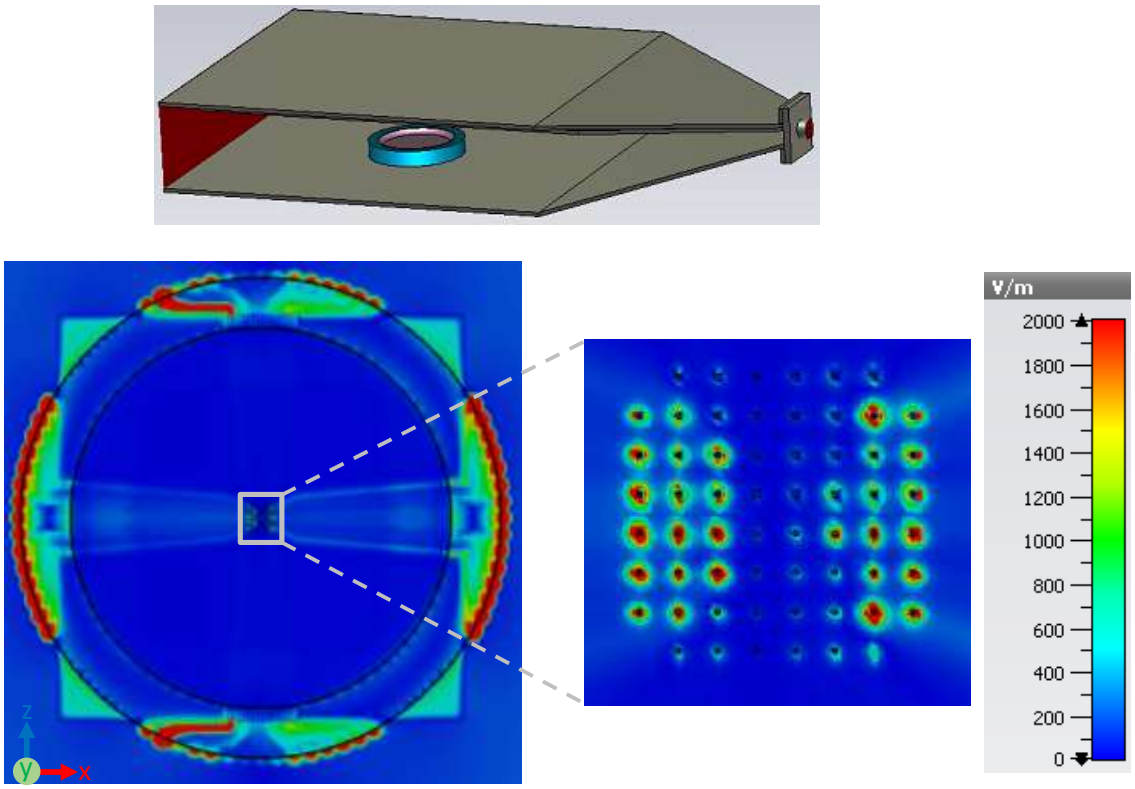


Figure 88 : a) design of the TEM cell and the MEA-2, b) En field spatial distribution at the surface of MEA-2 microelectrodes at 1.8 GHz, zoom on the E-field variation in the vicinity of the electrodes.

SAR spatial distribution was retrieved as well as shown in Figure 89. The horizontal plane cut is positioned at 0.1 mm above the microelectrodes surface and the vertical plane cut is made at the center of the culture medium. SAR values are extremely elevated in the center on top of the electrodes. Indeed, the SAR probe averaged over 1 $mm^3$ cubic volume was calculated to be 417 W/kg normalized per 1 W. The MEA-2 experimental SAR probe was determined in section III.1.4 of chapter 2 to be 6.4 W/kg that makes the numerical value higher by 65 folds. These results prove that the characterization of the MEA-2 cannot be accurately achieved with this TEM cell due to the difference in their dimensions scale.

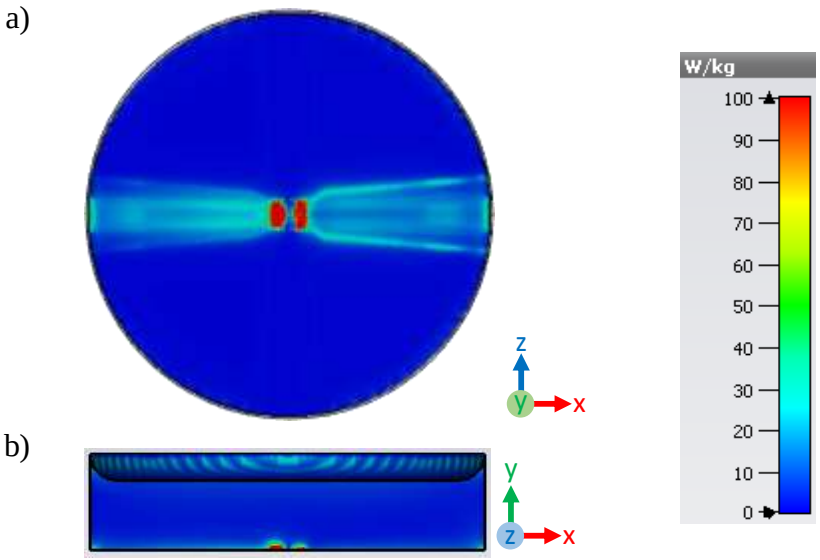


Figure 89 : SAR spatial distribution of the 1 ml culture medium within MEA-2, a) horizontal and b) vertical cuts.

The mesh number optimizations achieved by modifying the TEM cell structure reduced the simulation time but were not enough to obtain accurate E-field and SAR results within the MEA-2. The disparity between the TEM cell and the MEA-2 size scales is the major issue, hence, another approach was tested based on reducing the TEM cell size.

### IV.1.5. Compact TEM cell

An alternative strategy that is based on changing the scale of the exposure system was further implemented. Simulation time using the time domain solver depends not only on the number of meshes but also on their size. The smaller they are, the longer their simulation time. Furthermore, for better resolution, micro-components especially the microelectrodes require fine meshing. The exposure and the recording devices should be designed on the same scale so the disparity of mesh sizes can be eliminated.

For this reason, the TEM cell was the device that needed to be modified. The TEM cell size was reduced to help estimate the electrodes response to the E-field as well as the energy absorbed by the biological medium. The dimensions of the compact TEM cell are presented in Table 11 and the design is shown in Figure 90. The output connector of the compact TEM cell was also replaced by an output waveguide port. Developing a TEM cell at the microscopic scale can help to optimize the MEA's spatial resolution and then relatively quantify the E-field and

the SAR variations. The model was designed to ensure the impedance match at the operating frequency of 1.8 GHz.

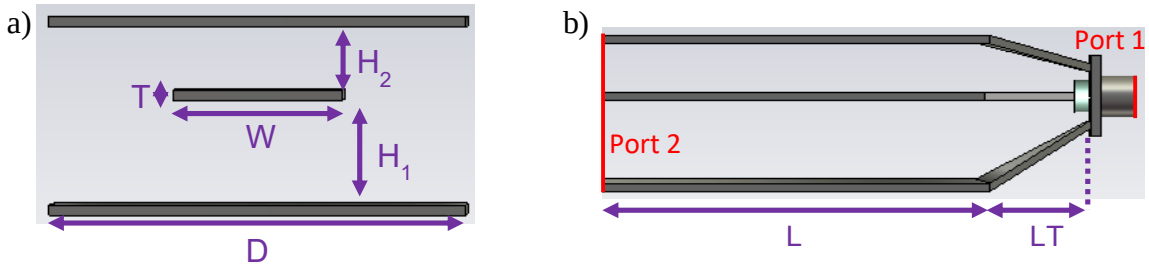


Figure 90 : Numerical design of the compact TEM cell, a) transversal and b) longitudinal plane cuts.

| Dimensions | W | T | H1 | H2 | D | L | LT |
|---|---|---|---|---|---|---|---|
| mm | 3 | 0.1 | 0.97 | 0.8 | 9 | 7.5 | 1.05 |

Table 11 : Dimensions of the compact TEM cell exposure device design.

The distance between the septum and the lower plate was reduced from 12 mm to 970 µm leading to a ratio of 12.4. Figure 91 illustrates the E-field distribution at 1.8 GHz within the compact TEM cell. The intensity between the septum and the lower plate was retrieved to be 9410 V/m. A 12 ratio is obtained when comparing this E-field range values (9340 – 9490 V/m) with the one (770 – 810 V/m) obtained for the real sized TEM cell. This is consistent with the 12.4 ratio on the dimensions.

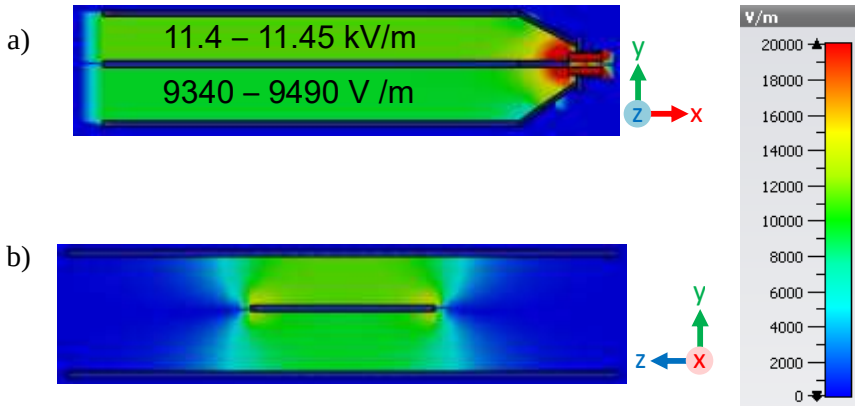


Figure 91 : E-field distribution at 1.8 GHz of the truncated micro-TEM cell, a) longitudinal plane cut, b) transversal plane cut.

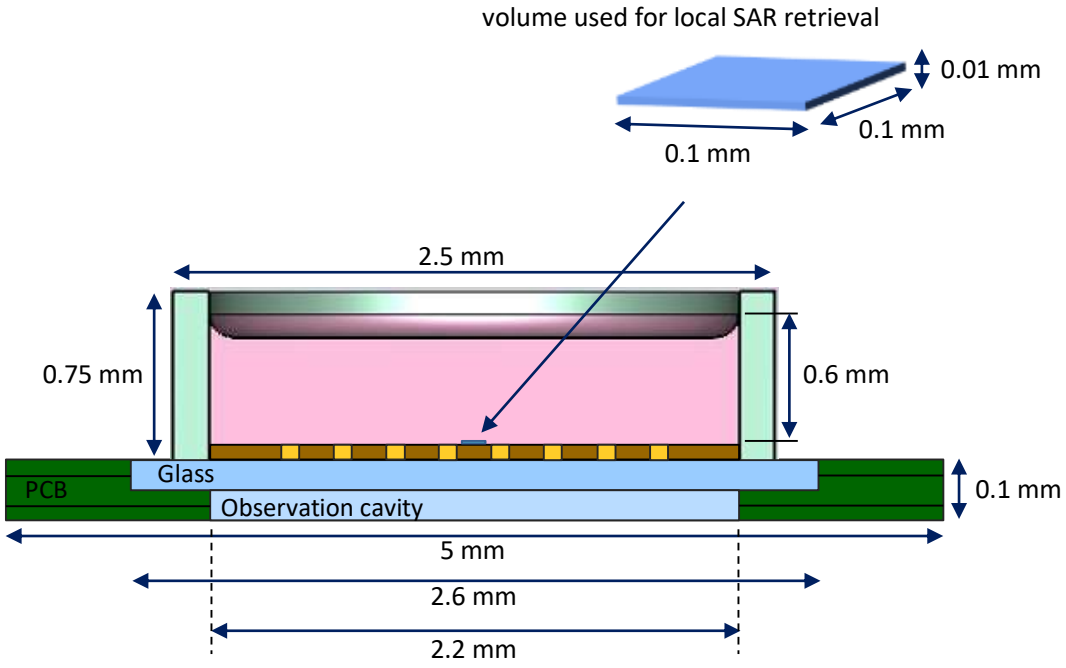


Figure 92 : Numerical design of MEA-2 with smaller dimensions fitting the compact TEM cell and an inset showing the microscopic SAR volume.

For MEA insertion, an aperture of 2.5 mm diameter was created on the compact TEM cell. A few changes were conducted as well on the MEA-2 components' size to fit into the compact TEM cell (see Figure 92). The inner diameter of the culture chamber was fixed at 2.2 mm and its height at 0.75 mm. A 5 × 5 mm PCB was defined with 0.1 mm thickness and the observation cavity diameter was reduced to 2.2 mm. In this version, microelectrodes were designed with their real dimensions (30 µm diameter, 50 µm thickness) and were finely meshed with a 2.4 µm × 2.6 µm grid along the electrodes diameter and 10 µm along the thickness as shown in Figure 93. The four metal reference planes were included within the PCB with no thickness. To keep the design simple, the conducting lines were not modeled. Electric properties of the MEA's components were kept as described in chapter 2. The metal components are defined as PEC and the properties of the non-metal components are defined in Table 12. Based on the dimensions of the culture chamber aforementioned, the culture medium added corresponds to a quantity of 1.9 µL, meshed with a uniform 10 $\mu m^3$ spatial grid.

| | Conductivity (S/m) | Relative permeability | Volume density ($kg/m^3$) |
|---|---|---|---|
| Biological medium | 2.3 | 74.2 | 1000 |
| Culture chamber<br>Glass chip<br>Observation cavity (MEA-2) | - | 4.6 | 2230 |
| PCB | - | 4.4 | 1850 |

Table 12 : Electric properties used in simulations of the MEAs components at 1.8 GHz.

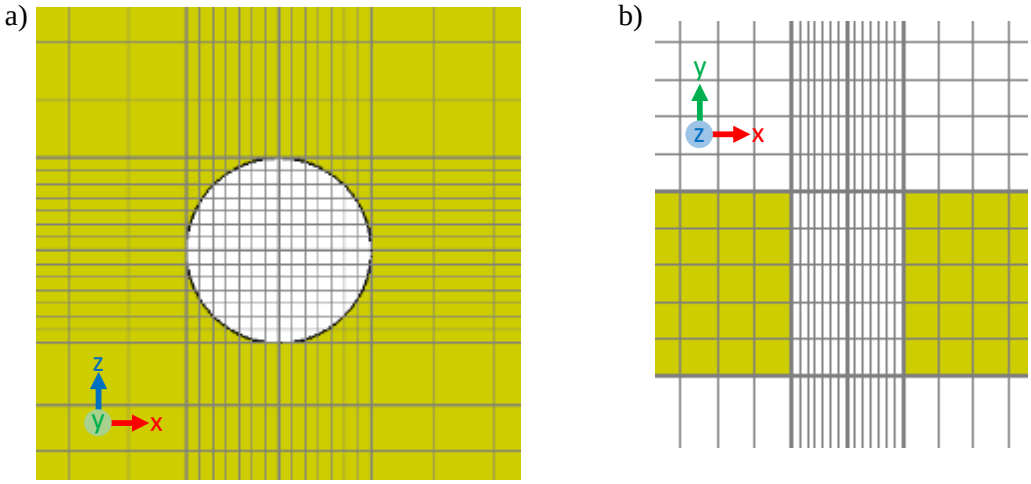


Figure 93 : The microelectrodes meshing, a) mesh-size at the surface of an electrode, b) vertical cut showing the meshing along the electrode height.

Results are displayed in Figure 94. They include the E-field spatial distribution at the surface of the microelectrodes displayed in Figure 94a, the SAR distribution within the culture medium with a horizontal cut at 10 µm above the electrodes surface (Figure 94b) and a vertical cut along the electrodes (Figure 94c). The field coupling is rather low at the surface of the electrodes with an homogenous distribution between the electrodes. The field gradually increases at the internal periphery of the culture chamber. SAR is rather homogenous along the medium height and at the electrodes level. A microscopic SAR value was computed at the center of the MEA-2 (inset of Figure 92) within a volume of 100 $\mu m^2$ surface and 10 µm thickness representative of the cells layer. The local SAR efficiency was determined to be 1.2 W/kg per 1 W incident power between the electrodes where neurons are typically located.

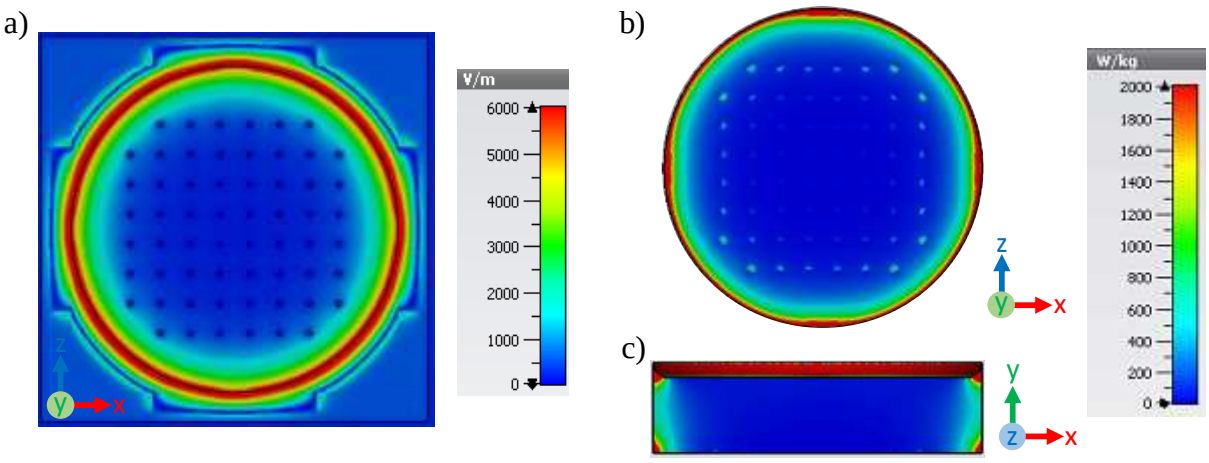


Figure 94 : Simulation results of the compact TEM cell with the MEA-2 without conductor lines at 1,8 GHz, a) E-field distribution at the surface of the microelectrodes, SAR distribution within the 1.9 µL culture medium, b) horizontal cut at 10 µm above the electrodes surface and c) a vertical cut along the electrodes.

To complete the MEA design, top conductor lines were added in the modeling with 30 µm thickness. Spatial distribution of E-field within the culture chamber at the electrodes surface is presented in Figure 95 with a zoom on some electrodes. The insertion of the top lines induced an increase of the E-field intensities at the surface of each electrode varying between 2200 and 4000 V/m. Using the 12 ratio, E-field intensity can be converted to estimate the values within a normal-sized TEM cell and MEA. Hence, the E-field at the surface of the electrodes would be approximatively between 183 and 333 V/m.

Even though lines are covered with the insulator layer the E-field's intensity at the lines level can be observed indicating that the coupling occurred with the transmitted wave led to a coupling between lines and electrodes. The E-field intensities in the areas between the microelectrodes and lines are homogenous with rather low values around 400 V/m. Hence, the intensity within the real size TEM cell was estimated to be 33 V/m. Comparing to the first MEA-2 simulations, these results agree with that of experimental analysis in terms of homogeneity. SAR distribution within the MEA is also homogenous between the electrodes as observed in Figure 96. The horizontal cut (Figure 96a) shows red spots where values are enhanced due to the presence of electrodes. The SAR increases within an area of approximately 70 µm diameter around each electrode. Local SAR retrieved between the electrodes (Figure 96c) within 100 $\mu m^2$ surface and 10 µm thickness is about 8.55 W/kg/W. With the same volume

but around an electrode (Figure 96c) the SAR becomes about 2402.4 W/kg/W which is much higher than the value obtained between the electrodes.

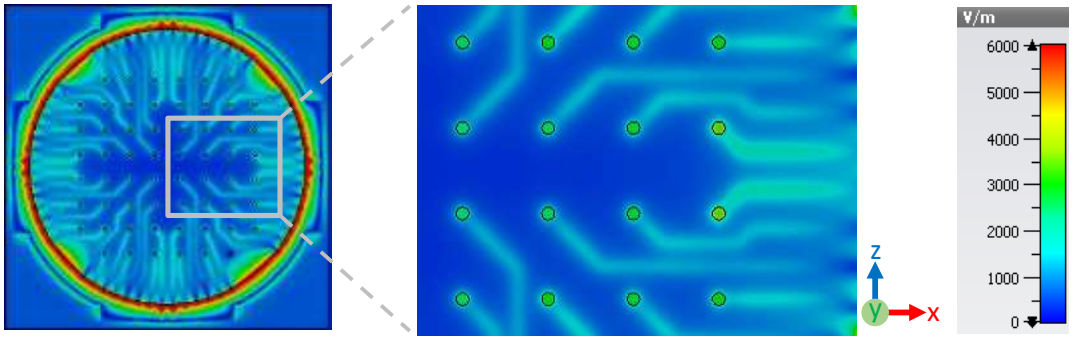


Figure 95 : E-field spatial distribution within MEA-2 at the electrodes surface, a close-up on the E-field in the vicinity of electrodes and lines.

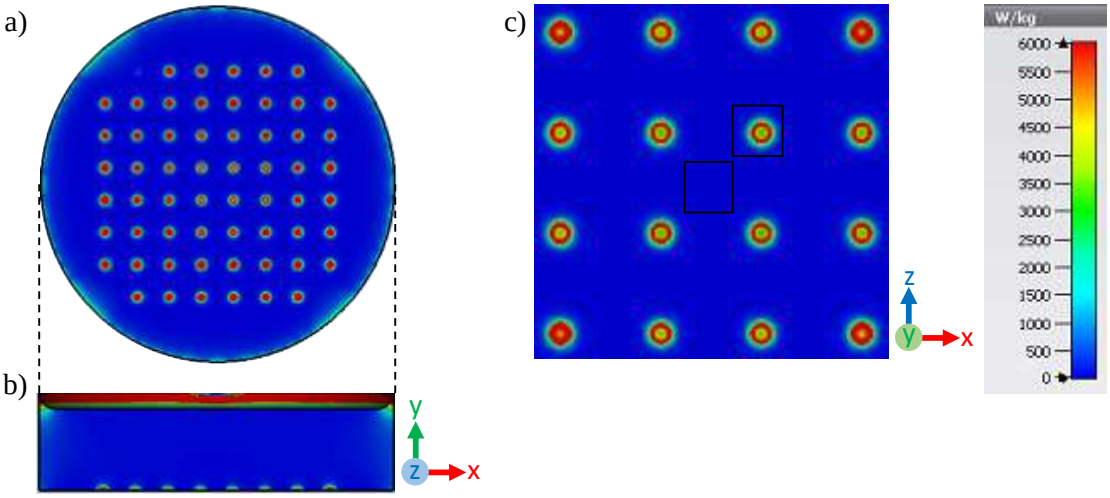


Figure 96 : SAR spatial distribution at 1.8 GHz within the 1.9 µl culture medium inside the compact TEM cell and MEA-2, a) horizontal cut 10 µm above the surface of the electrodes and b) a transversal cut at the electrodes level, c) positions of SAR retrieve between the electrodes and around an electrode.

To estimate the SAR value in the case of real size devices, the 12 ratio determined previously between the E-field intensities can be used. SAR values depend on the squared modulus of the E-field, thus, the ratio should be the square value of 12 which is 144. As a result, the local microscopic SAR can be estimated by dividing the 8.55 W/kg value by the 144 ratio to obtain approximately 0.06 W/kg. Also, the SAR around the electrode can be determined from the 2402.4 value to obtain 17 W/kg.

| Height | Numerical local SAR (W/kg) | Estimated local SAR after the division with the 144 ratio |
|---|---|---|
| 10 µm | 1035.73 | 7.19 |
| 8 µm | 1170.24 | 8.13 |
| 6 µm | 1348.14 | 9.36 |
| 4 µm | 1602.44 | 11.13 |
| 2 µm | 2040.43 | 14.17 |

Table 13 : Numerical local SAR retrieved within 0.65 × 0.65 mm² surface and several thicknesses providing the values within the compact system and the estimated ones for the real-sized system.

The experimental fluorescence intensity is recorded with the camera on a thin thickness that is not determined. Thus, other numerical local SAR values were retrieved within a larger surface of 0.65 × 0.65 mm² which corresponds to the acquisition window of the microscope camera at different heights between 2 and 10 µm. The local SAR values assessed from the simulation of the compact TEM cell and the ones estimated with the 144 ratio are displayed in Table 13. The final estimated local SAR values are comparable with the experimental SAR value obtained with the Rhod-B technique (7 ± 1.04 W/kg). The main noticeable difference between the experimental and the numerical results is that fluorescence measurements showed that the temperature elevation is highly homogenous even near the electrodes. However, the SAR distribution showed variations at the electrodes level.

The amount of culture medium used in simulation was 1.9 µL instead of the 1 mL used in experiments. It is known that SAR values increase with the biological medium quantity. Besides, other factors should be considered to explain the differences as the size of the culture chamber or other details of MEA-2 that were not included in this design.

## IV.2. Drop of medium on a glass slide

In the previous experiments, Rhod-B technique was evaluated with liquid culture medium of few milliliters. However, certain microsystems operate with microliter quantities hence, the efficiency of Rhod-B was investigated with small microliter samples. These tests aim to further optimize the setup settings and the dye usage for the next experiments with microsystems. Figure 97 shows the experimental setup used to apply the RF signal and to detect

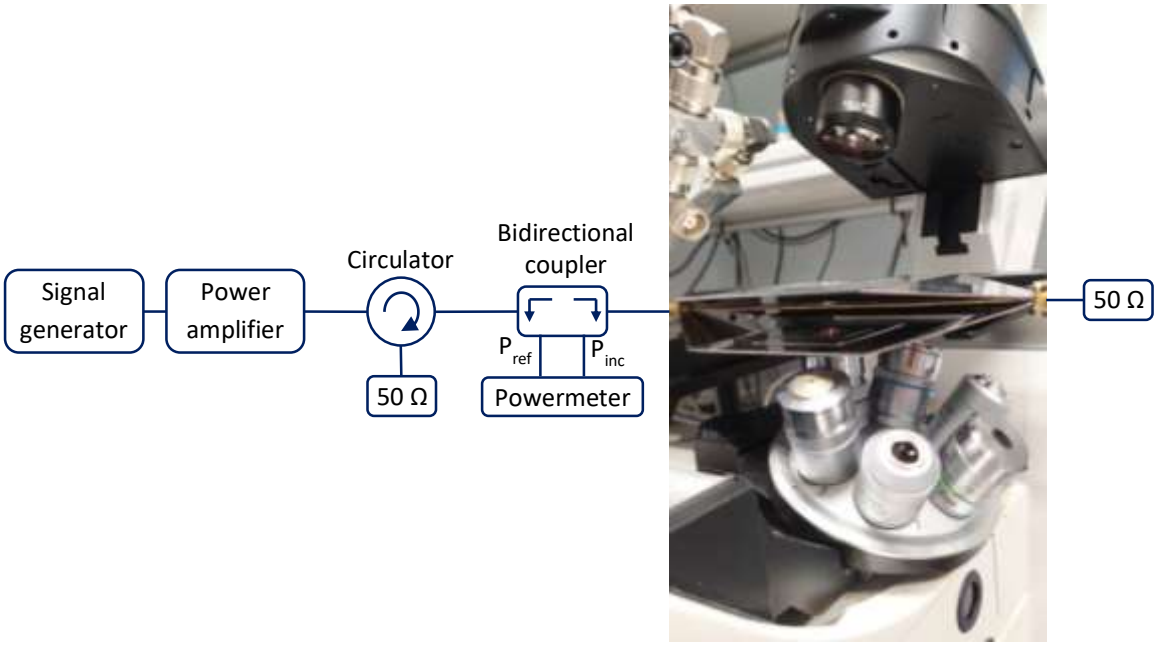


Figure 97 : Experimental setup used for the assessment of the Rhod-B fluorescence intensity within the 37 µl drop on top of a glass slide inside the TEM cell.

the fluorescence intensity of Rhod-B. A small amount of 37 µl of HBSS labeled with 50 µM of the fluorescent dye was placed on a glass slide within the TEM cell exposure device. This quantity of medium is small but can be detectable with the microscope camera. It is also used as an intermediate step between the milliliter quantities and microliter quantities. The TEM cell is set on the microscope stage for real-time fluorescence measurements.

The CW signal was applied at 1.8 GHz with several incident power i.e. 10 W, 20 W and 25 W for a duration of 30 s. Fluorescence intensity was recorded by 20x objective with 1 record/s sampling rate. No temperature measurements with the optic fiber probe were conducted due to the small quantity of the biological solution.

Fluorescence intensity detected at each experiment was converted to temperature variation. The fluorescence intensity recorded with the microscope camera was converted to temperature with the first-degree equation defined in chapter 2. The change of temperature obtained from 3 incident powers are plotted in Figure 98. Exposure starts at 300 s (RF generator ON). From this instant, no particular steep variation was observed related to the RF application. Even with high incident power like 25 W, the temperature varies only slightly within the drop.

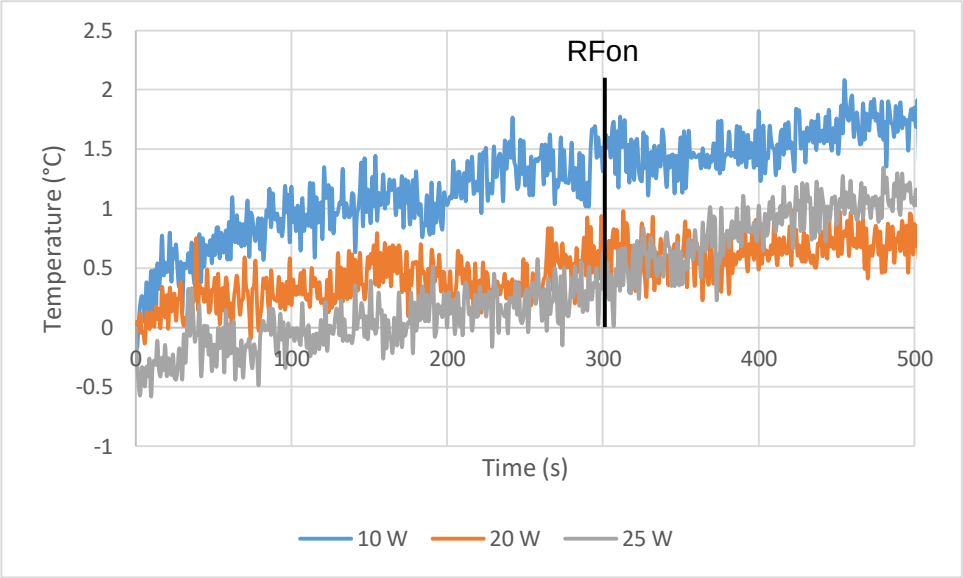


Figure 98 : Temperature elevation retrieved from the fluorescence intensity recorded from a drop of HBSS medium mixed with Rhod-B on top of a glass slide while applying CW signal.

Therefore, to evaluate the electric field and the SAR values, numerical simulation of the real sized TEM cell with a 37 µl drop on a glass slide was conducted with a 3D electromagnetic software based on the FDTD method. Figure 99 presents the 3D design of the medium drop, the glass slide, the TEM cell and the microscope objective. The numerical SAR variation is evaluated in function of the working distance illustrated in Figure 100. It represents the distance between the glass slide and the microscope objective. The design is meshed with a uniform 0.1 $mm^3$ spatial grid.

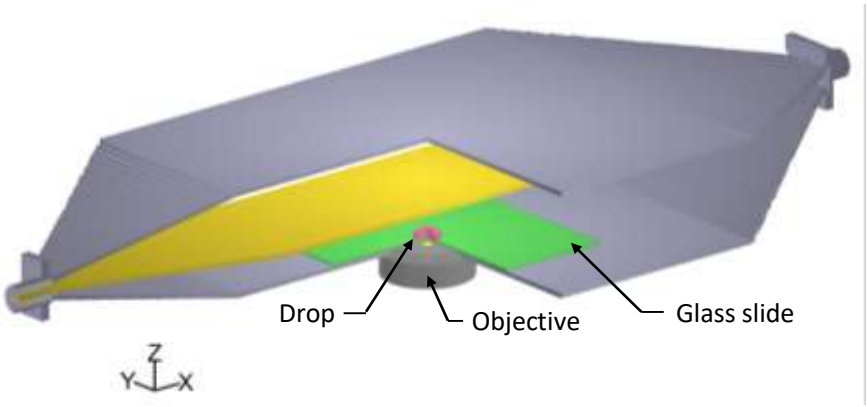


Figure 99 : A 3D design of the 37 µl drop on a glass slide inside the TEM cell with the objective.

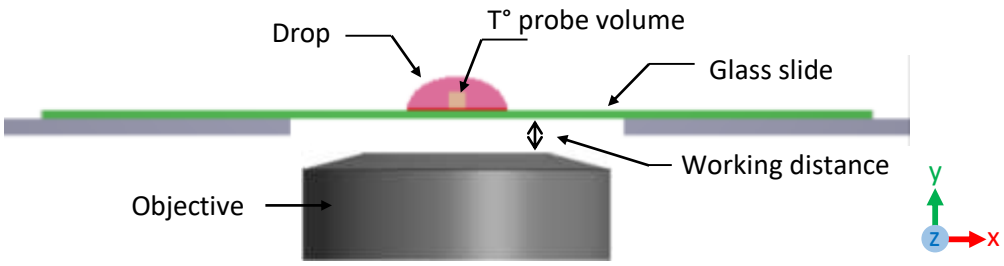


Figure 100 : A cross section of the drop within the TEM cell showing the working distance between the glass slide and the microscope objective.

Figure 101a displays the SAR distribution at 1.8 GHz along a transversal cut at the center of the drop while the working distance is set at 200 µm. The SAR map shows some inhomogeneity along the vertical cut. A gradual increase of SAR efficiencies is seen from the drop center toward the surface. The non-uniformity of SAR along the vertical cut is not a particular concern since the fluorescence measurement area is located at the bottom of the drop. The SAR distribution at the bottom is rather homogenous.

The variation of SAR values versus the working distance of the microscope is plotted in Figure 101b and are normalized per 1 W incident power. The whole volume SAR, bottom layer SAR and SAR probe represent the SAR values averaged over the whole volume of the drop (~ 37 $mm^3$), the bottom layer with a 100 µm thickness (~ 2.8 $mm^3$) and the probe measuring volume (~ 1 $mm^3$), respectively. The SAR was assessed for several working distance values from zero to 700 µm with 100 µm step size. SAR volume and bottom SAR decreased with the increase of the working distance and their variation is more remarkable from 0 to 100 µm working distance. The SAR probe slightly varies with the working distance. For a 200 µm working distance, the simulated SAR values obtained are 0.51 W/kg, 0.5 W/kg and 0.36 W/kg for the whole volume, bottom layer and probe, respectively.

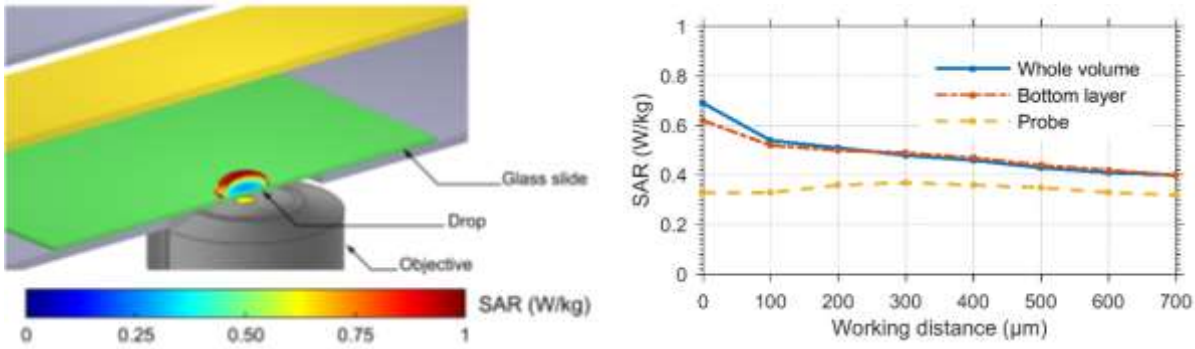


Figure 101 : Design of the 37 µL drop on the glass slide within the TEM cell. A) transversal cut of SAR spatial distribution with 200 µm distance from the objective, b) effect of the working distance on the SAR values [167].

The experimental measurements conducted with the drop of medium mixed with Rhod-B did not allow the evaluation of the fluorescence intensity variation as no significant change was recorded. However, the numerical assessments showed the variation of SAR across the drop as well as its variation versus the objective working distance. Within the area of interest that corresponds to the bottom layer of the medium, the SAR does not vary significantly and it is rather homogenous.

The next part describes a microsystem and its experimental evaluation obtained with the Rhod-B technique along the numerical assessments.

## IV.3. Microfluidic channel chip

The Rhod-B technique was applied with a microfluidic channel. This exposure device detailed in Figure 102 consists of a coplanar waveguide (CPW) with two microfluidic channels. The chip was fabricated by standard photolithography. On top of a 500 µm thick silica substrate (Figure 103), three gold electrodes were deposited with 2 µm thickness and 130 µm gap. A layer of 50 µm of polymer covers the electrodes surface. This exposure chip was designed to match 50 Ω when the microchannels are filled with the biological medium. The chip was then fixed to a PCB to ensure rigidity and avoid damaging the chip. The PCB was designed so the microfluidic exposure device fits within the microscope stage. Two SMA connectors are attached to the PCB to allow the connection to the experimental setup. A copper coplanar waveguide was created at each extremity of the chip as a transition between the microelectrodes

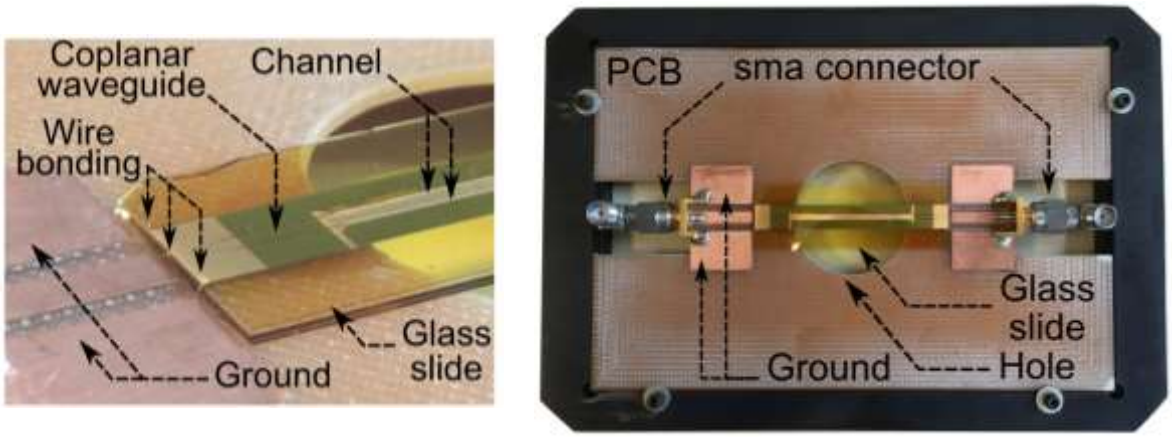


Figure 102 : Detailed photographs of the microfluidic microsystem based on CPW electrodes mounted on a PCB designed to be inserted on the microscope stage [167].

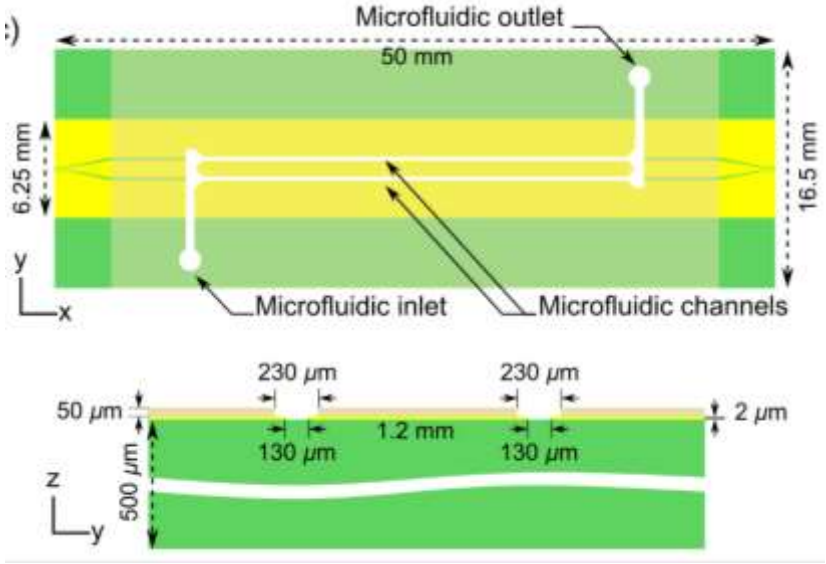


Figure 103: Numerical design of the microfluidic microsystem with its dimensions [167].

and the SMA connectors. The microelectrodes are connected to both CPWs through wire bondings.

An experimental frequency evaluation of the microfluidic channel chip was performed with a VNA with the channels empty or filled with the medium. The return loss $S_{11}$ recorded showed in Figure 104 proves the good impedance matching of the system. The medium did not cause significant field perturbation since values remained under -10 dB meaning that only 10 % of the incident power is reflected at the SMA input port. At 1.8 GHz, the transmission $S_{21}$ is

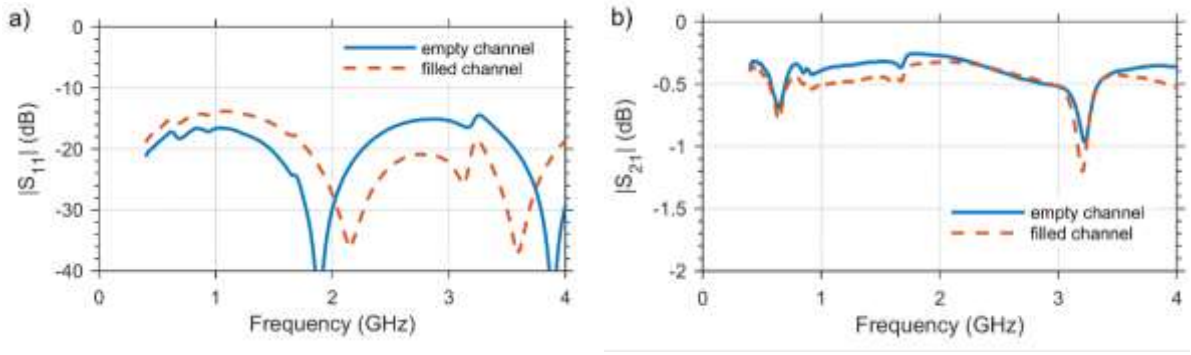


Figure 104 : S-Parameters of the microfluidic microsystem; the microfluidic channel is empty or filled with the biological sample, i.e., a drop of HBSS, (a) Reflection ($S_{11}$) coefficient, (b) Transmission ($S_{21}$) coefficient.

between 0 and -0.5 dB which confirms the good energy transfer as it informs that a minimum of 90 % of the incident power is transmitted to the biological sample.

The microchannel dosimetry was carried out in static conditions. Drops of HBSS labeled with Rhod-B were dropped into the microchannels and to prevent the evaporation of the liquid during the experiment, a cover glass was placed on top. The medium prepared had a concentration of 100 µM of Rhod-B dye and was exposed to a CW signal at 1.8 GHz. The incident powers applied measured at the power amplifier output were 0.1 and 0.2 W for a duration of 30 s. The recording of the fluorescence intensity was complex. A successful recording was only obtained when 5% of the microscope incident beam was applied for 5 ms. Above that percentage, the fluorescence intensity was continuously decreasing and did not reflect any effect of the RF application probably due to the photobleaching of the Rhod-B dye.

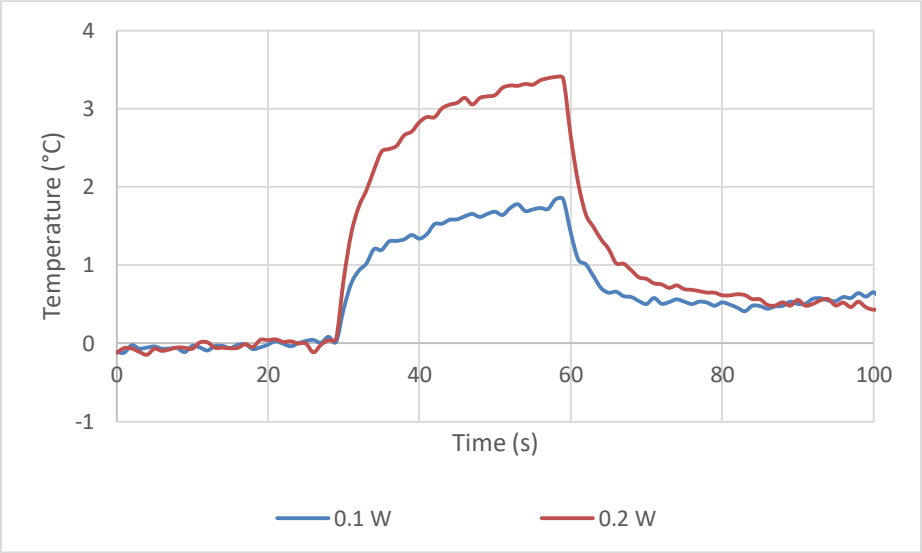


Figure 105 : Temperature change obtained from RhodB fluorescence intensity within the microfluidic channel containing a drop of HBSS with 100-µm Rhod-B. The microsystem is exposed at 1.8 GHz to 0.1 and 0.2 W incident power for 30 s.

Temperature variation was retrieved from the measured Rhod-B fluorescence intensity with the conversion coefficient determined in chapter 2 that was $\alpha = -57$. Curves plotted in Figure 105 represent the change in temperature in the drop filling the microchannels during RF signal application. A rise of about 17°C per incident power was detected and the local SAR per 1W incident power was computed from these data to be 14.5 kW/kg.

Other measurements were conducted to assess the impact of a two consecutive application of RF signal on the same sample within the microchannels. The EMF was applied following the time slots of Figure 106. After the first 30 s exposure, fluorescence was recorded for the following 3 minutes with no RF exposure to ensure the quenching of the sample and the return of the fluorescence to the initial value, then another 30 s exposure was applied with the same power level. Figure 107 displays the Rhod-B fluorescence intensity recorded while applying 0.2 W for 30 s twice. During the first field application (RFon at 94 s), the fluorescence lowers from the beginning of the exposure while the medium temperature increases then it returns to its initial value. Before the start of the second application (RFon at 304 s), fluorescence starts to decrease rapidly until it is no longer possible to detect it. This drop can be explained by either the evaporation of the liquid due to the increase in temperature during the experiment duration, or the displacement of the remaining liquid quantity within the

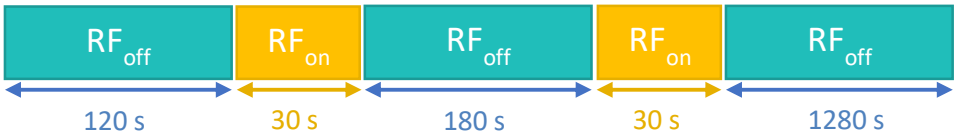


Figure 106 : Schema of the time slots assigned to the RF exposure and to the no RF used with the microfluidic channel.

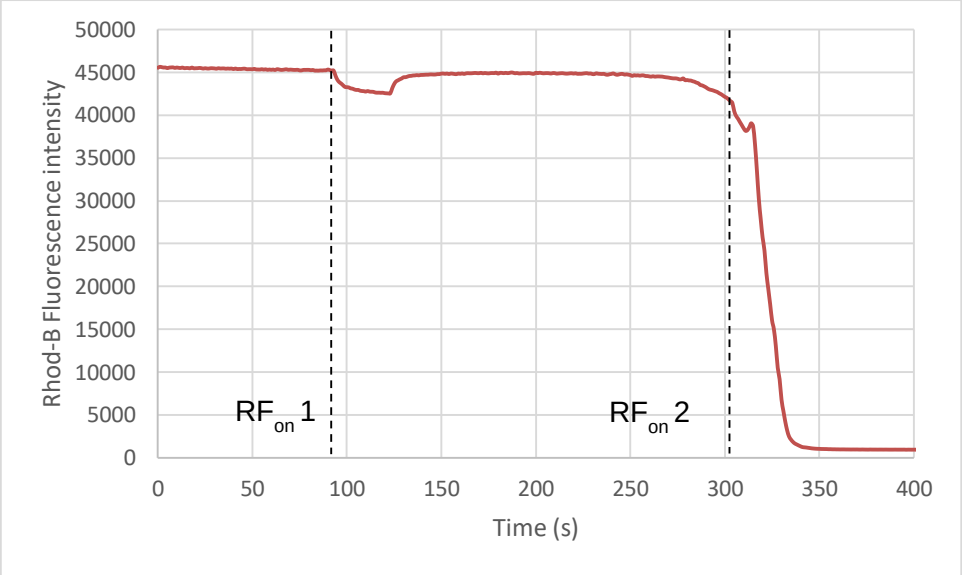


Figure 107 : Rhod-B fluorescence intensity recorded within the medium in one of the channels while applying the CW signal twice.

microchannel from the focal area. From this experiment, we conclude that in static conditions, samples should be exposed one time to the E-fields to avoid the effects aforementioned.

For comparison and feedback with the experimental measurements, the microfluidic chip was modeled and evaluated numerically with the FDTD method. A perfect electric conductor (PEC) was assigned to design the exposure microelectrodes, the wire bondings and the CPWs ensuring the transition between the chip and the SMA connectors. The PCB, the silica substrate and the polymer were defined with relative permittivity 4.3, 3.8 and 3.58, respectively. The microchannel chip was simulated with a non-uniform spatial resolution with a discretization of 5 µm for the microelectrodes forming the CPW. The SAR distribution depicted in Figure 108 is obtained at 1.8 GHz for the microchannels filled with culture medium that was defined by a 76 relative permittivity and a 2.3 S/m conductivity. SAR efficiency rises

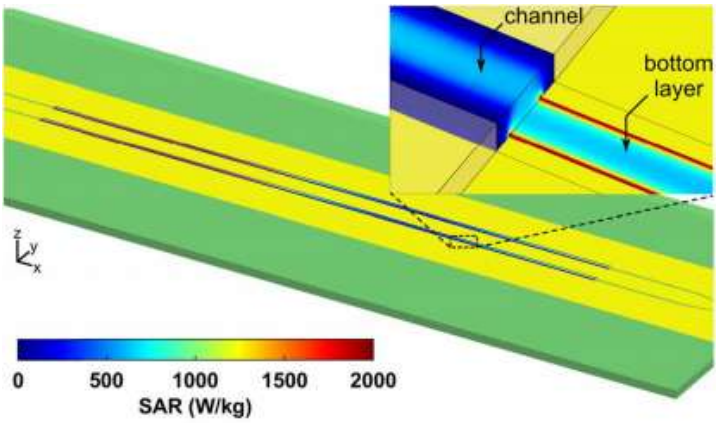


Figure 108 : SAR spatial distribution at 1.8 GHz within the microfluidic channel filled a drop of HBSS and covered by a glass slide. SAR values are normalized per 1 mW incident power [167].

along the microchannels. The highest values are observed in the inset of Figure 108 at the microelectrodes edges. Except for this area, SAR shows homogeneity along the width and the thickness of the channel.

The characterization of the microfluidic exposure device is achieved in static conditions where drops of medium are placed within the channels instead of fluids circulating by perfusion. This device has a good impedance match and high energy transfer. The application of the Rhod-B technique allowed to retrieve the temperature elevation within the channel and showed that in static conditions, RF exposure should be applied once due to some effects observed during the experiments. The local microscopic experimental SAR is rather high and the numerical values are more elevated. They are homogenous locally but vary along the channels length. This disparity can only be explained after conducting further assessments because the experimental SAR value represents a preliminary result. Thus for future experiments, lower power intensities application is required to avoid the extreme heating due to the high E-field intensities applied. Lowering the temperature induced prevents the evaporation of the medium that was encountered. More investigations need to be performed for optimization and better control of the Rhod-B technique and a better understanding of the functioning of this type of system. It is important also to obtain reproducible results confirming the accuracy of the findings.

# Conclusion

This chapter presented the microscopic dosimetry of microsystems. Experimentally, measurements were based on the use of Rhod-B and its temperature dependency. Its fluorescence intensity was detected using a microscope and then data were converted to temperature values. This technique was applied to the MEAs, with a drop of the medium on a glass slide and with a microfluidic chip. The temperature could not be detected with conventional tools such as the fiber optic probe within most of the microsystems due to the reduced amount of medium used and the extremely small channels and components of these devices. Therefore, detecting changes at the cellular level requires the use of advanced techniques.

The microscopic scale characterization of the microelectrode array recording devices (MEA-1 and MEA-2) was presented. Fluorescence intensities were successfully recorded in both MEAs. Due to the larger aperture of MEA-1, recordings were achieved at several positions including the electrodes area. The temperature conversion outcome and SAR values were higher than those obtained with the fiber optic probe. For example, at the microelectrodes area, the SAR values obtained are 70.3 and 159 W/kg with the probe method and the Rhod-B technique, respectively. Both measuring methods showed certain inhomogeneity within the MEA-1 and the microscale analysis indicated that the medium was homogenously exposed between the electrodes. Microscopic measurements within MEA-2 were allowed only at the zone of electrodes because of the small size of its observation cavity. Rhod-B based technique provides higher SAR values (7 W/kg) compared to measuring standard method (3.76 W/kg) and proves the homogeneity of the energy doses absorbed between the electrodes. It is important to ensure the homogeneity of SAR between the microelectrodes because, in the electrophysiological studies, the exposed cells will be placed between the electrodes regardless of the exposure device used. SAR probe values retrieved from the detection of temperature with Luxtron probe at different positions are quite inhomogeneous within the culture chamber. Compared to the MEA-1, the second MEA is considered steadier and showed less inhomogeneity within the culture chamber and lower SAR values. Numerical microscopic dosimetry of MEA-2 was complex, modifications were conducted to the TEM cell design to simplify the simulation and enhance the spatial resolution. The compact TEM cell and the simplified MEA-2 assessments emphasized the experimental characterization results in terms of homogeneity at the cell layer level. Through the macroscale and the microscale dosimetry,

results showed that MEA-2 recording device has more stability in terms of SAR and temperature within the exposed area, representing a better device for future electrophysiological experiments like the recording of neuronal activities.

Rhod-B was then applied to a drop of the medium on a glass slide within the TEM cell. The fluorescence intensity detected did not show the variation that could be associated with RF exposure. However, SAR spatial distribution within the drop could be retrieved due to the numerical simulations. The numerical SAR was homogenous at the bottom of the drop which represents the area of interest of the microscopy measurement technique.

Thereafter, this technique was applied to a microfluidic channel device. With the optimization of certain microscope settings, fluorescence intensity recording was achieved in static conditions. Temperature variation and SAR values were extracted. The energy absorbed by the medium within the channel was high even for low incident power values. The experimental SAR within the microfluidic channel was about 14.5 kW/kg/Winc. Numerical analysis showed also homogenous E-field with high intensities within the channels. Thus, to expose cells to RF-EMF within the microfluidic channel, incident power should be thoroughly selected to avoid cell damage due to the high thermal effects.

# Conclusion and perspectives

Bioelectromagnetics is a multidisciplinary field in which the studies focus on the biological and health effects due to the EMFs exposure. The studies performed during this thesis are affiliated to the *in vitro* bioelectromagnetic studies and are interested in achieving fine characterization of biological microsystems mainly the microscopic scale.

Mobile communication signals of the second generation particularly the GSM-1800 band are still in operation. Extensive databases and models for sophisticated dosimetry exist and did not evidence particular health hazards. Nonetheless, uncertainties can occur during studies thus research needs to continue by investigating approaches increasing complexity. An RF exposure device based on a TEM cell and an microelectrode array MEA which is an electrophysiological recording device are characterized for biological studies aiming to determine the mobile GSM signal effects on neurons. The fine characterization required the investigation of a Rhodamine B (Rhod-B) dye microscopy technique that consisted in calibrating and evaluating its sensitivity to several experimental parameters. Using a TEM cell exposure device, an optical fiber temperature probe and a microscope, the sensitivity of the Rhod-B fluorescence intensity was determined. From the experiments, it was determined that the minimum recommended concentration value of Rhod-B within the medium is 50 µM. This concentration induced accurate temperature results even for low powers. For short duration exposures, the recording of the fluorescence intensity should be set at 1 sample/s. Higher values induce erroneous outcomes or can cause photobleaching. Following the Rhod-B optimization, a calibration equation was determined allowing to convert the fluorescence intensity values into temperature variation. Unlike other calibration equations, this equation is based on a conversion coefficient α that is independent of the initial value of temperature.

Afterward, several MEA chips were characterized at the macroscopic scale by applying a CW signal at 1.8 GHz and measuring the temperature elevation induced with an optical fiber probe. This was studied for several configurations i.e. when the MEA and the TEM cell were suspended in the air by metal rods, placed on a dielectric support or a conductor support or coupled with the MEA's preamplifier system. The experimental SAR probe values retrieved showed a certain inhomogeneity within the MEA-1 that was significantly higher within MEA-2. These experiments concluded that adding a conductor under the systems decreased the SAR and that MEA-2 is more stable and less influenced by changing the material underneath.

Numerical simulations were conducted with simplified designs of MEAs to facilitate the simulations and study the variation of the E-field and SAR toward the changes of the materials placed under the MEAs. The SAR spatial distribution within MEA-1 is highly inhomogeneous in most configurations. MEA-2 SAR distributions have good homogeneity in all the configurations proving its stability. The SAR probe and SAR bottom values show certain variation within MEA-2 due to the value increase of SAR values at the observation cavity position. In general, the numerical SAR probe values were lower than the experimental ones and that can be explained by the numerical modelling simplifications such as the lack of the microelectrodes and lines in the MEAs designs.

To complete the characterization of the MEAs, microscopic dosimetry was conducted based on the Rhod-B technique. The TEM cell and the MEA were placed in the microscope stage for fluorescence intensity measurements in different positions within the central area. The local SAR values within the MEA-1 was retrieved at the microelectrodes area and at several positions were conducting lines are located. The results are quite inhomogeneous and the highest local SAR value is obtained at the area of interest which is the area of the electrodes with 159 ± 34.3 W/kg. Within the MEA-2, the small size of the observation cavity allowed the fluorescence intensity measurements only at the electrodes area where the local SAR was determined to be 7 ± 1.04 W/kg. According to these experimental results, it is recommended to use the MEA-2 for studies with neuron cells as it induces lower temperature variation and is steadier. Numerically, a spatial resolution issue related to the meshing was counteracted by designing a compact TEM cell. The SAR spatial distribution obtained with the compact TEM has great homogeneity between the electrodes and the values were locally heightened at the electrode location. This simulations showed the electrodes impact on the SAR values especially the local and bottom values.

Finally, the Rhod-B technique was tested with another microsystem which is an microfluidic exposure device. Assessments were conducted in static conditions. The experimental local SAR obtained was about 14.5 kW/kg retrieved from a limited number of fluorescence results. Numerical SAR spatial distribution showed local homogeneity within the channel but also variation along the channel length. These experiments were challenging and complex but they allowed obtaining preliminary results. This microsystem needs further assessments and optimizations for better control of the Rhod-B technique. It is important also to obtain reproducible results confirming findings accuracy. This is one of the perspectives of this study.

Moreover, following the experimental microscopic characterization of the MEAs, conducting in vitro studies with neuronal cells using the Rhod-B technique can be considered for future work. During the exposure of these cells to mobile signals at 1.8 GHz, fluorescence intensities should be recorded allowing the assessments of their temperature variations as well as the observation of potential biological changes in real-time.

The fifth generation (5G) of mobile communication is available and its utilization starts to spread and increase all over the world. Thus, it is essential to proceed with bioelectromagnetic studies in the 5G bands such as 3.5 GHz. Therefore, the MEAs can be suitable to study the electrical activity of neurons in the 5G-band. Characterizing this recording device at this frequency allows determining the coupling levels between the E-field and the biological medium along with the induced temperature and the SAR. Thereafter, the effects of the mobile signals at this frequency on neurons can be investigated.

The Rhod-B technique can be applied on other microsystems to assess from the fluorescence results the homogeneity of the exposure and the energy absorption levels. This technique can be used for different RF signal frequencies, E-field exposure intensities or device sizes. Furthermore, it will be interesting to study the efficiency of the Rhod-B fluorescence with long-term exposures over a few hours or days. In this case, the biological changes occurring during long exposures or even after a few days can be recorded.

# Bibliography


[1] H. Mehta, D. Patel, B. Joshi, et H. Modi, « 0G to 5G Mobile Technology: A Survey », vol. 1, nº 6, p. 5, 2014.

[2] K. M S et D. K. Vali, « A Survey on Evolution of Mobile Communication from 1G to 7G », in *NCICCNDA*, juin 2018, p. 391-397, doi: 10.21467/proceedings.1.61.

[3] Prinima et J. Pruthi, « Evolution of Mobile Communication Network: from 1G to 5G », *International Journal of Innovative Research in Computer and Communication Engineering*, 2016.

[4] H. Karjaluoto, « An Investigation of Third Generation (3G) Mobile Technologies and Services », *Contemp. Manag. Res.*, vol. 2, nº 2, p. 91, janv. 2007, doi: 10.7903/cmr.653.

[5] L. J. Vora, « Evolution of mobile generation technology: 1G to 5G and review of upcoming wireless technology 5G », *Int. J. Mod. Trends Eng. Res. IJMTER*, vol. 02, nº 10, p. 11, 2015.

[6] J. Lausson, « La TNT libère de nouvelles « fréquences en or » pour la 4G », *Numerama*, janv. 23, 2018. https://www.numerama.com/tech/323789-la-tnt-libere-de-nouvelles-frequences-en-or-pour-la-4g.html (consulté le nov. 23, 2020).

[7] « Introducing 5G technology and networks (speed, use cases and rollout). », *THALES group*. https://www.thalesgroup.com/en/markets/digital-identity-and-security/mobile/inspired/5G (consulté le nov. 18, 2020).

[8] G. Madeswaran, « Advancement of Wireless Generations-The Revolution », *ColorOS Know How*. https://community.coloros.com/thread-29070-1-1.html (consulté le sept. 22, 2020).

[9] D. J. Griffiths, *Introduction to electrodynamics*, Fourth edition. Boston: Pearson, 2013.

[10] S. Gabriel, R. W. Lau, et C. Gabriel, « The dielectric properties of biological tissues: II. Measurements in the frequency range 10 Hz to 20 GHz », *Phys. Med. Biol.*, vol. 41, nº 11, p. 2251–2269, nov. 1996, doi: 10.1088/0031-9155/41/11/002.

[11] « EMF-Portal | Radio frequency (10 MHz–300 GHz) ». https://www.emf-portal.org/en/cms/page/home/effects/radio-frequency (consulté le juill. 07, 2020).

[12] V. Anderson, « 1g vs 10g SAR average mass », présenté à ICNIRP/ACEBR/ARPANSA Wollongong Workshop, 2014, [En ligne]. Disponible sur: https://www.icnirp.org/cms/upload/presentations/rf/RFWshop_Anderson.pdf.

[13] « EMF-Portal | Mobile communication », *EMF - PORTAL*. https://www.emf-portal.org/en/cms/page/home/technology/radio-frequency/mobile-communication (consulté le sept. 23, 2020).

[14] International Commission on Non-Ionizing Radiation Protection (ICNIRP)1, « Guidelines for Limiting Exposure to Electromagnetic Fields (100 kHz to 300 GHz) »:, *Health Phys.*, vol. 118, nº 5, p. 483-524, mai 2020, doi: 10.1097/HP.0000000000001210.

[15] J. Cooper, B. Marx, J. Buhl, et V. Hombach, « Determination of safety distance limits for a human near a cellular base station antenna, adopting the IEEE standard or ICNIRP guidelines », *Bioelectromagnetics*, vol. 23, nº 6, p. 429-443, sept. 2002, doi: 10.1002/bem.10037.

[16] C. Chakraborty et A. Singh, « Determination of safe distance limit from Cellular Base station radiation exposure using SAR analysis », *Int J Comput Appl*, vol. 55, p. 18–22, 2013.

[17] J. D. Ramsey, C. L. Burford, M. Y. Beshir, et R. C. Jensen, « Effects of workplace thermal conditions on safe work behavior », *J. Safety Res.*, vol. 14, nº 3, p. 105–114, 1983.

[18] W. P. Cheshire, « Thermoregulatory disorders and illness related to heat and cold stress », *Auton. Neurosci.*, vol. 196, p. 91-104, avr. 2016, doi: 10.1016/j.autneu.2016.01.001.

[19] Y. Takashima, H. Hirose, S. Koyama, Y. Suzuki, M. Taki, et J. Miyakoshi, « Effects of continuous and intermittent exposure to RF fields with a wide range of SARs on cell growth, survival, and cell cycle distribution », *Bioelectromagnetics*, vol. 27, nº 5, p. 392-400, 2006, doi: 10.1002/bem.20220.

[20] K.-A. Hossmann et D. M. Hermann, « Effects of electromagnetic radiation of mobile phones on the central nervous system », *Bioelectromagnetics*, vol. 24, nº 1, p. 49-62, janv. 2003, doi: 10.1002/bem.10068.

[21] E. Valentini, G. Curcio, F. Moroni, M. Ferrara, L. De Gennaro, et M. Bertini, « Neurophysiological effects of mobile phone electromagnetic fields on humans: a comprehensive review », *Bioelectromagnetics*, vol. 28, nº 6, p. 415-432, sept. 2007, doi: 10.1002/bem.20323.

[22] S. Siuly, Y. Li, et Y. Zhang, « Electroencephalogram (EEG) and Its Background », *EEG Signal Anal. Classif.*, p. 3-21, 2016, doi: 10.1007/978-3-319-47653-7_1.

[23] « Avis de l'Anses relatif à la mise a jour de l'expertise "Radiofréquence et santé" », oct. 2009. Consulté le: sept. 26, 2020. [En ligne]. Disponible sur: https://www.anses.fr/fr/system/files/AP2007et0007Ra.pdf.

[24] « Avis de l'Anses relatif à la mise a jour de l'expertise "Radiofréquence et santé" », oct. 2013. Consulté le: sept. 26, 2020. [En ligne]. Disponible sur: https://www.anses.fr/fr/system/files/AP2011sa0150Ra.pdf.

[25] J.-C. Cassel, B. Cosquer, R. Galani, et N. Kuster, « Whole-body exposure to 2.45 GHz electromagnetic fields does not alter radial-maze performance in rats », *Behav. Brain Res.*, vol. 155, nº 1, p. 37–43, 2004.

[26] B. L. Cobb, J. R. Jauchem, et E. R. Adair, « Radial arm maze performance of rats following repeated low level microwave radiation exposure », *Bioelectromagnetics*, vol. 25, nº 1, p. 49–57, 2004.

[27] T. Kumlin *et al.*, « Mobile Phone Radiation and the Developing Brain: Behavioral and Morphological Effects in Juvenile Rats », *Radiat. Res.*, vol. 168, nº 4, p. 471-479, oct. 2007, doi: 10.1667/RR1002.1.

[28] G. W. Arendash *et al.*, « Electromagnetic field treatment protects against and reverses cognitive impairment in Alzheimer's disease mice », *J. Alzheimers Dis.*, vol. 19, nº 1, p. 191–210, 2010.

[29] T. Mori et G. W. Arendash, « Long-term electromagnetic field treatment increases brain neuronal activity: linkage to cognitive benefit and therapeutic implications for Alzheimer's disease », *J Alzheimer's Park.*, vol. 1, nº 2, p. 2161–0460, 2011.

[30] G. W. Arendash, T. Mori, M. Dorsey, R. Gonzalez, N. Tajiri, et C. Borlongan, « Electromagnetic treatment to old Alzheimer's mice reverses β-amyloid deposition, modifies cerebral blood flow, and provides selected cognitive benefit », *PLoS One*, vol. 7, nº 4, p. e35751, 2012.

[31] R. Luria, I. Eliyahu, R. Hareuveny, M. Margaliot, et N. Meiran, « Cognitive effects of radiation emitted by cellular phones: the influence of exposure side and time », *Bioelectromagn. J. Bioelectromagn. Soc. Soc. Phys. Regul. Biol. Med. Eur. Bioelectromagn. Assoc.*, vol. 30, nº 3, p. 198–204, 2009.

[32] R. Hareuveny, I. Eliyahu, R. Luria, N. Meiran, et M. Margaliot, « Cognitive effects of cellular phones: A possible role of non-radiofrequency radiation factors », *Bioelectromagnetics*, vol. 32, nº 7, p. 585–588, 2011.

[33] S. Leung *et al.*, « Effects of 2G and 3G mobile phones on performance and electrophysiology in adolescents, young adults and older adults », *Clin. Neurophysiol.*, vol. 122, nº 11, p. 2203–2216, 2011.

[34] M. S. Kwon *et al.*, « GSM mobile phone radiation suppresses brain glucose metabolism », *J. Cereb. Blood Flow Metab.*, vol. 31, nº 12, p. 2293–2301, 2011.

[35] M. S. Kwon *et al.*, « No effects of short-term GSM mobile phone radiation on cerebral blood flow measured using positron emission tomography », *Bioelectromagnetics*, vol. 33, nº 3, p. 247–256, 2012.

[36] C. Sauter *et al.*, « Effects of exposure to electromagnetic fields emitted by GSM 900 and WCDMA mobile phones on cognitive function in young male subjects », *Bioelectromagnetics*, vol. 32, nº 3, p. 179–190, 2011.

[37] S. Spichtig, F. Scholkmann, L. Chin, H. Lehmann, et M. Wolf, « Assessment of intermittent UMTS electromagnetic field effects on blood circulation in the human auditory region using a near-infrared system », *Bioelectromagnetics*, vol. 33, nº 1, p. 40–54, 2012.

[38] G. Curcio *et al.*, « Effects of mobile phone signals over BOLD response while performing a cognitive task », *Clin. Neurophysiol.*, vol. 123, nº 1, p. 129–136, 2012.

[39] A. Pelletier *et al.*, « Effects of chronic exposure to radiofrequency electromagnetic fields on energy balance in developing rats », *Environ. Sci. Pollut. Res.*, vol. 20, nº 5, p. 2735–2746, 2013.

[40] E. Mohler *et al.*, « Effects of everyday radiofrequency electromagnetic-field exposure on sleep quality: a cross-sectional study », *Radiat. Res.*, vol. 174, nº 3, p. 347–356, 2010.

[41] E. Mohler, P. Frei, J. Fröhlich, C. Braun-Fahrländer, et M. Röösli, « Exposure to radiofrequency electromagnetic fields and sleep quality: a prospective cohort study », *PloS One*, vol. 7, nº 5, p. e37455, 2012.

[42] H. Danker-Hopfe, H. Dorn, C. Bornkessel, et C. Sauter, « Do mobile phone base stations affect sleep of residents? Results from an experimental double-blind sham-controlled field study », *Am. J. Hum. Biol.*, vol. 22, nº 5, p. 613–618, 2010.

[43] S. Heinrich, S. Thomas, C. Heumann, R. von Kries, et K. Radon, « The impact of exposure to radio frequency electromagnetic fields on chronic well-being in young people—a cross-sectional study based on personal dosimetry », *Environ. Int.*, vol. 37, nº 1, p. 26–30, 2011.

[44] H. DANKER-HOPFE, H. Dorn, A. Bahr, P. Anderer, et C. Sauter, « Effects of electromagnetic fields emitted by mobile phones (GSM 900 and WCDMA/UMTS) on the macrostructure of sleep », *J. Sleep Res.*, vol. 20, nº 1pt1, p. 73–81, 2011.

[45] M. R. Schmid *et al.*, « Sleep EEG alterations: effects of different pulse-modulated radio frequency electromagnetic fields », *J. Sleep Res.*, vol. 21, nº 1, p. 50–58, 2012.

[46] S. P. Loughran, R. J. McKenzie, M. L. Jackson, M. E. Howard, et R. J. Croft, « Individual differences in the effects of mobile phone exposure on human sleep: rethinking the problem », *Bioelectromagnetics*, vol. 33, nº 1, p. 86–93, 2012.

[47] R. Paulraj et J. Behari, « Effects of low level microwave radiation on carcinogenesis in Swiss Albino mice », *Mol. Cell. Biochem.*, vol. 348, nº 1-2, p. 191–197, 2011.

[48] H.-J. Lee *et al.*, « Lymphoma development of simultaneously combined exposure to two radiofrequency signals in AKR/J mice », *Bioelectromagnetics*, vol. 32, nº 6, p. 485–492, 2011.

[49] M. P. Little *et al.*, « Mobile phone use and glioma risk: comparison of epidemiological study results with incidence trends in the United States », *BMJ*, vol. 344, mars 2012, doi: 10.1136/bmj.e1147.

[50] I. S. Group, « Brain tumour risk in relation to mobile telephone use: results of the INTERPHONE international case–control study », *Int. J. Epidemiol.*, vol. 39, n° 3, p. 675–694, 2010.

[51] L. Hardell, M. CARLbERG, et K. Hansson Mild, « Pooled analysis of case-control studies on malignant brain tumours and the use of mobile and cordless phones including living and deceased subjects », *Int. J. Oncol.*, vol. 38, n° 5, p. 1465–1474, 2011.

[52] J. Schüz *et al.*, « Long-term mobile phone use and the risk of vestibular schwannoma: a Danish nationwide cohort study », *Am. J. Epidemiol.*, vol. 174, n° 4, p. 416–422, 2011.

[53] D. Pettersson *et al.*, « Long-term mobile phone use and acoustic neuroma risk », *Epidemiology*, p. 233–241, 2014.

[54] P. Elliott *et al.*, « Mobile phone base stations and early childhood cancers: case-control study », *Bmj*, vol. 340, 2010.

[55] R. Cooke, S. Laing, et A. J. Swerdlow, « A case–control study of risk of leukaemia in relation to mobile phone use », *Br. J. Cancer*, vol. 103, n° 11, p. 1729–1735, 2010.

[56] I. Deltour *et al.*, « Mobile Phone Use and Incidence of Glioma in the Nordic Countries 1979—2008: Consistency Check », *Epidemiology*, p. 301–307, 2012.

[57] National Toxicology Program (NTP), « NTP Technical Report on the Toxicology and Carcinogenesis Studies in Hsd:Sprague Dawley SD Rats Exposed to Whole-Body Radio Frequency Radiation at a Frequency (900 MHz) and Modulations (GSM and CDMA) Used by Cell Phones », 595, nov. 2018. doi: 10.22427/NTP-TR-595.

[58] M.-P. Rols, « Electropermeabilization, a physical method for the delivery of therapeutic molecules into cells », *Biochim. Biophys. Acta BBA - Biomembr.*, vol. 1758, n° 3, p. 423-428, mars 2006, doi: 10.1016/j.bbamem.2006.01.005.

[59] A. G. Pakhomov, D. Miklavcic, et M. S. Markov, *Advanced Electroporation Techniques in Biology and Medicine*. CRC Press, 2010.

[60] S. I. Sukharev, V. A. Klenchin, S. M. Serov, L. V. Chernomordik, et C. YuA, « Electroporation and electrophoretic DNA transfer into cells. The effect of DNA interaction with electropores », *Biophys. J.*, vol. 63, n° 5, p. 1320–1327, 1992.

[61] R. Heller *et al.*, « In vivo gene electroinjection and expression in rat liver », *FEBS Lett.*, vol. 389, n° 3, p. 225-228, 1996, doi: 10.1016/0014-5793(96)00590-X.

[62] E. P. Spugnini *et al.*, « Electrochemotherapy for the treatment of squamous cell carcinoma in cats: a preliminary report », *Vet. J.*, vol. 179, n° 1, p. 117–120, 2009.

[63] G. Pucihar, J. Krmelj, M. Reberšek, T. B. Napotnik, et D. Miklavčič, « Equivalent pulse parameters for electroporation », *IEEE Trans. Biomed. Eng.*, vol. 58, n° 11, p. 3279–3288, 2011.

[64] P. Kramar, D. Miklavcic, et A. M. Lebar, « Determination of the lipid bilayer breakdown voltage by means of linear rising signal », *Bioelectrochemistry*, vol. 70, n° 1, p. 23–27, 2007.

[65] P. T. Vernier, Y. Sun, et M. A. Gundersen, « Nanoelectropulse-driven membrane perturbation and small molecule permeabilization », *BMC Cell Biol.*, vol. 7, n° 1, p. 37, 2006.

[66] R. P. Joshi et K. H. Schoenbach, « Bioelectric Effects of Intense Ultrashort Pulses », *Crit. Rev. Biomed. Eng.*, vol. 38, n° 3, 2010, doi: 10.1615/CritRevBiomedEng.v38.i3.20.

[67] G. L. Thompson, C. C. Roth, M. A. Kuipers, G. P. Tolstykh, H. T. Beier, et B. L. Ibey, « Permeabilization of the nuclear envelope following nanosecond pulsed electric field exposure », *Biochem. Biophys. Res. Commun.*, vol. 470, n° 1, p. 35–40, 2016.

[68] M. OKINO et H. MOHRI, « Effects of a high-voltage electrical impulse and an anticancer drug on in vivo growing tumors », *Jpn. J. Cancer Res. GANN*, vol. 78, nº 12, p. 1319–1321, 1987.

[69] J. Gehl et P. F. Geertsen, « Palliation of haemorrhaging and ulcerated cutaneous tumours using electrochemotherapy », *Eur. J. Cancer Suppl.*, vol. 4, nº 11, p. 35–37, 2006.

[70] E. Neumann, M. Schaefer-Ridder, Y. Wang, et P. H. Hofschneider, « Gene transfer into mouse lyoma cells by electroporation in high electric fields. », *EMBO J.*, vol. 1, nº 7, p. 841-845, juill. 1982, doi: 10.1002/j.1460-2075.1982.tb01257.x.

[71] L. M. Mir *et al.*, « High-efficiency gene transfer into skeletal muscle mediated by electric pulses », *Proc. Natl. Acad. Sci.*, vol. 96, nº 8, p. 4262-4267, avr. 1999, doi: 10.1073/pnas.96.8.4262.

[72] J. Gehl, « Electroporation: theory and methods, perspectives for drug delivery, gene therapy and research », *Acta Physiol. Scand.*, vol. 177, nº 4, p. 437–447, 2003.

[73] P. Chiarella, V. Michele Fazio, et E. Signori, « Electroporation in DNA vaccination protocols against cancer », *Curr. Drug Metab.*, vol. 14, nº 3, p. 291–299, 2013.

[74] S. Raffy, C. Lazdunski, et J. Teissié, « Electroinsertion and activation of the C-terminal domain of colicin A, a voltage gated bacterial toxin, into mammalian cell membranes », *Mol. Membr. Biol.*, vol. 21, nº 4, p. 237–246, 2004.

[75] S. Shayanfar, O. P. Chauhan, S. Toepfl, et V. Heinz, « The interaction of pulsed electric fields and texturizing-antifreezing agents in quality retention of defrosted potato strips », *Int. J. Food Sci. Technol.*, vol. 48, nº 6, p. 1289–1295, 2013.

[76] C. Gusbeth, W. Frey, H. Volkmann, T. Schwartz, et H. Bluhm, « Pulsed electric field treatment for bacteria reduction and its impact on hospital wastewater », *Chemosphere*, vol. 75, nº 2, p. 228–233, 2009.

[77] H. Ye, L.-L. Huang, S.-D. Chen, et J.-J. Zhong, « Pulsed electric field stimulates plant secondary metabolism in suspension cultures of Taxus chinensis », *Biotechnol. Bioeng.*, vol. 88, nº 6, p. 788–795, 2004.

[78] N. M. M. T. Saw, H. Riedel, Z. Cai, O. Kütük, et I. Smetanska, « Stimulation of anthocyanin synthesis in grape (Vitis vinifera) cell cultures by pulsed electric fields and ethephon », *Plant Cell Tissue Organ Cult. PCTOC*, vol. 108, nº 1, p. 47–54, 2012.

[79] J. C. Weaver, K. C. Smith, A. T. Esser, R. S. Son, et T. R. Gowrishankar, « A brief overview of electroporation pulse strength–duration space: A region where additional intracellular effects are expected », *Bioelectrochemistry*, vol. 87, p. 236–243, 2012.

[80] R. E. Neal III, J. H. Rossmeisl Jr, P. A. Garcia, O. I. Lanz, N. Henao-Guerrero, et R. V. Davalos, « Successful treatment of a large soft tissue sarcoma with irreversible electroporation », 2011.

[81] L. Miller, J. Leor, et B. Rubinsky, « Cancer cells ablation with irreversible electroporation », *Technol. Cancer Res. Treat.*, vol. 4, nº 6, p. 699–705, 2005.

[82] S. Mahnič-Kalamiza, E. Vorobiev, et D. Miklavčič, « Electroporation in Food Processing and Biorefinery », *J. Membr. Biol.*, vol. 247, nº 12, p. 1279-1304, déc. 2014, doi: 10.1007/s00232-014-9737-x.

[83] S. Xiao, S. Guo, V. Nesin, R. Heller, et K. H. Schoenbach, « Subnanosecond Electric Pulses Cause Membrane Permeabilization and Cell Death », *IEEE Trans. Biomed. Eng.*, vol. 58, nº 5, p. 1239-1245, mai 2011, doi: 10.1109/TBME.2011.2112360.

[84] A. Paffi *et al.*, « Considerations for Developing an RF Exposure System: A Review for in vitro Biological Experiments », *IEEE Trans. Microw. Theory Tech.*, vol. 58, nº 10, p. 2702-2714, oct. 2010, doi: 10.1109/TMTT.2010.2065351.

[85] A. Paffi *et al.*, « Microwave Exposure Systems for In Vivo Biological Experiments: A Systematic Review », *IEEE Trans. Microw. Theory Tech.*, vol. 61, nº 5, p. 1980-1993, mai 2013, doi: 10.1109/TMTT.2013.2246183.

[86] J. W. Hansen *et al.*, « A Systematic Review of In Vitro and In Vivo Radio Frequency Exposure Methods », *IEEE Rev. Biomed. Eng.*, vol. 13, p. 340-351, 2020, doi: 10.1109/RBME.2019.2912023.

[87] A. Schirmacher *et al.*, « Electromagnetic fields (1.8 GHz) increase the permeability to sucrose of the blood–brain barrier in vitro », *Bioelectromagnetics*, vol. 21, nº 5, p. 338-345, 2000, doi: 10.1002/1521-186X(200007)21:5<338::AID-BEM2>3.0.CO;2-Q.

[88] O. Zeni *et al.*, « Evaluation of genotoxic effects in human peripheral blood leukocytes following an acute in vitro exposure to 900 MHz radiofrequency fields », *Bioelectromagnetics*, vol. 26, nº 4, p. 258-265, 2005, doi: 10.1002/bem.20078.

[89] P. Koester, J. Sakowski, W. Baumann, H.-W. Glock, et J. Gimsa, « A new exposure system for the in vitro detection of GHz field effects on neuronal networks », *Bioelectrochemistry*, vol. 70, nº 1, p. 104–114, 2007.

[90] M. R. Lambrecht, I. Chatterjee, D. Mcpherson, J. Quinn, T. Hagan, et G. L. Craviso, « Design, Characterization, and Optimization of a Waveguide-Based RF/MW Exposure System for Studying Nonthermal Effects on Skeletal Muscle Contraction », *IEEE Trans. Plasma Sci.*, vol. 34, nº 4, p. 1470-1479, août 2006, doi: 10.1109/TPS.2006.876490.

[91] C. P. Wen, « Coplanar waveguide: A surface strip transmission line suitable for nonreciprocal gyromagnetic device applications », *IEEE Trans. Microw. Theory Tech.*, vol. 17, nº 12, p. 1087–1090, 1969.

[92] M. Liberti, F. Apollonio, A. Paffi, M. Pellegrino, et G. D'Inzeo, « A coplanar-waveguide system for cells exposure during electrophysiological recordings », *IEEE Trans. Microw. Theory Tech.*, vol. 52, nº 11, p. 2521-2528, nov. 2004, doi: 10.1109/TMTT.2004.837155.

[93] A. Paffi *et al.*, « A Real-Time Exposure System for Electrophysiological Recording in Brain Slices », *IEEE Trans. Microw. Theory Tech.*, vol. 55, nº 11, p. 2463-2471, nov. 2007, doi: 10.1109/TMTT.2007.908657.

[94] N. Nikoloski, J. Fröhlich, T. Samaras, J. Schuderer, et N. Kuster, « Reevaluation and improved design of the TEM cell in vitro exposure unit for replication studies », *Bioelectromagnetics*, vol. 26, nº 3, p. 215-224, 2005, doi: 10.1002/bem.20067.

[95] « TEM Cell and GTEM Guide For Radiated Emissions & Radiated Immunity Pre-Compliance Testing », *EMC FastPass*, févr. 21, 2020. https://emcfastpass.com/tem-cell-guide/ (consulté le oct. 04, 2020).

[96] M. L. Crawford, « Generation of Standard EM Fields Using TEM Transmission Cells », *IEEE Trans. Electromagn. Compat.*, vol. EMC-16, nº 4, p. 189-195, nov. 1974, doi: 10.1109/TEMC.1974.303364.

[97] F. Schönborn, K. Poković, M. Burkhardt, et N. Kuster, « Basis for optimization of in vitro exposure apparatus for health hazard evaluations of mobile communications », *Bioelectromagnetics*, vol. 22, nº 8, p. 547-559, 2001, doi: 10.1002/bem.83.

[98] S. M. Satav et V. Agarwal, « Do-it-yourself fabrication of an open TEM cell for EMC pre-compliance », *IEEE EMC Soc. Newsl.*, vol. 218, p. 66–71, 2008.

[99] B. R. R. Persson, L. G. Salford, et A. Brun, « Blood-brain barrier permeability in rats exposed to electromagnetic fields used in wireless communication », *Wirel. Netw.*, vol. 3, nº 6, p. 455-461, nov. 1997, doi: 10.1023/A:1019150510840.

[100] Salford Leif G, Brun Arne E, Eberhardt Jacob L, Malmgren Lars, et Persson Bertil R R, « Nerve cell damage in mammalian brain after exposure to microwaves from GSM mobile

phones. », *Environ. Health Perspect.*, vol. 111, nº 7, p. 881-883, juin 2003, doi: 10.1289/ehp.6039.

[101] O. Zeni, A. Schiavoni, A. Perrotta, D. Forigo, M. Deplano, et M. R. Scarfi, « Evaluation of genotoxic effects in human leukocytes after in vitro exposure to 1950 MHz UMTS radiofrequency field », *Bioelectromagnetics*, vol. 29, nº 3, p. 177-184, 2008, doi: 10.1002/bem.20378.

[102] G. Del Vecchio *et al.*, « Effect of radiofrequency electromagnetic field exposure on in vitro models of neurodegenerative disease », *Bioelectromagn. J. Bioelectromagn. Soc. Soc. Phys. Regul. Biol. Med. Eur. Bioelectromagn. Assoc.*, vol. 30, nº 7, p. 564–572, 2009.

[103] M. G. Moisescu, P. Leveque, J.-R. Bertrand, E. Kovacs, et L. M. Mir, « Microscopic observation of living cells during their exposure to modulated electromagnetic fields », *Bioelectrochemistry*, vol. 74, nº 1, p. 9–15, 2008.

[104] R. P. O'Connor, S. D. Madison, P. Leveque, H. L. Roderick, et M. D. Bootman, « Exposure to GSM RF Fields Does Not Affect Calcium Homeostasis in Human Endothelial Cells, Rat Pheocromocytoma Cells or Rat Hippocampal Neurons », *PLOS ONE*, vol. 5, nº 7, Art. nº 7, juill. 2010, doi: 10.1371/journal.pone.0011828.

[105] C. Merla, N. Ticaud, D. Arnaud-Cormos, B. Veyret, et P. Leveque, « Real-Time RF Exposure Setup Based on a Multiple Electrode Array (MEA) for Electrophysiological Recording of Neuronal Networks », *IEEE Trans. Microw. Theory Tech.*, vol. 59, nº 3, Art. nº 3, mars 2011, doi: 10.1109/TMTT.2010.2100404.

[106] S. Kohler, T. D. T. Vu, P. T. Vernier, D. Arnaud-Cormos, et P. Leveque, « Open transverse electromagnetic (tem) cell as applicator of high-intensity nsPEFs and electro-optic measurements », in *2012 IEEE International Power Modulator and High Voltage Conference (IPMHVC)*, 2012, p. 764–767.

[107] F. Schönborn, K. Poković, A. M. Wobus, et N. Kuster, « Design, optimization, realization, and analysis of an in vitro system for the exposure of embryonic stem cells at 1.71 GHz », *Bioelectromagnetics*, vol. 21, nº 5, p. 372-384, 2000, doi: 10.1002/1521-186X(200007)21:5<372::AID-BEM6>3.0.CO;2-S.

[108] J. Schuderer, T. Samaras, W. Oesch, D. Spat, et N. Kuster, « High peak SAR exposure unit with tight exposure and environmental control for in vitro experiments at 1800 MHz », *IEEE Trans. Microw. Theory Tech.*, vol. 52, nº 8, p. 2057-2066, août 2004, doi: 10.1109/TMTT.2004.832009.

[109] G. B. Gajda, J. P. McNamee, A. Thansandote, S. Boonpanyarak, E. Lemay, et P. V. Bellier, « Cylindrical waveguide applicator for in vitro exposure of cell culture samples to 1.9-GHz radiofrequency fields », *Bioelectromagnetics*, vol. 23, nº 8, p. 592–598, 2002.

[110] L. Laval, P. H. Leveque, et B. Jecko, « A new in vitro exposure device for the mobile frequency of 900 MHz », *Bioelectromagn. J. Bioelectromagn. Soc. Soc. Phys. Regul. Biol. Med. Eur. Bioelectromagn. Assoc.*, vol. 21, nº 4, p. 255–263, 2000.

[111] C. Delaveaud, P. Leveque, et B. Jecko, « New kind of microstrip antenna: the monopolar wire-patch antenna », *Electron. Lett.*, vol. 30, nº 1, p. 1-2, janv. 1994, doi: 10.1049/el:19940057.

[112] L. Ardoino, V. Lopresto, S. Mancini, R. Pinto, et G. A. Lovisolo, « 1800 MHz in vitro exposure device for experimental studies on the effects of mobile communication systems », *Radiat. Prot. Dosimetry*, vol. 112, nº 3, p. 419–428, 2004.

[113] T. Iyama *et al.*, « Large scale in vitro experiment system for 2 GHz exposure », *Bioelectromagnetics*, vol. 25, nº 8, p. 599-606, 2004, doi: 10.1002/bem.20038.

[114] P. Galloni *et al.*, « Effects of 900 MHz electromagnetic fields exposure on cochlear cells' functionality in rats: Evaluation of distortion product otoacoustic emissions », *Bioelectromagnetics*, vol. 26, nº 7, p. 536-547, 2005, doi: 10.1002/bem.20127.

[115] A. Peinnequin *et al.*, « Non-thermal effects of continuous 2.45 GHz microwaves on Fas-induced apoptosis in human Jurkat T-cell line », *Bioelectrochemistry*, vol. 51, nº 2, p. 157–161, 2000.

[116] Vijayalaxmi, « Cytogenetic studies in human blood lymphocytes exposed in vitro to 2.45 GHz or 8.2 GHz radiofrequency radiation », *Radiat. Res.*, p. 532–538, 2006.

[117] R. Araneo et S. Celozzi, « Design of a Microstrip Antenna Setup for Bio-Experiments on Exposure to High-Frequency Electromagnetic Field », *IEEE Trans. Electromagn. Compat.*, vol. 48, nº 4, p. 792-804, nov. 2006, doi: 10.1109/TEMC.2006.882857.

[118] J. W. Hansen *et al.*, « A far-field radio-frequency experimental exposure system with unrestrained mice », *SpringerPlus*, vol. 4, nº 1, p. 669, déc. 2015, doi: 10.1186/s40064-015-1433-5.

[119] S. M. Bardet, L. Carr, M. Soueid, D. Arnaud-Cormos, P. Leveque, et R. P. O'Connor, « Multiphoton imaging reveals that nanosecond pulsed electric fields collapse tumor and normal vascular perfusion in human glioblastoma xenografts », *Sci. Rep.*, vol. 6, nº 1, p. 34443, déc. 2016, doi: 10.1038/srep34443.

[120] Y.-H. Wu, D. Arnaud-Cormos, M. Casciola, J. M. Sanders, P. Leveque, et P. T. Vernier, « Moveable wire electrode microchamber for nanosecond pulsed electric-field delivery », *IEEE Trans. Biomed. Eng.*, vol. 60, nº 2, p. 489–496, 2012.

[121] L. C. Carr, S. M. Bardet, R. Burke, D. Arnaud-Cormos, P. Lévêque, et R. P. O 'connor, « Calcium-independent disruption of microtubule dynamics by nanosecond pulsed electric fields in U87 human glioblastoma cells », *Sci. Rep.*, vol. 7, p. 41267-41267, 2017, doi: 10.1038/srep41267.

[122] A. Nefzi, P. Leveque, et D. Arnaud-Cormos, « Frequency characterization of wire electrodes devices for biomedical applications », 2017.

[123] J. F. Kolb, S. Kono, et K. H. Schoenbach, « Nanosecond pulsed electric field generators for the study of subcellular effects », *Bioelectromagnetics*, vol. 27, nº 3, p. 172-187, 2006, doi: 10.1002/bem.20185.

[124] M. Kenaan, « Développement d'applicateurs pour étudier le comportement des cellules biologiques soumises à des impulsions électromagnétiques ultracourtes », These de doctorat, Limoges, 2010.

[125] A. Silve, R. Vezinet, et L. M. Mir, « Nanosecond-Duration Electric Pulse Delivery In Vitro and In Vivo: Experimental Considerations », *IEEE Trans. Instrum. Meas.*, vol. 61, nº 7, p. 1945-1954, juill. 2012, doi: 10.1109/TIM.2012.2182861.

[126] Y. Sun, P. T. Vernier, M. Behrend, L. Marcu, et M. A. Gundersen, « Electrode microchamber for noninvasive perturbation of mammalian cells with nanosecond pulsed electric fields », *IEEE Trans. NanoBioscience*, vol. 4, nº 4, Art. nº 4, déc. 2005, doi: 10.1109/TNB.2005.859544.

[127] M. Casciola, M. Liberti, A. Denzi, A. Paffi, C. Merla, et F. Apollonio, « A computational design of a versatile microchamber for in vitro nanosecond pulsed electric fields experiments », *Integration*, vol. 58, p. 446–453, 2017.

[128] C. Dalmay *et al.*, « A microfluidic biochip for the nanoporation of living cells », *Biosens. Bioelectron.*, vol. 26, nº 12, Art. nº 12, août 2011, doi: 10.1016/j.bios.2011.03.020.

[129] C. Dalmay, J. Villemejane, V. Joubert, O. Français, L. M. Mir, et B. Le Pioufle, « Design and realization of a microfluidic device devoted to the application of ultra-short pulses of

electrical field to living cells », *Sens. Actuators B Chem.*, vol. 160, nº 1, p. 1573–1580, 2011.

[130] A. G. Pakhomov, J. F. Kolb, J. A. White, R. P. Joshi, S. Xiao, et K. H. Schoenbach, « Long-lasting plasma membrane permeabilization in mammalian cells by nanosecond pulsed electric field (nsPEF) », *Bioelectromagn. J. Bioelectromagn. Soc. Soc. Phys. Regul. Biol. Med. Eur. Bioelectromagn. Assoc.*, vol. 28, nº 8, p. 655–663, 2007.

[131] R. Orlacchio, L. Carr, C. Palego, D. Arnaud-Cormos, et P. Leveque, « High-voltage 10 ns delayed paired or bipolar pulses for in vitro bioelectric experiments », *Bioelectrochemistry*, p. 107648, 2020.

[132] M. Kenaan *et al.*, « Characterization of a 50-Ω Exposure Setup for High-Voltage Nanosecond Pulsed Electric Field Bioexperiments », *IEEE Trans. Biomed. Eng.*, vol. 58, nº 1, Art. nº 1, janv. 2011, doi: 10.1109/TBME.2010.2081670.

[133] D. Arnaud-Cormos, P. Leveque, Y.-H. Wu, J. M. Sanders, M. A. Gundersen, et T. P. Vernier, « Microchamber Setup Characterization for Nanosecond Pulsed Electric Field Exposure », *IEEE Trans. Biomed. Eng.*, vol. 58, nº 6, p. 1656-1662, juin 2011, doi: 10.1109/TBME.2011.2108298.

[134] M. Bonakdar, P. M. Graybill, et R. V. Davalos, « A microfluidic model of the blood–brain barrier to study permeabilization by pulsed electric fields », *RSC Adv.*, vol. 7, nº 68, p. 42811-42818, 2017, doi: 10.1039/C7RA07603G.

[135] M. B. Fox *et al.*, « Electroporation of cells in microfluidic devices: a review », *Anal. Bioanal. Chem.*, vol. 385, nº 3, p. 474, 2006.

[136] S. W. Rhee, A. M. Taylor, C. H. Tu, D. H. Cribbs, C. W. Cotman, et N. L. Jeon, « Patterned cell culture inside microfluidic devices », *Lab. Chip*, vol. 5, nº 1, p. 102–107, 2005.

[137] « CST Studio Suite 3D EM simulation and analysis software ». https://www.3ds.com/products-services/simulia/products/cst-studio-suite/ (consulté le déc. 16, 2020).

[138] P. Leveque, R. O'Connor, et D. Arnaud-Cormos, « Measurement and Characterization of Exposure Systems for High-Frequency, Ultrashort Pulses », *Handb. Electroporation*, p. 1-24, 2017, doi: 10.1007/978-3-319-26779-1_207-1.

[139] « Dosimetric near field probes, SPEAG », *Speag*. https://speag.swiss/components/probes-2/dosimetric/ (consulté le nov. 28, 2020).

[140] « SAR Probes, MVG », *Microwave Vision Group (MVG)*. https://www.mvg-world.com/en/products/sar/sar-accessories/probes (consulté le nov. 28, 2020).

[141] M. J. M. Harrap, N. Hempel de Ibarra, H. M. Whitney, et S. A. Rands, « Reporting of thermography parameters in biology: a systematic review of thermal imaging literature », *R. Soc. Open Sci.*, vol. 5, nº 12, p. 181281, 2018, doi: 10.1098/rsos.181281.

[142] « Thermistor - an overview | ScienceDirect Topics ». https://www.sciencedirect.com/topics/earth-and-planetary-sciences/thermistor (consulté le nov. 30, 2020).

[143] G. J. Lavenuta, « Negative temperature coefficient thermistors ».

[144] B. Danielsson, « SENSORS | Calorimetric/Enthalpimetric », in *Encyclopedia of Analytical Science (Second Edition)*, P. Worsfold, A. Townshend, et C. Poole, Éd. Oxford: Elsevier, 2005, p. 237-245.

[145] D. A. Christensen, « Thermal dosimetry and temperature measurements », *Cancer Res.*, vol. 39, nº 6 Part 2, p. 2325–2327, 1979.

[146] M. Zhadobov, S. I. Alekseev, R. Sauleau, Y. L. Page, Y. L. Dréan, et E. E. Fesenko, « Microscale temperature and SAR measurements in cell monolayer models exposed to

millimeter waves », *Bioelectromagnetics*, vol. 38, nº 1, p. 11-21, 2017, doi: https://doi.org/10.1002/bem.21999.

[147] R. Orlacchio, « Millimeter waves for biomedical electromagnetics : study of changes induced at the cellular level by pulsed electromagnetically-induced heating », These de doctorat, Rennes 1, 2019.

[148] T. Togawa, « Body temperature measurement », *Clin. Phys. Physiol. Meas.*, vol. 6, nº 2, p. 83, 1985.

[149] É. Pinet, S. Ellyson, F. Borne, et F. Technologies, « Temperature fiber-optic point sensors : commercial technologies and industrial applications », 2010.

[150] P. Kolodner et J. A. Tyson, « Microscopic fluorescent imaging of surface temperature profiles with 0.01 °C resolution », *Appl. Phys. Lett.*, vol. 40, nº 9, p. 782-784, mai 1982, doi: 10.1063/1.93258.

[151] O. Zohar *et al.*, « Thermal Imaging of Receptor-Activated Heat Production in Single Cells », *Biophys. J.*, vol. 74, nº 1, p. 82-89, janv. 1998, doi: 10.1016/S0006-3495(98)77769-0.

[152] D. Moreau, C. Lefort, R. Burke, P. Leveque, et R. P. O'Connor, « Rhodamine B as an optical thermometer in cells focally exposed to infrared laser light or nanosecond pulsed electric fields », *Biomed. Opt. Express*, vol. 6, nº 10, Art. nº 10, sept. 2015, doi: 10.1364/BOE.6.004105.

[153] K. H. Drexhage, « Structure and properties of laser dyes », in *Dye lasers*, Springer, 1973, p. 144–193.

[154] W.-T. Liu, J.-H. Wu, E. S.-Y. Li, et E. S. Selamat, « Emission Characteristics of Fluorescent Labels with Respect to Temperature Changes and Subsequent Effects on DNA Microchip Studies », *Appl. Environ. Microbiol.*, vol. 71, nº 10, p. 6453-6457, oct. 2005, doi: 10.1128/AEM.71.10.6453-6457.2005.

[155] « Quantum Yield - an overview | ScienceDirect Topics ». https://www.sciencedirect.com/topics/biochemistry-genetics-and-molecular-biology/quantum-yield (consulté le oct. 08, 2020).

[156] R. F. Kubin et A. N. Fletcher, « Fluorescence quantum yields of some rhodamine dyes », *J. Lumin.*, vol. 27, nº 4, p. 455-462, déc. 1982, doi: 10.1016/0022-2313(82)90045-X.

[157] R. E. Schwerzel et N. E. Klosterman, « Temperature dependence of the fluorescence quantum yields of rhodamine derivatives », *US Dept Commer. Nat Bur. Stand Spectosc Publ*, nº 526, p. 3–4, 1978.

[158] G. Weber et F. W. J. Teale, « Determination of the absolute quantum yield of fluorescent solutions », *Trans. Faraday Soc.*, vol. 53, p. 646, 1957, doi: 10.1039/tf9575300646.

[159] C. A. Parker et W. T. Rees, « Correction of fluorescence spectra and measurement of fluorescence quantum efficiency », *The Analyst*, vol. 85, nº 1013, p. 587, 1960, doi: 10.1039/an9608500587.

[160] J. Ferguson et A. W. H. Mau, « Spontaneous and stimulated emission from dyes. Spectroscopy of the neutral molecules of acridine orange, proflavine, and rhodamine B », *Aust. J. Chem.*, vol. 26, nº 8, p. 1617–1624, 1973.

[161] J. J. Shah, M. Gaitan, et J. Geist, « Generalized temperature measurement equations for rhodamine B dye solution and its application to microfluidics », *Anal. Chem.*, vol. 81, nº 19, p. 8260–8263, 2009.

[162] J. Sakakibara, K. Hishida, et M. Maeda, « Measurements of thermally stratified pipe flow using image-processing techniques », *Exp. Fluids*, vol. 16, nº 2, p. 82-96, déc. 1993, doi: 10.1007/BF00944910.

[163] M. Soueid *et al.*, « Electromagnetic Analysis of an Aperture Modified TEM Cell Including an Ito Layer for Real-Time Observation of Biological Cells Exposed to Microwaves », *Prog. Electromagn. Res.*, vol. 149, p. 193-204, 2014, doi: 10.2528/PIER14053108.

[164] S. Kohler, R. P. O'Connor, T. D. T. Vu, P. Leveque, et D. Arnaud-Cormos, « Experimental Microdosimetry Techniques for Biological Cells Exposed to Nanosecond Pulsed Electric Fields Using Microfluorimetry », *IEEE Trans. Microw. Theory Tech.*, vol. 61, nº 5, Art. nº 5, mai 2013, doi: 10.1109/TMTT.2013.2252917.

[165] Y. Y. Chen et A. W. Wood, « Application of a temperature-dependent fluorescent dye (Rhodamine B) to the measurement of radiofrequency radiation-induced temperature changes in biological samples », *Bioelectromagnetics*, vol. 30, nº 7, Art. nº 7, oct. 2009, doi: 10.1002/bem.20514.

[166] D. Ross, M. Gaitan, et L. E. Locascio, « Temperature measurement in microfluidic systems using a temperature-dependent fluorescent dye », *Anal. Chem.*, vol. 73, nº 17, Art. nº 17, sept. 2001.

[167] A. Nefzi, L. Carr, C. Dalmay, A. Pothier, P. Leveque, et D. Arnaud-Cormos, « Microdosimetry Using Rhodamine B Within Macro- and Microsystems for Radiofrequency Signals Exposures of Biological Samples », *IEEE Trans. Microw. Theory Tech.*, vol. 68, nº 3, p. 1142-1150, mars 2020, doi: 10.1109/TMTT.2019.2950191.

[168] S. Ebert, K. Travis, B. Lincoln, et J. Guck, « Fluorescence ratio thermometry in a microfluidic dual-beam laser trap », *Opt. Express*, vol. 15, nº 23, p. 15493–15499, 2007.

[169] R. Fu, B. Xu, et D. Li, « Study of the temperature field in microchannels of a PDMS chip with embedded local heater using temperature-dependent fluorescent dye », *Int. J. Therm. Sci.*, vol. 45, nº 9, p. 841–847, 2006.

[170] R. Samy, T. Glawdel, et C. L. Ren, « Method for microfluidic whole-chip temperature measurement using thin-film poly (dimethylsiloxane)/Rhodamine B », *Anal. Chem.*, vol. 80, nº 2, p. 369–375, 2008.

[171] C. A. Thomas, P. A. Springer, G. E. Loeb, Y. Berwald-Netter, et L. M. Okun, « A miniature microelectrode array to monitor the bioelectric activity of cultured cells », *Exp. Cell Res.*, vol. 74, nº 1, Art. nº 1, sept. 1972, doi: 10.1016/0014-4827(72)90481-8.

[172] M. O. Heuschkel, M. Fejtl, M. Raggenbass, D. Bertrand, et P. Renaud, « A three-dimensional multi-electrode array for multi-site stimulation and recording in acute brain slices », *J. Neurosci. Methods*, vol. 114, nº 2, Art. nº 2, mars 2002, doi: 10.1016/S0165-0270(01)00514-3.

[173] M. Baca, H. Bartsch, T. Porzig, A. Williamson, et A. Schober, « 3D Multi Electrode Arrays », p. 3.

[174] M. E. J. Obien, K. Deligkaris, T. Bullmann, D. J. Bakkum, et U. Frey, « Revealing neuronal function through microelectrode array recordings », *Front. Neurosci.*, vol. 8, p. 423, 2015.

[175] J. N. Aziz, R. Genov, B. L. Bardakjian, M. Derchansky, et P. L. Carlen, « Brain–silicon interface for high-resolution in vitro neural recording », *IEEE Trans. Biomed. Circuits Syst.*, vol. 1, nº 1, p. 56–62, 2007.

[176] L. Guo, G. S. Guvanasen, X. Liu, C. Tuthill, T. R. Nichols, et S. P. DeWeerth, « A PDMS-based integrated stretchable microelectrode array (isMEA) for neural and muscular surface interfacing », *IEEE Trans. Biomed. Circuits Syst.*, vol. 7, nº 1, p. 1–10, 2012.

[177] J. Guo, W. Ng, J. Yuan, S. Li, et M. Chan, « A 200-channel area-power-efficient chemical and electrical dual-mode acquisition IC for the study of neurodegenerative diseases », *IEEE Trans. Biomed. Circuits Syst.*, vol. 10, nº 3, p. 567–578, 2015.

[178] M. Chiappalone, V. Pasquale, et M. Frega, *In Vitro Neuronal Networks: From Culturing Methods to Neuro-Technological Applications*, vol. 22. Springer, 2019.

# Liste des publications et communications

## I. Revues internationales à comité de lecture

1. **Nefzi A.**, Carr L., Dalmay C., Pothier A., Leveque P**.**, Arnaud-Cormos D. "Microdosimetry Using Rhodamine B Within Macro and Micro Systems for Radiofrequency Signals Exposures of Biological Samples". M*icrowave Theory and Techniques, IEEE Transactions on, 68(3), pp. 1142-1150. Published: March 2020***.** DOI: 10.1109/TMTT.2019.2950191

2. **Nefzi A.**, Orlacchio R., Carr L., Lemercier C., El Khoueiry C., Lewis N., Leveque L., Arnaud-Cormos D., "Dosimetry of Microelectrodes Array Chips for Electrophysiological Studies under Simultaneous Radiofrequency Exposures". *Biomedical Circuits and Systems, IEEE Transactions, en soumission*

## II. Communications internationales avec actes de colloque à comité de lecture

1. **Nefzi A.**, Percherancier Y. Lagroye I., Leveque P., Arnaud-Cormos D.,"Delivery setup compatible for in vitro impedance measurements and exposures to electromagnetic fields: nanosecond pulse electric fields and radiofrequency signals" in 2nd World Congress on Eletroporation, Norfolk, USA, 24-28 Sept, 2017.

2. **Nefzi A.**, Leveque P., Arnaud-Cormos D. "Frequency characterization of wire electrodes devices for biomedical applications " in cinquième colloque francophone Pluridisciplinaire sur les Matériaux, l'Environnement et l'Électronique, PLUMEE 2017, Bacau, Roumanie. 19-21 Octobre 2017. Oral session

3. **Nefzi A.**, Carr L., Leveque P., Arnaud-Cormos D. "Experimental Dosimetry using the Fluorescence of Rhodamine B under Radiofrequency exposure. " in sixième colloque francophone Pluridisciplinaire sur les Matériaux, l'Environnement et l'Électronique, PLUMEE 2019, Limoges, France. 10-12 Avril. Oral session

4. **Nefzi A.**, E. Lemercier C., El Khoueiry C., Lewis N., Lagroye I., Boucsein C., Leveque P., Arnaud-Cormos D., "Microdosimetry of Multi Electrodes Array in an RF Exposure System for In Vitro Real-Time Recordings." in The IEEE MTT-S International Microwave Biomedical Conference, IMBioC 2019, Nanjing, China, 6 – 8 May. Oral Session.

5. **Nefzi A.**, Carr L., Arnaud-Cormos D., Leveque P., "Planar Interdigitated Array Electrodes for RF Exposure of Biological samples. " in European Microwave Conference in Central Europe, EuMCE 2019, Prague, Czech Republic, 13 – 15 May. Oral Session.

6. **Nefzi A.**, Carr L., Dalmay C., Pothier A., Leveque P., Arnaud-Cormos D.,"Rhodamine B Temperaure Dosimetry of Biological Samples Interacting with Electromagnatic Fields in Macrosystems," in IEEE MTT-S International Microwave Symposium, IMS 2019; Boston, MA; USA, 2-7 June. Poster session.

7. **Nefzi A.**, Lemercier C.E., Lewis N., Lagroye I., Leveque P., Arnaud-Cormos D., "Dosimetric study of electrophysiological recording devices based on micro-electrodes under Radio-Frequency exposures", in BioEM2019, Joint Meeting of the BioElectroMagnetics Society and the European BioElectromagnetics Association, Montpellier, France, 23-28 June 2019. Poster session.

8. **Nefzi A.**, Carr L., Leveque P., Arnaud-Cormos D. " Thermal measurements using a temperature-dependent dye under electromagnetic fields exposure", WC2019, 3rd World Congress on Electroporation and Pulsed Electric Fields in Biology, Medicine and Food & Environmental Technologies, Toulouse, France 3-6 Sept. 2019

9. Orlacchio R., **Nefzi A.**, Percherancier Y., Leveque P., Arnaud-Cormos D., "In vivo functional ultrasound (fUS) imaging of mice brain under radiofrequency exposure: preliminary dosimetric results", in BioEM2020, Joint Meeting of the BioElectroMagnetics Society and the European BioElectromagnetics Association, Oxford, UK, June 2020. Abstract book.

10. **Nefzi A.**, Orlacchio R., Carr L., Lewis N., Percherancier Y., Leveque P., Arnaud-Cormos D., "Microscale Temperature Measurements Within Specific Exposure Systems for Real-Time Cellular Characterization" in IEEE IMBioC 2020, Toulouse, France, 14-17 December 2020, Oral session.

## Analyse et dosimétrie du couplage des ondes électromagnétiques avec les tissus biologiques : application à la conception d'applicateur pour le biomédical et l'étude des effets sanitaires

**Résumé :** L'évolution et l'utilisation croissante des systèmes de communications mobiles sont associées à des études en laboratoire pour s'assurer de l'innocuité d'une exposition aux ondes électromagnétiques radiofréquences. Dans ce contexte, ce mémoire se concentre sur la caractérisation de systèmes d'exposition permettant des études en laboratoire sur des modèles cellulaires *in vitro*. Une double approche, numérique et expérimentale, est mise en œuvre pour réaliser la dosimétrie de ces dispositifs, afin de déterminer et maitriser les niveaux d'exposition. Une des problématiques liées à cette dosimétrie est due aux dimensions micrométriques mises en jeu. Aussi, une technique de microscopie basée sur un marqueur fluorescent dépendant de la température, nommé Rhodamine B, a été mise en place et évaluée. Il ressort de cette évaluation une recommandation sur la concentration du marqueur de l'ordre de 50 µM. Après calibration, il est alors possible d'estimer le débit d'absorption spécifique (DAS) à partir de la variation de température, et ce même pour de faibles niveaux de DAS (< W/kg) avec une résolution spatiale inférieure à la dizaine de micron. On parle alors de microdosimétrie. Les deux principaux systèmes d'exposition étudiés, basés sur des réseaux de microélectrodes (MEA), permettent l'enregistrement d'une activité électrophysiologie de neurones. L'exposition aux ondes électromagnétiques est réalisée simultanément en insérant ces MEA dans des cellules TEM. De la dosimétrie effectuée à 1.8 GHz, il ressort une plus forte sensibilité du premier MEA à son environnement. On a montré que les modifications apportées au second MEA, taille de l'ouverture et plan de masse, ont permis de limiter de façon significative l'influence de l'environnement. La microdosimétrie a mis en évidence une bonne homogénéité du DAS entre les électrodes avec une valeur estimée à 7±1 W/kg pour 1 W incident. Enfin, un dispositif d'exposition microfluidique basé sur un guide d'ondes coplanaire a été caractérisé en conditions statiques.

**Mots-clés :** Bioelectromagnetisme, dosimétrie, Rhodamine B, fluorescence, débit d'absorption spécifique (DAS), Multielectrode array (MEA).

## Analysis and dosimetry of the coupling of electromagnetic waves with biological tissues: application to applicator design for biomedical and study of health effects

**Abstract :** The evolution and increasing use of mobile communications systems was associated with laboratory investigations to study radiofrequency electromagnetic waves exposure safety. In this context, this thesis focuses on the characterization of exposure systems allowing laboratory in vitro studies on cell models. A dual numerical and experimental approach is implemented to perform the devices dosimetry allowing to determine and control the exposure levels. One of the limitations associated with this dosimetry is due to the micrometric dimensions involved. Therefore, a microscopy technique based on a temperature-dependent fluorescent dye named Rhodamine B was set up and evaluated. This assessment recommends an optimal concentration of the dye at around 50 µM. After calibration, it is possible to estimate the specific absorption rate (SAR) from the temperature variation, even for low levels of SAR (< W / kg) with a spatial resolution of less than ten micrometers i.e. microdosimetry. The two main exposure systems studied, based on microelectrode arrays (MEA), allow the recording of neurons electrophysiological activity. Exposure to electromagnetic waves is achieved simultaneously by inserting these MEAs into TEM cells exposure systems. Dosimetry carried out at 1.8 GHz shows a higher sensitivity of one MEA to its environment. It was shown that the modifications made to the second MEA such as its aperture size and ground planes, have reduced the proximity environment influence. The microdosimetry demonstrated good homogeneity of the SAR between the electrodes with an estimated value of 7 ± 1 W / kg for 1 W incident power. Finally, a microfluidic exposure device based on a coplanar waveguide was characterized under static conditions.

**Keywords :** Bioelectromagnetic, Electromagnetic field, dosimetry, Rhodamine B, fluorescence, Specific absorption rate (SAR), Multielectrode array (MEA).